

# Optimized Feedback Control of Vortex Shedding on an Inclined Flat Plate

Thesis by

Won Tae Joe

In Partial Fulfillment of the Requirements

for the Degree of

Doctor of Philosophy



California Institute of Technology

Pasadena, California

2010

(Submitted June 7, 2010)

© 2010

Won Tae Joe

All Rights Reserved

To my parents, JangHo and JaKyung Joe, and  
in memory of my grandparents, JoongChae Joe(1927–2009) and KeumRae Ahn (1931–2009)

# Acknowledgments

My advisor, Professor Tim Colonius, is gratefully acknowledged for his support and teachings throughout my graduate studies. His passion for research and science has been a great inspiration. I thank him for all his patience in guiding me through the road to become a better scientist and also for the countless revisions to my papers. It has been a true joy and an unparalleled learning experience. I would also like to acknowledge Doctor Douglas MacMynowski for his guidance and critical comments on controls and dynamics in order to make the design and implementation of the feedback system possible. Professors Fazle Hussain, Morteza Gharib, and Beverly McKeon have offered enlightening comments and graciously agreed to serve on my committee.

I was also fortunate to have been involved in a multi-disciplinary research initiative (MURI), receiving insightful comments by Professors Clarence Rowley (Princeton Univ), David Williams (Illinois Inst of Tech), Gilead Tadmor (Northeastern Univ), and Doctor William Dickson. Funding for this research was provided by the U.S. Air Force Office of Scientific Research and some of the computations were made possible by the U.S. Department of Defense High Performance Computing Modernization Program. I must also thank Professor Colm Caulfield (University of California, San Diego, now at University of Cambridge) for his guidance during my undergraduate studies. He has been a great motivation for me both, in my first scientific research project, and in my continued pursuit of graduate-level studies.

I would also like to thank and acknowledge all my colleagues and peers, here at Caltech. My laboratory members, Kunihiko Taira, Jennifer Frank, Jeff Krimmel, Kristjan Gudmundsson and Guillaume Bres, have been integral in my success; providing me with insightful comments and helping establish a collegial working environment. My roommates, Jeff Hanna and Andrew Tchieu,

have helped immensely in creating a life outside of the lab, which has given me mental and emotional stability throughout my Caltech tenure.

Additionally, I would like to thank my previous roommates from University of California, San Diego, Andy Yoon and Larry Chae, for helping shape my character during our college days and for providing continual emotional and mental support.

Last, but by no means least, I would like to wholeheartedly thank my wonderful family. My parents, Jangho and Jakyung Joe, have provided me with unconditional love and support throughout all my studies, as well as providing me with guidance through my life. My brother, Daniel Wonjung Joe, has supported me and provided me with more motivation than one sibling could ask for from another sibling. And finally, I would like to thank my grandparents, Jungchae Joe and Keumrae Ahn, for their unwavering faith and pride in my accomplishments, both past and future.

# Abstract

This thesis examines flow control and the potentially favorable effects of feedback, associated with unsteady actuation in separated flows over airfoils. The objective of the flow control is to enhance lift at post-stall angles of attack by changing the dynamics of the wake vortices. We present results from a numerical study of unsteady actuation on a two-dimensional flat plate at post-stall angles of attack at Reynolds number (Re) of 300 and 3000. At  $Re = 300$ , the control waveform is optimized and a feedback strategy is developed to optimize the phase of the control relative to the lift with either a sinusoidal or the optimized waveform, resulting in a high-lift limit cycle of vortex shedding. Also at  $Re = 3000$ , we show that certain frequencies and actuator waveforms lead to stable (high-lift) limit cycles, in which the flow is phase locked to the actuation

First, a two-dimensional flat plate model at a high angle of attack at a Re of 300 is considered. With the sinusoidal forcing, we find that certain phase shifts between the forcing and lift signals result in very high period-averaged lifts. We design the feedback to slightly adjust the frequency and/or phase of actuation to lock it to a particular phase of the lift, thus achieving a phase-locked flow with the maximal period-averaged lift over every cycle of actuation.

With the sinusoidal forcing and feedback, we show that it is possible to optimize the phase of the control relative to the lift in order to achieve the highest possible period-averaged lift in a consistent fashion. However, continuous sinusoidal forcing could be adding circulation when it is unnecessary, or undesirable. Thus we employ an adjoint-based optimization in order to find the waveform (time history of  $U_j$ ) that maximizes the lift for a given actuation amplitude. The adjoint of the linearized perturbed equations is solved backwards in time to obtain the gradient of the lift to changes in actuation (the jet velocity), and this information is used to iteratively improve the controls.

Optimal control provides a periodic control waveform, resulting in high lift shedding cycle with minimal control input. However, if applied in open loop, the flow fails to phase lock onto the optimal waveform, degrading the lift performance. Thus, the optimized waveform is also implemented in a closed-loop controller where the control signal is shifted or deformed periodically to adjust to the (instantaneous) frequency of the lift fluctuations. The feedback utilizes a narrowband filter and an Extended Kalman Filter to robustly estimate the phase of vortex shedding and achieve phase-locked, high lift flow states. Feedback control of the optimized waveform is able to reproduce the high-lift limit cycle from the optimization, but starting from an arbitrary phase of the baseline limit cycle.

Finally, we apply the tools developed and knowledge gained at  $Re = 300$  to a  $Re$  of 3000 on a thin airfoil with a thickness-to-chord ratio of 4%, which were chosen to match the experimental studies of Greenblatt *et al.* (2008). We consider more detailed time-dependent aspects of the lift and corresponding flow fields, particularly the flow structures at the minimum and maximum lift, and the phase of pulses relative to the lift, in order to more precisely compare different actuated flow fields and distinguish the differences responsible for higher or lower instantaneous lift, along with identifying different vortex evolutions. We consider two representative angles of attack,  $\alpha = 10^\circ$  and  $20^\circ$ , and investigate the lift enhancement and which combinations of forcing frequency and duty cycle lead to phase-locked flow. Finally, we show that for certain frequencies and actuator waveforms, there occur stable limit cycles in which the flow is phase locked to the actuation.

# Contents

<b>Acknowledgments</b>	<b>iv</b>
<b>Abstract</b>	<b>vi</b>
<b>Contents</b>	<b>viii</b>
<b>List of Figures</b>	<b>xi</b>
<b>Nomenclature</b>	<b>xvi</b>
<b>1 Introduction</b>	<b>1</b>
1.1 Background of Flow Control . . . . .	3
1.2 Open-Loop Control . . . . .	5
1.3 Feedback Control . . . . .	6
1.4 Overview of Current Work . . . . .	7
<b>2 Numerical Methods</b>	<b>10</b>
2.1 Fast Immersed Boundary Method . . . . .	10
<b>3 Sinusoidal Forcing at <math>Re = 300</math></b>	<b>16</b>
3.1 Numerical Method . . . . .	16
3.2 Results . . . . .	18
3.2.1 Uncontrolled Flow . . . . .	18
3.2.2 Open-loop control . . . . .	19

3.2.2.1	Leading-edge actuation . . . . .	19
3.2.2.2	Trailing-edge actuation . . . . .	24
3.3	Closed-loop control . . . . .	26
<b>4</b>	<b>Optimized waveform at <math>Re = 300</math></b>	<b>37</b>
4.1	Numerical Method . . . . .	38
4.2	Adjoint-based Optimization . . . . .	39
4.2.1	Adjoint-based Optimization: Cost Functional and Sensitivity . . . . .	39
4.2.2	Adjoint-based Optimization: Formulation . . . . .	40
4.2.3	Adjoint-based Optimization: Numerical Implementation . . . . .	42
4.2.4	Adjoint-based Optimization: Results . . . . .	44
4.3	Feedback . . . . .	45
4.4	Results of Optimized Feedback Control . . . . .	47
4.5	Sinusoidal Pulse . . . . .	52
<b>5</b>	<b>Control at <math>Re = 3000</math></b>	<b>56</b>
5.1	Numerical Method . . . . .	57
5.2	Uncontrolled flow . . . . .	61
5.3	Actuation at $\alpha = 10^\circ$ . . . . .	62
5.4	Actuation at $\alpha = 20^\circ$ . . . . .	69
<b>6</b>	<b>Conclusions</b>	<b>83</b>
6.1	Control at $Re = 300$ . . . . .	84
6.1.1	Sinusoidal Forcing . . . . .	84
6.1.2	Optimization of the Control Waveform . . . . .	85
6.1.3	Feedback Control with the Optimized Waveform . . . . .	86
6.2	Control at $Re = 3000$ . . . . .	87
6.3	Recommendations for Future Work . . . . .	89

<b>Appendix A</b>	<b>Appendix A</b>	<b>91</b>
A.1	Derivation of Linearized and Adjoint Equations . . . . .	91
<b>Appendix B</b>	<b>Appendix B</b>	<b>94</b>
B.1	Extended Kalman Filter . . . . .	94
<b>Bibliography</b>		<b>97</b>

# List of Figures

2.1	Multi-domain method to solve the Poisson equation. Figure reproduced with permission from Colonius & Taira (2008). . . . .	15
3.1	Schematic of actuation at leading and trailing edge. . . . .	18
3.2	Vorticity and streamlines of translating flat plate at different angle of attack, $\alpha$ at $Re = 300$ . . . . .	20
3.3	Leading-edge actuation: maximum and minimum lift ( $\square$ ) and its average over time ( $\circ$ ) for downstream (left) and upstream (right) actuation. Average of the baseline case is plotted in dashed grey and shaded region is bounded by its maximum and minimum. Actuation is applied at the natural shedding frequency, $\omega_f = \omega_n$ . For cases where the flow is not phase locked to the forcing signal, variation in period-averaged lift over each actuation period is plotted with error bar to indicate the range of values over a subharmonic limit cycle. . . . .	22
3.4	Lift as a function of time (a) and jet velocity (b) with upstream actuation at the leading edge (LE, upstream) at the natural shedding frequency ( $\omega_f = \omega_n$ ) for $\alpha = 50^\circ$ . . . . .	23
3.5	Trailing-edge actuation: see Figure 3.3 for a description. . . . .	27
3.6	Lift with upstream actuation at the trailing-edge at its natural shedding frequency ( $\omega_f = \omega_n$ ), for $\alpha = 50^\circ$ . . . . .	28
3.7	Vorticity contour at the time of maximum lift for baseline (thin) and upstream actuation (thick) at the trailing edge at the natural shedding frequency ( $\omega_f = \omega_n$ ). Dashed and solid lines represent counterclockwise and clockwise vorticity. . . . .	28

3.8	Vorticity contour at the time of maximum lift for baseline (black) and upstream actuation (red) at the trailing edge at the natural shedding frequency ( $\omega_f = \omega_n$ ). . . . .	29
3.9	Trailing-edge actuation: maximum and minimum lift ( $\square$ ), average lift ( $\circ$ ), and period-averaged lift (error bar) over a range of open-loop forcing frequency, $\omega_f$ . Maximum and minimum lift of baseline (- - -) case is shown as a reference. . . . .	30
3.10	Trailing-edge actuation: phase shift of the forcing signal, $U_j$ , relative to the lift signal, $C_L$ , for phase-locked flows, over a range of open-loop forcing frequency, $\omega_f$ ( $\alpha = 30^\circ$ ). . . . .	31
3.11	Feedback control configuration. . . . .	31
3.12	Maximum and minimum lift ( $\square$ ) and its average over time ( $\circ$ ) (top) and frequency (bottom) of phase-locked limit cycles at different phase-shift, $\phi_o$ , for (a) $\alpha = 40^\circ$ and (b) $50^\circ$ . . . . .	35
3.13	Comparison between open-loop control case (-), that phase locked the flow at the highest average $C_L$ (denoted as $OL_1$ in Figure 3.9(c)), and the corresponding feedback control case (-) (denoted as $FB_1$ in Figure 3.12). Forcing frequency of this open-loop control is denoted as $\omega_{f,OL_1}$ , and the average output frequency of $C_L$ of the feedback control is denoted as $\omega_{o,FB_1}$ . . . . .	36
3.14	Continuation of feedback control case in figure 3.13 with open-loop control of $\omega_f$ . . . . .	36
4.1	Schematic of upstream actuation at the trailing-edge. . . . .	39
4.2	Schematic of receding-horizon predictive control. First the optimization of controls are performed on horizon $[t_0, t_1]$ . Each iteration of optimization gives the update on control. Once the convergence of the control on the optimization is achieved, the flow is ‘advanced’ some portion $T_a$ of the period $T$ , and controls near the end of the optimization horizon are discarded and the optimization is begun anew on horizon $[t_0 + T_a, t_1 + T_a]$ . . . . .	44
4.3	Schematic of feedback. . . . .	47

4.4	Comparison between open-loop control case (grey) and the feedback control case (black) with optimized waveform ( $N_k = 10$ ) at $\alpha = 40^\circ$ . . . . .	48
4.5	Comparison of optimized control (—) with closed-loop sinusoidal forcing(—) at $\alpha = 40^\circ$ . Maximum and minimum lift of baseline (- - -) case is shown as a reference. . . . .	50
4.6	Vorticity contour at the (a) minimum and (b) maximum lift for baseline (black) and sinusoidal actuation (blue). Dashed and solid lines represent counterclockwise and clockwise vorticity. . . . .	50
4.7	Vorticity contour at the (a) minimum and (b) maximum lift for sinusoidal actuation (blue) and optimized actuation (red). Dashed and solid lines represent counterclockwise and clockwise vorticity. . . . .	51
4.8	Average lift of optimized control ( $\square$ ) and closed-loop sinusoidal forcing ( $\circ$ ) at different values of $C_\mu$ at $\alpha = 40^\circ$ . For the optimized control, different values of the control weight, $C_w$ is used in (4.4), resulting in corresponding values of $C_\mu$ as shown. . . . .	51
4.9	Comparison between feedback control cases with optimized waveform at $\alpha = 40^\circ$ : $N_k = 10$ (dashed) and $N_k = 4$ (solid). . . . .	52
4.10	Maximum and minimum lift ( $\square$ ) and average lift ( $\circ$ ) of phase-locked limit cycles at different phase shift with optimized waveform ( $N_k = 10$ ) at $\alpha = 40^\circ$ . Maximum and minimum lift of baseline (- - -) case is shown as a reference. . . . .	52
4.11	Sinusoidal pulses of different widths with either a constant maximum (blue) or average (green) $U_j$ . Duty cycle is defined here as a percentage of the width of a sinusoidal waveform to the period of actuation. Thus, a duty cycle of 100% gives a continuous sinusoidal waveform (black). The feedback was used to phase lock the flow near zero phase shift. This phase shift results in the highest average lift for all cases considered. For the optimized control (red), different values of the control weight were used in each optimization to result in different values of $C_\mu$ as shown. . . . .	54

4.12	Sinusoidal pulse with constant maximum (blue) and average (green) $U_j$ . Circles and x-marks indicate higher and lower average $C_L$ , respectively, than the maximum lift achieved by baseline shedding cycle. . . . .	55
5.1	Schematic of flat plate of thickness-to-chord ratio of 4% and actuation at the leading edge. . . . .	60
5.2	Sinusoidal pulse waveform, $U_j(t)$ and phase, $\theta(t)$ with duty cycle, $DC = 5\%$ (red), 50% (blue), 100% (black). $\theta(t) = 2\pi$ is a period of every pulse. Duty cycle is defined here as a percentage of the width of a sinusoidal waveform to the period of actuation. Thus, a duty cycle of 100% gives a continuous sinusoidal waveform (black). . . . .	60
5.3	Average lift coefficient of the baseline flow, comparing results here with experimental data by Greenblatt <i>et al.</i> (2008) at $Re = 3,000$ and by Alam <i>et al.</i> (2010) at $Re = 5,000$ and 10,000. . . . .	63
5.4	Lift and power spectrum of baseline flow at $\alpha = 10^\circ$ (black) and $\alpha = 20^\circ$ (red). . . . .	64
5.5	(a) Smoke-visualization by Greenblatt <i>et al.</i> (2008), and (b) streaklines and (c) vorticity field from present simulation of baseline flow ( $\alpha = 10^\circ$ ). . . . .	65
5.6	(a) Smoke-visualization by Greenblatt <i>et al.</i> (2008), and (b) streaklines and (c) vorticity field from present simulation of baseline flow ( $\alpha = 20^\circ$ ). . . . .	66
5.7	(a) Smoke-visualization by Greenblatt <i>et al.</i> (2008) and (b) streaklines of fluid particles of actuated flow with $DC = 5\%$ , $F^+ = 0.42$ ( $\alpha = 10^\circ$ ). . . . .	67
5.8	Streaklines (top) and vorticity field (bottom) at (a) minimum and (b) maximum lift and (c) maximum pulse with $DC = 5\%$ and $F^+ = 0.42$ ( $\alpha = 10^\circ$ ). . . . .	68
5.9	Time history of lift and $U_j$ of actuated flow at $F^+ = 0.42$ with $DC = 5\%$ ( $\alpha = 10^\circ$ ). Dashed lines indicate the moment of minimum (min) and maximum (max) lift and time corresponding to the maximum of the input waveform to the actuator (pulse). . . . .	69

5.10	Sinusoidal pulse with (a) $DC = 5\%$ and (b) $100\%$ ( $\alpha = 10^\circ$ ). Squares represent the maximum and minimum lift, and circles represent overall average lift. The period-averaged lift once per cycle of actuation is plotted in gray(*), and the flow is observed to be periodic (phase-locked) when these collapse to a single point (meaning they are the same each cycle). . . . .	70
5.11	Time history of lift and $U_j$ of actuated flow at $F^+ = 1.9$ with $DC = 100\%$ ( $\alpha = 10^\circ$ ). . . . .	71
5.12	Streaklines (top) and vorticity field (bottom) at (a) minimum and (b) maximum lift with $DC = 100\%$ and $F^+ = 1.90$ ( $\alpha = 10^\circ$ ). . . . .	71
5.13	Average lift increase over a range of forcing frequency at $\alpha = 20^\circ$ with 5% duty cycle (DC) compared to the results by Greenblatt <i>et al.</i> (2008). . . . .	72
5.14	(a)Smoke-visualization by Greenblatt <i>et al.</i> (2008) and (b) streaklines of fluid particles of actuated flow with $DC = 5\%$ , $F = 0.40$ ( $\alpha = 20^\circ$ ). . . . .	73
5.15	Streaklines (top) and vorticity field (bottom) at (a) minimum and (b) maximum lift with $DC = 5\%$ and $F^+ = 0.40$ ( $\alpha = 20^\circ$ ). . . . .	74
5.16	Sinusoidal pulse with $DC = 5\%$ , $10\%$ , $50\%$ , and $100\%$ ( $\alpha = 20^\circ$ ). Squares represent the maximum and minimum lift, and circles represent overall average lift. The period-averaged lift once per cycle of actuation is plotted in gray(*), and the flow is observed to be periodic (phase-locked) when these collapse to a single point (meaning they are the same each cycle). . . . .	76
5.17	Time history of lift of actuated flow phase-locked at $F^+ = 0.5$ ( $\alpha = 20^\circ$ ). . . . .	77
5.18	Streaklines of actuated flow phase-locked at $F^+ = 0.5$ ( $\alpha = 20^\circ$ ). . . . .	78
5.19	Vorticity field of actuated flow phase-locked at $F^+ = 0.5$ ( $\alpha = 20^\circ$ ). . . . .	79
5.20	Time history of lift of actuated flow phase-locked at $F^+ = 0.6$ ( $\alpha = 20^\circ$ ). . . . .	80
5.21	Streaklines of actuated flow phase-locked at $F^+ = 0.6$ ( $\alpha = 20^\circ$ ). . . . .	81
5.22	Vorticity field of actuated flow phase-locked at $F^+ = 0.6$ ( $\alpha = 20^\circ$ ). . . . .	82

# Nomenclature

## Greek letters

$\alpha$	angle of attack
$\langle C_\mu \rangle$	unsteady momentum coefficient
$\rho$	density
$c$	chord length
$C_\mu$	momentum coefficient
$C_D$	drag coefficient
$C_L$	lift coefficient

## Acronyms

LEV	leading-edge vortex
MAVs	micro-air vehicles
TEV	trailing-edge vortex

# Chapter 1

## Introduction

Micro-air vehicles (MAVs) operate at Reynolds number as low as  $Re \sim O(10^4)$  and their operating  $Re$  will continue to decrease (Pines & Bohorquez, 2006). Due to operational and weight requirements, these aircraft have unique designs with low-aspect-ratio wings, when compared to conventional aircraft. Moreover, these vehicles fly at low speed and often high angles of attack and experience large perturbations such as wind gusts. Torres & Mueller (2004) have addressed the need for data on the aerodynamics of low-aspect-ratio wings operating at low  $Re$ . Taira & Colonius (2009b) investigated three-dimensional flows around low-aspect-ratio wings in pure translation at  $Re$  of 300 and 500 and observed that the tip effects in three-dimensional flows can stabilize the flow (steady lift) and also exhibit nonlinear interaction with the shedding vortices (periodic or aperiodic lift behavior).

However, significant difficulty of achieving high lift-to-drag ratios at low  $Re$  have led many to the pursuit of biologically inspired approaches (Madangopal *et al.*, 2005; Raney & Slominski, 2004) that mimic, to a certain degree, the flight of small birds and insects. As MAVs become smaller in size, they share some characteristics with flying animals such as birds and insects. These animals have low-aspect-ratio wings operating at  $Re$  of order  $10^2$  to  $10^5$ , often at post-stall angles of attack. It has been observed in the flapping flight of bio-flyers that the leading-edge vortex (LEV) is formed and persists during most of their downstroke (Ellington *et al.*, 1996). This LEV provide additional spanwise circulation resulting in enhanced lift (Dickinson & Gotz, 1993). The LEV, in fact, accounts for most of the lift, and synchronization of its shedding appears to be necessary for rapid maneuvers

(Birch *et al.*, 2004; Birch & H., 2001; Wang, 2000).

In contrast to flapping flight, the objective of this thesis is to investigate the control of vortex shedding on conventional, purely translating airfoils at low Reynolds number ( $Re = O(10^2) - (10^3)$ ) using unsteady actuation in order to manipulate the LEV and vortex shedding. Previous work on flow control over an airfoil has used periodic excitation, such as unsteady mass injection and synthetic jets, to show that the oscillatory addition of momentum can eliminate or delay boundary layer separation and reattach a separated flow (Glezer & Amitay, 2002; Greenblatt & Wygnanski, 2000), or delay the shedding of the dynamic stall on a rapidly pitching airfoil (Magill *et al.*, 2003). Unsteady actuation was also shown to change the global dynamics of vortex shedding of post-stall flow, leading to higher unsteady lift than the natural shedding (Rullan *et al.*, 2006; Wu *et al.*, 1998).

However, most of the studies on post-stall flow control focus on open-loop actuation, but feedback can be used to change the dynamics of the unsteady shedding to provide even higher lift. For example, Wu *et al.* (1998) observed that the highest-lift vortex shedding cycle was not in perfect frequency lock-in with open-loop forcing; a subharmonic resonance was also excited. Such higher-lift vortex shedding may not be maintained with conventional open-loop forcing because the flow does not phase lock with the actuation signal. In such cases, feedback may provide continuous modification of the control input, according to the response of the flow system, to achieve higher lift. For example, Pastoor *et al.* (2008) used a phase-locking feedback strategy with zero-net-mass-flux actuation to synchronize the detachment of upper and lower shear layers for the turbulent flow around a D-shaped body, resulting in a 15% drag reduction. A physically motivated phase controller outperformed other approaches based on open-loop forcing and extremum-seeking feedback strategies.

The goal of the present study is to develop a closed-loop control of separated flow that uses vortex-induced lift to achieve lift enhancement aimed at micro air vehicles (MAVs). At  $Re$  usually experienced by MAVs, conventional low-Reynolds-number airfoils perform poorly and some of the best performing airfoils are cambered flat plates and thin airfoils with a thickness-to-chord ratio of approximately 5% (Mueller, 1999). Also, at high angles of attack,  $\alpha > 30^\circ$  once the separation point

moves upstream to the leading edge, surface curvature or airfoil shape does not play a significant role on the separated flow dynamics. Thus, in order to study the control of two basic constituents of unsteady post-stall flow (i.e. leading-edge and trailing-edge vortices) and develop a physically motivated feedback strategy, we consider a two-dimensional flow, at  $\text{Re} = O(100)$  to  $O(1000)$  over a flat plate. Even though introducing camber or using Eppler airfoil shape would improve uncontrolled performance, the flat plate ensures the separation at the leading edge in the post-stall regime and allows us to avoid additional complications due to the variation of the separation point or curvature effects of a different airfoil geometry. For the lower range of  $\text{Re}$ , 300 was selected to be sufficiently high to ensure forming and shedding of large coherent structures of opposite signs from the leading and trailing edges, a feature common to fully stalled wings at higher  $\text{Re}$ . Then the tools developed and the knowledge gained at  $\text{Re} = 300$  is applied to a  $\text{Re}$  of 3000, closer to MAVs operating condition, on a thin airfoil with a thickness-to-chord ratio of 4%.

## 1.1 Background of Flow Control

Flow control can be divided into passive and active control. Passive control utilizes a change in surface morphology that beneficially modifies the flow dynamics, but is fixed in place and offers no adaptivity once installed. Vortex generators mounted on airplane wings are one example of passive control, in which the slender vanes are thought to re-energize the boundary layer and delay separation resulting in better performance envelopes for ailerons and flaps. On the other hand, active control injects or withdraws mass or momentum from the flow via slots mounted flush to the surface and controlled by actuators.

Traditional boundary layer control is achieved through steady suction or blowing which is effective in increasing lift to drag ratios on airfoils. However steady suction/blowing control has had limited success due to the complexity of the installed system. Added weight and power requirements often negate the aerodynamic benefits (Greenblatt & Wygnanski, 2000).

While steady blowing is a tool investigated for more than eight decades, separation control by

periodic addition of momentum has been a subject of intense research only since the early 1990s. Its most striking feature is that a control goal, e.g., a specific lift increase, can typically be attained by orders of magnitude smaller momentum input compared to steady actuation (Greenblatt & Wygnanski, 2000).

Much of the recent research on flow control has been focused on synthetic jets (Glezer & Amitay (2002)). Synthetic jets are zero-net mass flux oscillatory control devices that are operated with lower power requirements than traditional boundary layer control. Such devices are often very small compared with the length of the body (less than 1% of chord) and are mounted flush with the surface. An oscillating surface, such as a membrane or piston adds momentum to the boundary layer, but only utilizes the fluid already contained in the system.

Frequently used parameters to characterize control are the time averaged momentum input and the excitation frequency. The momentum coefficient,  $C_\mu$  is defined as the momentum added to the flow divided by the momentum of the freestream.

$$C_\mu = \frac{\rho_s u_s^2 h_s}{\frac{1}{2} \rho_\infty U_\infty^2 c} \quad (1.1)$$

where the variables  $\rho_s$ ,  $u_s$ ,  $h_s$  are the density, velocity and width at the control slot and  $\rho_\infty$ ,  $U_\infty$ ,  $c$  are the density, velocity, and characteristic length scale of the freestream flow ( $c$ =chord length for flow control over an airfoil). In the case of periodic actuation, unsteady momentum coefficient  $\langle C_\mu \rangle$  is defined by

$$\langle C_\mu \rangle = \frac{\rho_s \langle u_s \rangle^2 h_s}{\frac{1}{2} \rho U_\infty^2 c} \quad (1.2)$$

and the frequency of oscillation,  $f$  is characterized by the reduced frequency

$$F^+ = \frac{f X_c}{U_\infty} \quad (1.3)$$

For the length scale  $X_c$ , the length of the separated region or usually the chord length for the flow separation at the leading edge of an airfoil is used.

## 1.2 Open-Loop Control

Recent papers (Glezer & Amitay, 2002; Greenblatt & Wygnanski, 2000) have reviewed a variety of open-loop unsteady actuation strategies to reattach separated flows on airfoil. For example, Seifert *et al.* (1993) used oscillatory blowing to delay flow separation from a NACA0015 airfoil at angles of attack from  $\alpha = 12^\circ$  to  $14^\circ$ . This results in a 68% increase and a 32% decrease in the mean lift and drag coefficients, respectively. Zhang *et al.* (2008) used surface perturbation using piezoceramic actuators on a NACA0012 airfoil to postpone the stall angle by  $3^\circ$  and significantly improve the airfoil performance for  $12^\circ \leq \alpha \leq 20^\circ$ .

The effective range of forcing frequencies in separation control has been investigated computationally and experimentally by many other researchers, where  $F^+ \approx O(1)$  can either delay separation or initiate an earlier flow reattachment (Raju *et al.*, 2008; Greenblatt & Wygnanski, 2000). Seifert *et al.* (2004) experimentally studied separation control at Reynolds numbers ranging from  $3 \times 10^4$  to  $4 \times 10^7$  and observed perturbations needs to be amplified over the region susceptible to separation at effective excitation frequencies that generate one to four vortices over the controlled region at all times, irrespective of Reynolds number. Seifert *et al.* (2004) indicated that the actuation frequency couples to and, in fact drives the shedding in the near wake. Actuation at these frequencies leads to the formation of vortical structures that scale with the length of the separated flow domain, and the ensuing changes in the rate of entrainment result in a Coanda-like deflection of the separating shear layer toward the surface of the stalled airfoil, such that the layer vortices are effectively advected downstream in close proximity to the surface. Similarly, Sosa *et al.* (2007) used plasma sheet actuators to generate electrohydrodynamic perturbations to the flow around an NACA0015 at Reynolds numbers of  $O(10^5)$  and found the optimal frequency  $F^+ \approx 0.4$ .

At sufficiently high angle of attack, the flow becomes fully separated at the leading edge, leading to the formation and shedding of large-scale vortical structures; the leading-edge vortex (LEV) and the trailing-edge vortex (TEV). The shedding of these vortices results in large oscillation of forces exerted on the airfoil. Unsteady actuation has also been used to change dynamics of the vortex

shedding from the leading and trailing edges at post-stall  $\alpha$ , leading to higher unsteady lift (Rullan *et al.*, 2006; Wu *et al.*, 1998). With leading edge actuation by means of pulsed vortex generator jets, Scholz *et al.* (2008) observed even higher normal forces than in prestall condition when the actuators were positioned in the region of separation. Using a Reynolds-averaged Navier-Stokes (RANS) computation of turbulent flow over a two-dimensional NACA0012 airfoil, Wu *et al.* (1998) showed that local unsteady forcing near the leading edge can lead to post-stall lift enhancement in a time-averaged sense. Also, Rullan *et al.* (2006) and Miranda *et al.* (2005) considered flow over sharp-edged airfoils to show that unsteady actuation can provide an average lift increase on the order of 50%.

### 1.3 Feedback Control

Feedback control methods are an attractive choice over passive and active open-loop controls in that the control is continuously modified according to the response of the flow system. A salient observation from control theory is that open-loop control cannot modify the dynamics of a linear system, meaning that feedback is required to stabilize a system or alter its fundamental response to inputs. In addition, feedback control is generally less sensitive to disturbances and uncertainties than open-loop methods, and adaptive and gain-scheduled controllers can be designed to adjust to changing flight conditions.

Although most of the references on post-stall flow control focus on open-loop studies, feedback control methods such as the single-sensor linear feedback control (Berger, 1967; Huang, 1996; Zhang *et al.*, 2004), optimal (Li *et al.*, 2003) and suboptimal controls (Min & Choi, 1999), and control based on reduced-order models (Siegel *et al.*, 2006) have been successfully applied in flow over a cylinder to suppress vortex shedding and stabilize wake unsteadiness (Kim & Bewley, 2007). For example, Zhang *et al.* (2004) developed a proportional-integral-derivative controller to suppress the in-phase vortex shedding and vortex-induced vibration on a spring-supported square cylinder at the resonance condition leading to an almost complete suppression of vortex shedding.

Feedback has also been successfully applied in the flow over open cavities to suppress the acoustic tones to background sound pressure levels (Rowley & Williams, 2006; Kegerise *et al.*, 2007*a,b*). For example, Cattafesta *et al.* (1997) found experimentally that feedback control with piezoelectric actuators required an order of magnitude of less power than open-loop forcing with the same actuator.

In the area of post-stall flow control, Pinier *et al.* (2007) experimentally considered a simple proportional feedback control of turbulent flow over a NACA4412 with leading-edge zero-net-mass-flux actuators. Pinier *et al.* (2007) validated the use of low-dimensional modeling techniques for developing more sophisticated controller designs as a promising solution for real-time flow separation control.

More recently, Ahuja & Rowley (2010) numerically investigated feedback control of two-dimensional flow over a flat plate at a low Reynolds number and at large angles of attack. Using a reduced-order estimator, Ahuja & Rowley (2010) were able to suppress stable periodic vortex shedding over a two-dimensional flat plate at  $Re = 100$ . Also, feedback control around a low-aspect-ratio wing at post-stall angles of attack was numerically investigated by Taira *et al.* (2010) at a low Reynolds number of 300 with blowing along the trailing edge. Motivated by the existence of time-periodic high-lift states under open-loop control with periodic excitation, Taira *et al.* (2010) considered the extremum seeking algorithm for designing feedback control to lock the flow onto such high-lift states.

## 1.4 Overview of Current Work

In this thesis, we first investigate a simple model of a purely translating flat plate at high angle of attack at a Reynolds number of 300, where strong, periodic vortex shedding occurs. A small amplitude body force intended to mimic oscillatory mass injection is applied near the trailing edge in order to modulate the vortex shedding.

Open-loop control with periodic pulsing at the natural shedding frequency is first investigated for various actuator configurations over a range of angle of attack,  $\alpha$ . In certain cases, primarily for lower  $\alpha$ , open-loop forcing results in a phase-locked limit cycle with lift varying at the frequency of

actuation. For sufficiently high  $\alpha$ , however, subharmonic frequencies are excited and a more complex limit cycle behavior is obtained. The period-averaged lift over one cycle of actuator forcing varies from cycle to cycle, and it is observed that higher lift is associated with a particular phase shift between the forcing and the lift. This period-averaged lift can exceed the maximum lift achieved during the natural shedding cycle, particularly for upstream blowing at the trailing edge during certain cycles. We show that feedback of the lift signal can be used to phase lock the forcing to the particular phase shift associated with the highest period-averaged lift. This feedback stabilizes the high-lift limit cycles that are otherwise unstable with open-loop control. Similar phase-locking feedback control has been used in the aforementioned study of Pastoor *et al.* (2008) and by Tadmor (2004).

Rather than optimizing the phase of the control relative to the lift using only a sinusoidal waveform, we investigate the possibility of optimizing the lift using more general (non-sinusoidal) actuation waveforms. We utilize a gradient-based approach that has been used previously in simulations to reduce the turbulent kinetic energy and drag of a turbulent flow in a plane channel (Bewley *et al.*, 2001), or to reduce free-shear flow noise (Wei & Freund, 2006). Given the DNS for a particular actuator waveform, we solve the adjoint of the perturbed linearized equations backward in time to determine the sensitivity of the lift to the actuator input, and subsequently use this information to iteratively improve the control.

Optimization provides a periodic waveform with a high lift after a couple of transient periods. This optimal waveform was not a continuous sinusoid, but a pulsatile waveform roughly in phase with the maximum lift. However, if the (periodic) optimal waveform is extracted and applied in open loop, the flow fails to lock on and the subharmonic resonances degrade the performance. A receding horizon control approach could be used to keep the flow locked on, but since this computed optimal control requires knowledge of the full flow state, it is not practical for real-time control. To overcome these obstacles, we design a controller that uses the previously developed phase-locking strategy, but is applied to the more complicated waveforms deduced by the optimization. This provides a robust and practical approach to giving near-optimal performance. Also the feedback is able to phase

lock an arbitrary waveform at a particular phase shift, enabling us to investigate the lift response to various control waveform. Motivated by the pulsatile waveform the optimization provided, we investigate the lift response to pulses of different duty cycles. The feedback is used to enforce the optimal phase shift (approximately in phase) for each control waveform. We find that the pulse with a duty cycle of 25% achieves similar average lift enhancement as a continuous sinusoid when the forcing is in phase with the lift.

Finally, we consider a higher  $Re$  of 3000 and investigate the lift response to different waveforms motivated by the nature of the optimal forcing found at  $Re = 300$ . Geometry of flat plate with a thickness-to-chord ratio of 4% and  $Re$  are chosen to match the experiments by Greenblatt *et al.* (2008). We consider different frequencies and actuation waveforms with different duty cycles. We show that for certain frequencies and actuator waveforms, there occur stable limit cycles in which the flow is phase locked to the actuation. Forcing with duty cycle of 5% is as effective as higher duty cycles or a continuous sinusoidal. Also, as the duty cycle is increased, the range of forcing frequencies for the phase-locked limit cycles decreases.

In the next chapter, we present the simulation methodology and the actuation scheme. Results from sinusoidal forcing will be discussed in Chapter 3. Once the objective of our control is defined, we formulate an adjoint-based optimization in Chapter 4. Then we design a feedback algorithm where the optimized waveform is shifted or deformed periodically to adjust to the output frequency of the flow. We show that the feedback controller achieves as high lift as the optimization, and can be started from any phase of the natural shedding cycle. Then the feedback control with optimized waveform is directly compared to the sinusoidal forcing case.

Finally, in Chapter 5, we apply the tools developed and the knowledge gained at  $Re = 300$  to a  $Re$  of 3000, closer to MAVs operating condition, on a thin airfoil with a thickness-to-chord ratio of 4%.

## Chapter 2

# Numerical Methods

### 2.1 Fast Immersed Boundary Method

The numerical scheme used is a fast immersed boundary method developed by Colonius & Taira (2008), and is briefly described here. Consider the following form of the incompressible Navier-Stokes equations, based on the continuous analog of the immersed boundary formulation introduced by Peskin (1972):

$$\frac{\partial u}{\partial t} + u \cdot \nabla u = -\nabla p + \frac{1}{Re} \nabla^2 u + \int f(\xi) \delta(\xi - x) d\xi, \quad (2.1)$$

$$\nabla \cdot u = 0, \quad (2.2)$$

$$u(\xi) = \int u(x, t) \delta(x - \xi) dx = u_B, \quad (2.3)$$

where  $u$ ,  $p$ , and  $f$  are the appropriately non-dimensionalized fluid velocity, pressure and surface force respectively. The force  $f$  acts as a Lagrange multiplier that imposes the no-slip boundary condition on the Lagrangian points  $\xi$ , which arise from the discretization of a body moving with velocity  $u_B$ . We consider the body to be a stationary flat plate at an angle of attack  $\alpha$ ; that is, here  $u_B = 0$ , except at the actuation points where  $u_B = U_j$ .

The variables  $u$  and  $x$  are non-dimensionalized with respect to the freestream velocity  $U_\infty$  and the flat plate chord length  $c$ , and the Reynolds number is defined as  $Re = Uc/\nu$  where  $\nu$  is the kinematic

viscosity. The other quantities pressure  $p$ , force  $f$ , and time  $t$  are consistently non-dimensionalized as  $p/\rho U_\infty^2$ ,  $f/\rho U_\infty^2 c$ , and  $U_\infty t/c$ , respectively. Equations (2.1 - 2.3) are discretized in space using a second-order finite-volume scheme on a staggered grid, which results in the following semi-discrete equations:

$$M \frac{dq}{dt} + Gp - Hf = n(q) + Lq + dc_1, \quad (2.4)$$

$$Dq = bc_2, \quad (2.5)$$

$$Eq = 0, \quad (2.6)$$

where  $q$ ,  $p$ , and  $f$  are the discrete velocity flux, pressure, and force respectively. The operator  $n(q)$  is the discretized nonlinear term  $u \cdot \nabla u$ ,  $L$  is the discrete Laplacian, and  $M$  is the diagonal mass matrix, which is the identity for a uniform grid. The operators  $G$  and  $D$  are the discrete gradient and divergence operators constructed such that  $G = -D^T$ , and the operators  $E$  and  $H$  are interpolation and regularization operators that smear the Dirac delta functions in equation (2.1) over a few grid points. In order to obtain a symmetric matrix in the Poisson solve obtained on temporal discretization, these operators are also constructed such that  $E = -H^T$  (see Taira & Colonius (2007) for details). The terms  $bc_1$  and  $bc_2$  depend on the particular choice of boundary conditions. For example, for a 2-D flow past a stationary object, uniform flow conditions can be applied at the inlet and at the lateral walls, and convective boundary conditions can be applied at the outflow.

Equations (2.4 - 2.6) are then discretized in time using an implicit trapezoidal scheme for the linear terms and the second-order accurate Adams-Bashforth for the nonlinear terms. The resulting algebraic equations are solved using a fractional-step algorithm to march the variables forward in time. The key feature of this technique is that the pressure  $p$  and the force  $f$  are combined together as a single Lagrangian multiplier  $\lambda = (p, f)$ , which can be obtained by solving a single modified Poisson equation.

A fast algorithm of the above immersed boundary method was developed by Colonius & Taira (2008) by employing a nullspace approach and a multi-domain method for applying the far-field boundary conditions. The discrete streamfunction  $s$  is introduced, which is related to the flux  $q$  by a discrete curl operation  $C$  constructed as the nullspace of the divergence  $D$ :

$$q = Cs, \text{ where, } DC \triangleq 0. \quad (2.7)$$

Thus, the incompressibility condition (2.5) is satisfied at all times. The transpose operator  $C^T$  relates the discrete circulation  $\gamma$  to the discrete flux by:

$$\gamma = C^T q. \quad (2.8)$$

Pre-multiplying (2.4) by  $C^T$  eliminates the pressure, since  $C^T G = -C^T D^T = 0$ , resulting in a semi-discrete formulation in terms of the circulation  $\gamma$ :

$$\frac{d\gamma}{dt} + C^T E^T \tilde{f} = -\beta C^T C \gamma + C^T n(q) + bc_\gamma, \quad (2.9)$$

$$ECs = u_{jet}, \quad (2.10)$$

$$(2.11)$$

where a uniform grid is assumed (that is  $M = I$ ) in (2.4). In (2.9), the discrete Laplacian is represented by  $-C^T C \gamma$ , using the identity  $\nabla^2 \gamma = \nabla(\nabla \cdot \gamma) - \nabla \times (\nabla \times \gamma) = -\nabla \times (\nabla \times \gamma)$ ; the constant  $\beta = 1/Re\Delta^2$ , where  $\Delta$  is the uniform grid spacing. The nonlinear term  $n(q)$  is the spatial discretization of  $q \times \gamma$ . From (2.7) and (2.8), the discrete streamfunction  $s$  and circulation  $\gamma$  can be related by

$$s = (C^T C)^{-1} \gamma. \quad (2.12)$$

The boundary conditions specified are Dirichlet and Neumann for the velocity components normal and tangential to the domain boundaries, which for the flow past a flat plate imply a uniform flow in the far field. With a uniform grid and these boundary condition, the Laplacian  $C^T C$  can be diagonalized using the fast Sine transform:

$$L = C^T C = S \Lambda S, \quad (2.13)$$

where,  $S$  is the symmetric operator representing the discrete Sine transform and  $\Lambda$  is a diagonal matrix containing eigenvalues of  $C^T C$ . Equations (2.9, 2.10) are then discretized in time, using the trapezoidal rule for the linear terms and the second-order Adams-Bashforth for the nonlinear terms to obtain the timestepping scheme:

$$S(1 + \frac{\beta \Delta t}{2} \Lambda) S \gamma^* = (I - \frac{\beta \Delta t}{2} C^T C) \gamma^n + \frac{\Delta t}{2} (3n(q^n) - n(q^{n-1})) + \Delta t b c_\gamma, \quad (2.14)$$

$$EC(S \Lambda^{-1} (1 + \frac{\beta \Delta t}{2} \Lambda)^{-1} S) (EC)^T \tilde{f} = EC S \Lambda^{-1} S \gamma^* - u_B^{n+1}, \quad (2.15)$$

$$\gamma^{n+1} = \gamma^* - S(1 + \frac{\beta \Delta t}{2} \Lambda)^{-1} S (EC)^T \tilde{f}, \quad (2.16)$$

where the index  $n$  represents the fields at time  $t_n = n \Delta t$ . The dimension of the Poisson equation (2.15) to solve for the force  $\tilde{f}$ , is much smaller than the corresponding equation to solve for pressure  $p$  required in the scheme resulting from a similar temporal discretization of (2.4-2.6). This results in an algorithm that is much faster (for stationary bodies) than that resulting from the temporal discretization of (2.4-2.6).

The above boundary conditions are valid only for a sufficiently large domain, however with a uniform grid, large domain could result in a large number of grid points. In order to circumvent this problem, Colonius & Taira (2008) developed a multi-domain approach to apply simple far-field boundary conditions. The domain around the immersed body is considered to be embedded in a series of domains, each twice as large as the preceding, with a uniform but a coarser grid having

the same number of grid points as illustrated in Fig. 2.1. The circulation field on the smallest is first coarsified or interpolated onto the next larger mesh. The Poisson equation (2.12), with zero boundary conditions, is solved on the largest domain to obtain the streamfunction. This solution is then interpolated to obtain the boundary values of the next smaller domain, which are in turn used as boundary conditions to solve the Poisson equation on the smaller domain. The immersed body is assumed to be present only in the smallest domain, which consists of a fine mesh in the region of interest around the body. For the model problem of two dimensional flow past a flat plate, the typical size of the largest domain is around 40 chord lengths in each direction, and the number of domains ranges from 3 to 5. The operators for interpolating between different levels of domains are carefully designed to preserve the total circulation. The cost of the method increases due to the multi-domain implementation, as the Poisson equation (2.12) is required to be solved at least once for each domain, however, the overall cost benefit due to the elimination of pressure and use of the fast Sine transform results in an overall speed-up by an order-of-magnitude over the previous algorithm of Taira & Colonius (2007).

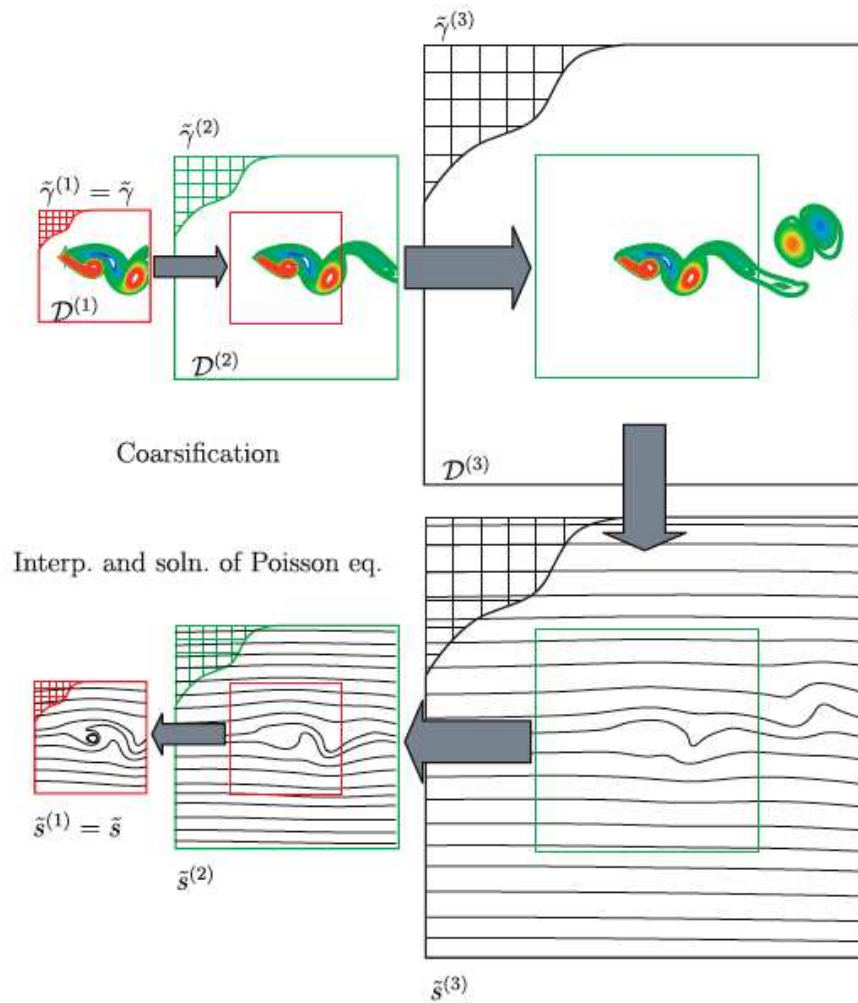


Figure 2.1: Multi-domain method to solve the Poisson equation. Figure reproduced with permission from Colonius & Taira (2008).

## Chapter 3

# Sinusoidal Forcing at $Re = 300$

In this chapter, we first investigate open-loop control at the leading and trailing edges directed upstream or downstream parallel to the freestream. We find that, for upstream actuation at the trailing edge, certain phase shifts between the forcing and lift signals result in very high period-averaged lifts. Thus, we design the feedback in order to adjust the frequency of the actuation accordingly to keep the phase shift constant and reproduce the high-lift shedding cycles.

### 3.1 Numerical Method

Simulations of flow over a two-dimensional flat plate at  $Re = 300$  are performed with the immersed boundary projection method combined with a multi-domain technique (Taira & Colonius (2007); Colonius & Taira (2008) described in Chapter 2). This method is capable of resolving incompressible flows over an arbitrarily-shaped body in motion and deformation. Here we employ this method with the flat plate being stationary. In what follows, all velocities and length scales are nondimensionalized by the freestream velocity and the chord,  $U_\infty$  and  $c$ , respectively.

The numerical method utilizes a series of overlapping uniform Cartesian grids of differing resolution. The finest grid, encompassing the body, is comprised of a rectangular domain extending to  $[-1, 4] \times [-1.5, 1.5]$  in the streamwise ( $x$ ) and vertical ( $y$ ) directions with a uniform grid spacing of 0.02 units. The constant time step was 0.004. The coarsest grid extended to  $[-8, 32] \times [-12, 12]$ . The boundary condition at the outermost grid was that the streamfunction corresponding to the

difference between the full velocity and a uniform free stream was zero. Selected cases were run on finer grids and with larger extents to demonstrate convergence and independence to far-field boundary conditions.

The lift and drag coefficient on the flat plate is defined by

$$C_L = \frac{F_y}{\frac{1}{2}\rho U_\infty^2 c} \quad \text{and} \quad C_D = \frac{F_x}{\frac{1}{2}\rho U_\infty^2 c}, \quad (3.1)$$

where  $\rho$  is the freestream density of the fluid and  $F_y$  and  $F_x$  are lift and drag on the plate, respectively, obtained by summing over surface forces in  $y$ -direction,  $\tilde{f}_y$  or in  $x$ -direction,  $\tilde{f}_x$ . Since the force obtained is normal to the plate and  $F_y$  is only the vertical component of the normal force, the increase of the normal force increases both the lift and drag. As the angle of attack increases, the drag component of the normal force is increased while the lift component is reduced. For high angles of attack, this might result in decrease of the lift-to-drag ratio even in the presence of lift enhancement. However, for the purpose of demonstrating the control algorithm to achieve high lift, we will pay closer attention to the lift component of the normal force,  $C_L$ .

In practice, actuators produce a jet-like flow that can lead to complex spatial and temporal characteristics. However, for the purpose of investigating the control of shedding, we model the actuation as a point body force regularized across 3 cells in both  $x$ - and  $y$ -directions with a discrete delta function (Taira & Colonius, 2009a) and define its strength by specifying the magnitude of its velocity,  $U_j$  in the direction of forcing. In defining the momentum injection added by the forcing, the width of the actuator is estimated as the grid spacing,  $\Delta x$ . The momentum coefficient, defined in Eq. (3.2), is the ratio between the momentum injected by the forcing and that of the freestream.

$$C_\mu = \frac{\overline{\rho U_j(t)^2} \Delta x}{\frac{1}{2}\rho U_\infty^2 c} \quad C'_\mu = \frac{\rho \langle U_j(t) \rangle^2 \Delta x}{\frac{1}{2}\rho U_\infty^2 c}. \quad (3.2)$$

The values of  $C_\mu$   $C'_\mu$  reported are based on the average and the root mean square of control input,  $\overline{U_j(t)}$  and  $\langle U_j(t) \rangle$ , respectively, fixed at 0.5, and the width of the actuator,  $\Delta x = 0.02$ . This corre-

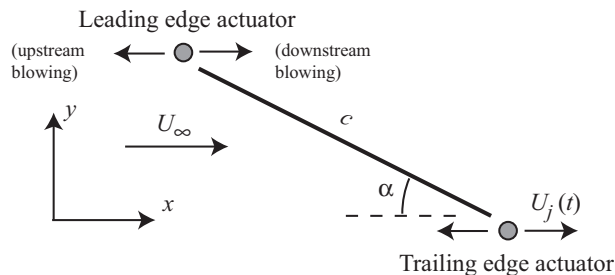


Figure 3.1: Schematic of actuation at leading and trailing edge.

sponds to a fixed  $C_\mu$  of 0.01 for all of the cases considered here. For each actuation location, two cases of blowing angles are considered, one directed downstream and the other directed upstream as illustrated in Figure 4.1.

## 3.2 Results

In this section, uncontrolled flow is first described followed by results from open-loop control with periodic pulsing for various actuator configurations over a range of  $\alpha$ .

### 3.2.1 Uncontrolled Flow

For the translating flat plate at  $Re = 300$ , steady attached flow is observed for  $\alpha < 10^\circ$ . At  $\alpha = 10^\circ$ , the flow is observed to be separated but remains steady. The flow undergoes a Hopf bifurcation between angles of attack of  $12^\circ$  and  $15^\circ$ , Colonius *et al.* (2006) after which vortex shedding occurs with natural shedding frequency,  $\omega_n$ , which varies from 3.65 at  $\alpha = 15^\circ$  to 1.39 at  $\alpha = 50^\circ$ . Using the vertical projection of the airfoil to the freestream, we find that  $\omega_n$  can be scaled, for  $\alpha \geq 30^\circ$ , to a Strouhal number of  $St = f_n c \sin(\alpha) / U_\infty \approx 0.2$ , where  $f_n = \omega_n / (2\pi)$ . This agrees with the wake Strouhal number for vortex shedding behind two-dimensional bluff bodies (Roshko, 1961; Bearman, 1967; Griffin, 1978). The unsteady shedding cycle consists of vortices of opposite signs alternately shed from the leading and trailing edges, creating periodic oscillations in the lift and drag. As  $\alpha$  is increased, larger vortex structures are formed, inducing a larger amplitude of oscillation in the force

exerted on the plate. For  $\alpha \geq 30^\circ$ , the vortex structure on the suction side of the plate is observed to be created from the leading edge and can be viewed as a transient LEV, or, similarly, a dynamic stall vortex (DSV) that occurs during a rapid pitch up. Maximum lift is found when the LEV is brought down to the suction side of the plate as it grows in strength. The lift decreases as the new vortex structure of the opposite sign is formed at the trailing edge. This trailing-edge vortex (TEV) pushes up the LEV sitting on the suction side of the plate, and finally halts its growth causing it to pinch-off and shed into the wake.

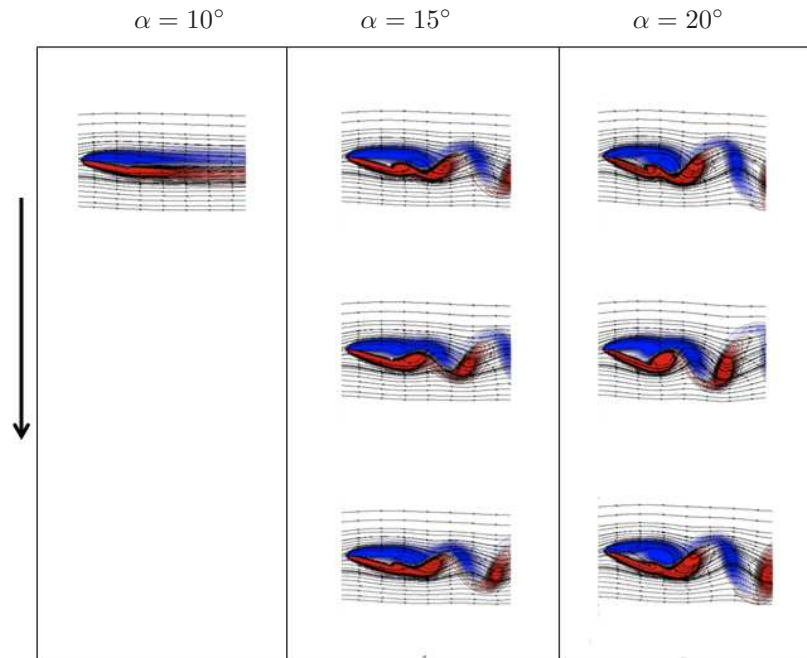
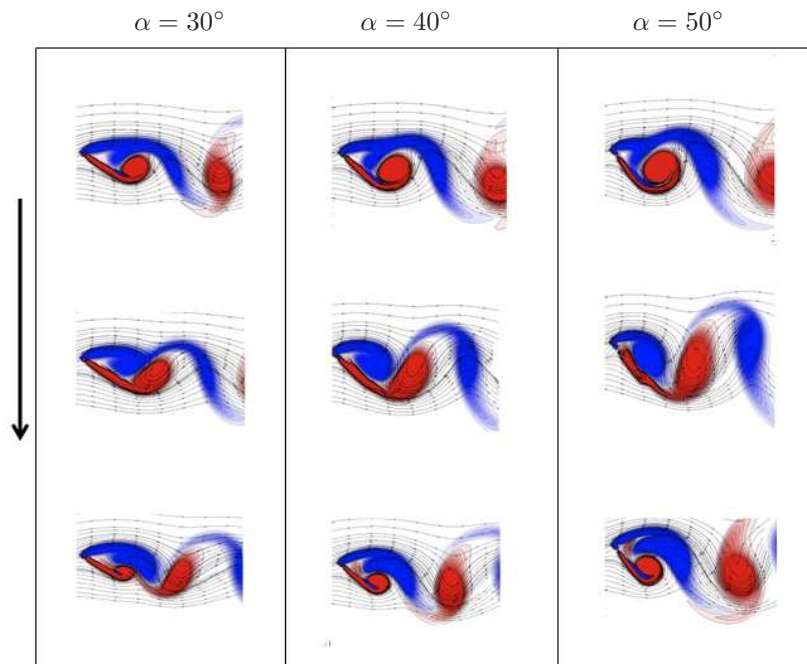
### 3.2.2 Open-loop control

In order to investigate the effect of unsteady blowing on these vortex shedding cycles, we first consider open-loop control using periodic pulsing with different blowing angles at the leading and trailing edge of the plate. The nondimensional jet velocity is set as  $U_j = \bar{U}_j + U'_j \sin(\omega_f t)$ , where  $\bar{U}_j = 0.5$  and  $U'_j = 0.5$ . Since this study is focused on maximizing lift from shedding of the coherent vortex structures rather than the suppression of shedding or separation,  $\omega_f$  is initially chosen to be the natural shedding frequency for each  $\alpha$ , at which the unsteady shedding of the large coherent vortex structure will likely be amplified the most (Glezer *et al.*, 2005; Amitay & Glezer, 2002). In the next two sections we examine leading and trailing edge actuation, respectively.

#### 3.2.2.1 Leading-edge actuation

Figure 3.3 shows the lift coefficient with actuation at the leading edge directed downstream (top) and upstream (bottom). In each figure, the uncontrolled flow (baseline) is overlaid in grey with its average in dashed grey and its maximum and minimum bounding the shaded region. Squares show the minimum and maximum of the lift signal whose overall average is shown in the circles in between. For cases where the lift is not phase locked to the forcing signal, variation in the period-averaged lift (averaged over each actuation period) is also plotted with an error bar.

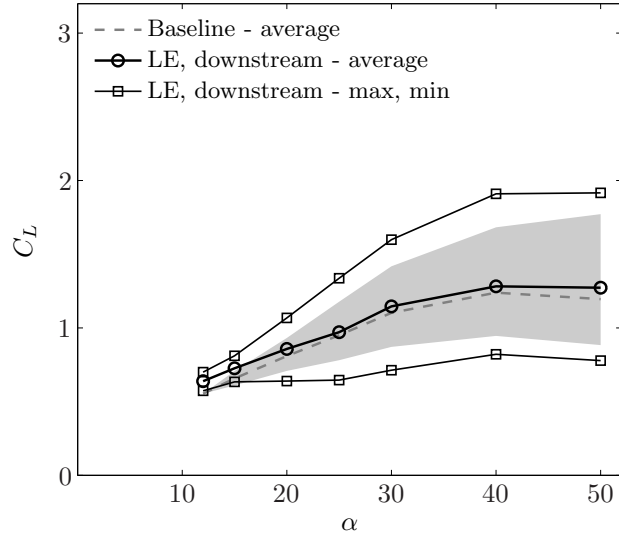
Blowing downstream provides extra momentum at the leading-edge in addition to that of the freestream. This amplifies the unsteady shedding of vortex structures, resulting in larger magnitudes

(a) Vorticity flowfield at  $\alpha = 10^\circ$ ,  $15^\circ$ , and  $20^\circ$ (b) Vorticity flowfield at  $\alpha = 30^\circ$ ,  $40^\circ$ , and  $50^\circ$ Figure 3.2: Vorticity and streamlines of translating flat plate at different angle of attack,  $\alpha$  at  $Re = 300$ .

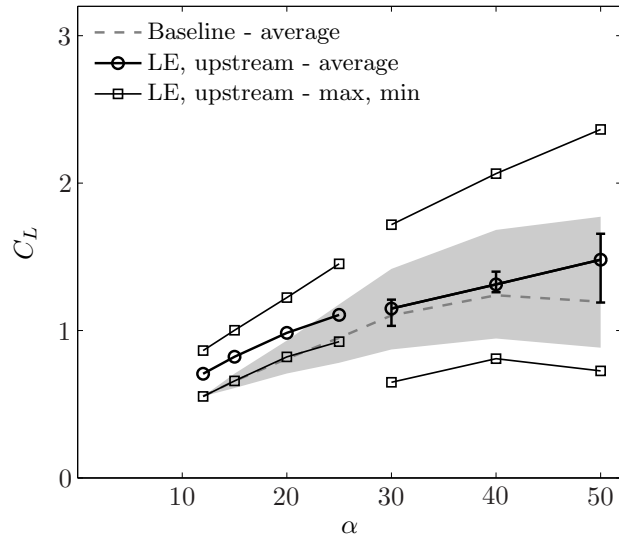
of the lift fluctuations. The forced flow exhibits higher maximum lift but also lower minimum lift, below that of the baseline flow. As a result, blowing downstream does not significantly benefit the overall average lift.

However, when the actuation is directed upstream, the resulting amplification of the unsteady shedding has a more positive effect on the average lift. For  $\alpha < 25^\circ$ , the flow locks onto the forcing  $2 \sim 3$  periods after the actuation is initiated. However at higher  $\alpha$ , the flow fails to lock onto the forcing frequency and displays a more complicated limit cycle, with subharmonics of the forcing frequency also excited. An example is shown in Figure 3.4, at  $\alpha = 50^\circ$  where each subharmonic limit cycle consists of several periods with a different period-averaged lift. Figure 3.4 also shows the lift as a function of the jet velocity, and shows that the actuation produces the highest lift when  $U_j$  is in phase with the  $C_L$  (maximum  $C_L$  when  $U_j$  is maximum). However, the succeeding period becomes slightly out of phase and the lift decreases. Each period within the subharmonic limit cycle is observed to be associated with a particular phase shift,  $\phi$ , between the forcing signal and the lift, yielding a particular period-averaged lift. The actuation period associated with the highest average lift is plotted in a thicker line. At each  $\alpha$ , there is a particular  $\phi$ , resulting in the highest average lift over an actuation period. If the feedback allows us to accordingly adjust the frequency of actuation to phase lock the flow at these  $\phi$ , then we could repeatedly produce the highest average lift period. This feedback design will be revisited later.

It might be counter-intuitive that upstream actuation at the leading edge achieves such a lift enhancement and performs better than downstream actuation. However, experiments at Reynolds number of the order of  $3 \times 10^5$  by Rullan *et al.* (2006) demonstrated that unsteady blowing upstream, parallel to the chord at the leading-edge of a sharp-edged, circular arc airfoil at various  $\alpha$  beyond stall leads to averaged pressure distribution that resulted in higher lift than that of the baseline flow. They achieved lift increase as high as 30% with momentum coefficient of  $C_\mu' = C_\mu / \sin(\alpha) \approx 1\%$ , scaled with the vertical projection of the airfoil and the actuation pulsating at the shedding frequency of the airfoil.

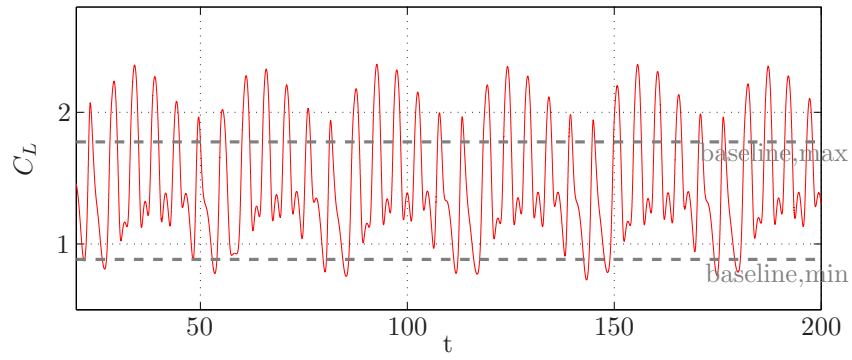


(a) downstream

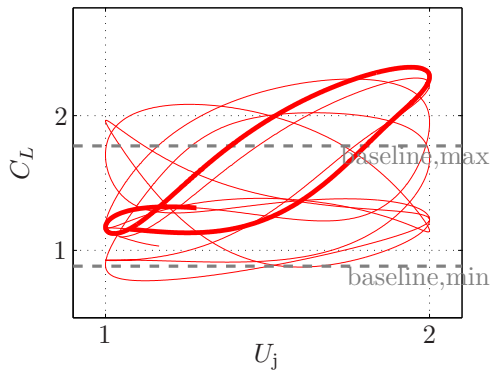


(b) upstream

Figure 3.3: Leading-edge actuation: maximum and minimum lift ( $\square$ ) and its average over time ( $\circ$ ) for downstream (left) and upstream (right) actuation. Average of the baseline case is plotted in dashed grey and shaded region is bounded by its maximum and minimum. Actuation is applied at the natural shedding frequency,  $\omega_f = \omega_n$ . For cases where the flow is not phase locked to the forcing signal, variation in period-averaged lift over each actuation period is plotted with error bar to indicate the range of values over a subharmonic limit cycle.



(a)



(b)

Figure 3.4: Lift as a function of time (a) and jet velocity (b) with upstream actuation at the leading edge (LE, upstream) at the natural shedding frequency ( $\omega_f = \omega_n$ ) for  $\alpha = 50^\circ$ .

### 3.2.2.2 Trailing-edge actuation

In Figure 3.5, the lift performance of the open-loop actuation at the natural shedding frequency at the trailing edge is investigated in a similar manner as in Figure 3.3. Blowing downstream exerts a negative effect on the average lift, yielding a lower minimum lift than that of the baseline flow with a similar maximum lift. However, when the forcing is directed upstream, the forced flow displays a significant lift enhancement. The forcing excites the vortex shedding cycle even for  $\alpha$  below the Hopf bifurcation. For  $\alpha \leq 15^\circ$ , the flow locks onto the forcing after  $2 \sim 3$  periods. However, for  $\alpha \geq 20^\circ$ , the subharmonic resonance is excited. This is similar to the observation with upstream blowing at the leading edge, but the subharmonic resonance is excited at a lower  $\alpha$  for the trailing-edge actuation than that for the leading-edge actuation.

Each period within the subharmonic limit cycle is again observed to be associated with a particular  $\phi$ , resulting in a particular period-averaged lift. We denote the  $\phi$  associated with the highest period-averaged lift at each  $\alpha$  as  $\phi_{\text{best}}$ . Particularly at  $\alpha = 30^\circ, 40^\circ$ , and  $50^\circ$ ,  $\phi_{\text{best}}$  was observed to be approximately  $-0.25, -0.05$ , and  $0.0$  radians, respectively. For trailing-edge actuation, the period-averaged lift at high  $\alpha$  is, in many cases, greater than the maximum lift occurring in the baseline flow. This suggests a greater potential for the trailing-edge feedback actuation to sustain the flow with the highest period-averaged lift. Consequently, we would obtain a phase-locked flow that has an average lift as high as the maximum lift of the baseline flow (or even higher).

In general, blowing upstream at both the leading and trailing edges create significant enhancement in the average lift. However, blowing upstream at the trailing edge provides a larger increase in lift than that of the leading-edge actuation. These findings are similar to observations made by Huang *et al.* (2004) who investigated the effect of blowing and suction control at various locations on the upper surface of a NACA0012 airfoil. They considered steady blowing and suction at  $Re = 5 \times 10^5$  and  $\alpha = 18^\circ$  and demonstrated that blowing at the leading edge directed downstream exerts a negative effect, decreasing lift and increasing drag at the same time, but suction increases lift by creating a larger and lower pressure zone on the airfoil's upper surface. They also observed

that the actuation near the trailing-edge on the upper surface,  $0.8c$  from the leading edge, improves lift and drag characteristics by manipulating the circulation of the TEV.

In order to understand the lift-enhancing mechanism of upstream actuation at the trailing edge, we compare the vorticity contours at the time of maximum lift for the cases of baseline and upstream actuation at the trailing edge, for  $40^\circ$  in Figure 3.8. Actuation feeds extra circulation to the TEV which induces a stronger downwash near the trailing edge. As a result, the vortex structure on the suction side is pulled down closer to the plate and the backflow near the trailing edge is reduced. Particularly at  $\alpha = 40^\circ$ , this delays the interference of the newly forming TEV with the LEV residing on the suction side. It also lengthens the duration over which the vortex structure is formed from the leading edge. These results also agree with the observations that the period associated with the highest lift within a subharmonic cycle in Figure 3.5(b) has a longer period than that of the baseline flow. This might indicate that there exists a forcing frequency below  $\omega_n$ , at which the flow becomes phase locked to the forcing at a higher lift than that of the baseline flow.

Thus, we next investigate the possibility of the existence of shedding cycles that are phase locked to the open-loop forcing signal. Figure 3.9 shows the lift response to the variation in open-loop forcing frequency for  $20^\circ \leq \alpha \leq 50^\circ$ , above which upstream actuation at  $\omega_f = \omega_n$  fails to phase lock the flow.

Over a range of frequency below  $\omega_n$ , the flow is phase locked to the actuation with its average lift near the maximum period-averaged lift of the flow actuated at  $\omega_f = \omega_n$ . As we go deeper into stall by increasing  $\alpha$ , the domain of attraction for the phase-locked limit cycle decreases, and finally at  $\alpha = 50^\circ$ , actuation failed to phase lock the flow over the range of forcing frequencies considered.

Figure 3.10 shows the corresponding phase shift,  $\phi$ , over this range of  $\omega_f$  that achieves a phase-locked flow for  $\alpha = 30^\circ$ . Recall that the subharmonic cycle (excited with upstream blowing at  $\omega_n$ ) consists of several actuation periods with a distinct  $\phi$  associated with a particular period-averaged lift. Also, its highest period-averaged lift is associated with  $\phi = \phi_{\text{best}} \approx -0.25$ . As  $\omega_f$  is decreased below  $\omega_n$ , the flow phase locks onto one of those periods observed in the subharmonic limit cycle at  $\alpha = 30^\circ$ . As  $\omega_f$  is decreased further, the flow is phase locked onto different periods with different

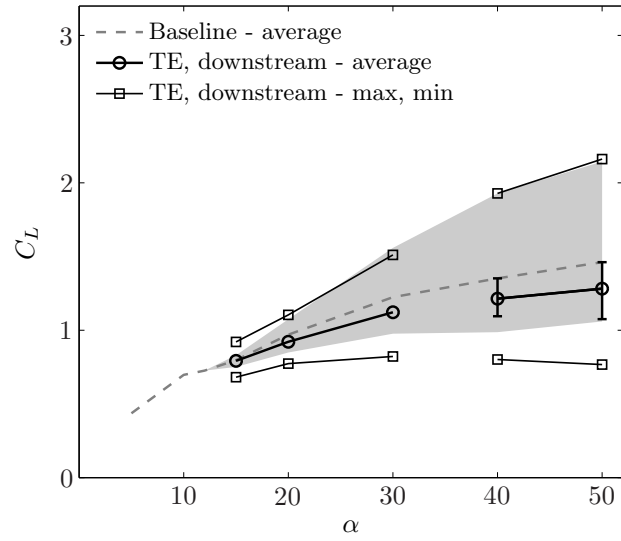
$\phi$ , closer to  $\phi_{\text{best}}$  with higher average lift. Finally, at  $\omega_f/\omega_n \approx 0.87$ , the actuation is able to lock the flow at the best period achieved with forcing at  $\omega_n$ . This indicates that each phase-locked limit cycle of the vortex shedding could be characterized by its frequency and the phase shift, yielding a particular maximum, minimum, and average lift.

If the feedback allows us to adjust the frequency of the actuation accordingly to keep the phase shift between the forcing signal and the lift constant (for example at  $\phi = \phi_{\text{best}}$ ), we should be able to reproduce the high-lift shedding cycles over a wide range of  $\alpha$ . Thus in order to achieve the desired phase-locked shedding cycle, we feedback lift into the controller, whose details are described in the next section.

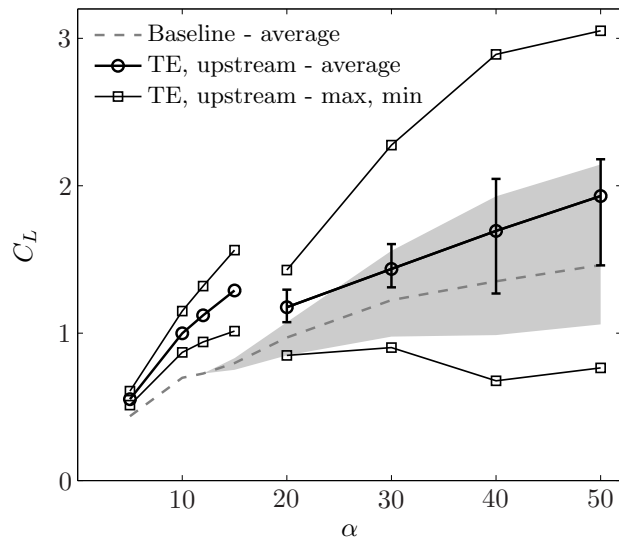
### 3.3 Closed-loop control

Open-loop periodic forcing can lead to limit cycles with a high average lift, but with a decreasing domain of attraction as  $\alpha$  increases. Our goal with closed-loop control is to obtain forced limit cycles with the maximum average lift. This involves stably maintaining limit cycles that are not stable without feedback.

Since the actuated flows with the highest average lift seem to be characterized by a distinct phase shift of the forcing relative to the lift at each  $\alpha$ , we feedback  $C_L$  in an attempt to phase lock the flow at these high-lift states. Direct feedback of  $C_L$  with appropriate gain would only allow us to force the flow to be in-phase with  $U_j$ . However, since the observed best phase shifts between  $C_L$  and  $U_j$  are negative, shifting direct feedback signal requires us to know the lift of the forced flow *a priori*. Instead, we assume that the lift signal being fed back is approximately sinusoidal. In such cases lift

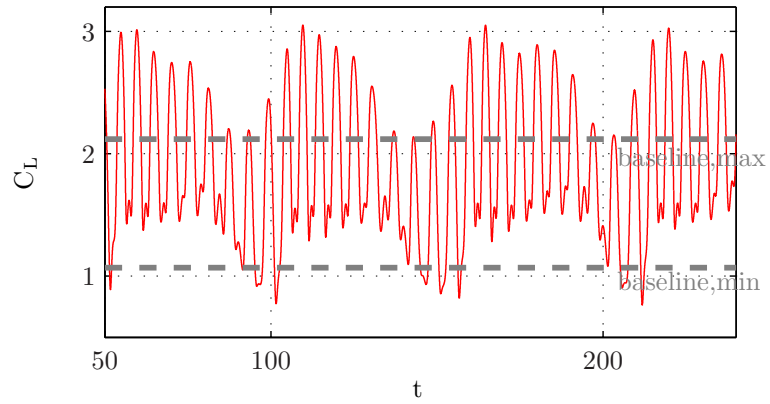


(a) downstream

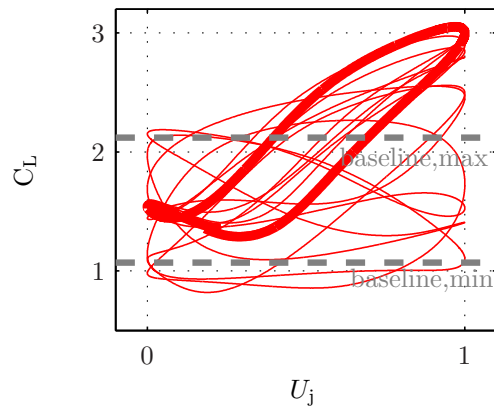


(b) upstream

Figure 3.5: Trailing-edge actuation: see Figure 3.3 for a description.



(a)



(b)

Figure 3.6: Lift with upstream actuation at the trailing-edge at its natural shedding frequency ( $\omega_f = \omega_n$ ), for  $\alpha = 50^\circ$ .

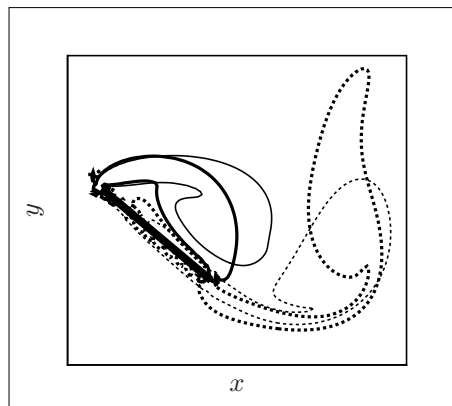


Figure 3.7: Vorticity contour at the time of maximum lift for baseline (thin) and upstream actuation (thick) at the trailing edge at the natural shedding frequency ( $\omega_f = \omega_n$ ). Dashed and solid lines represent counterclockwise and clockwise vorticity.

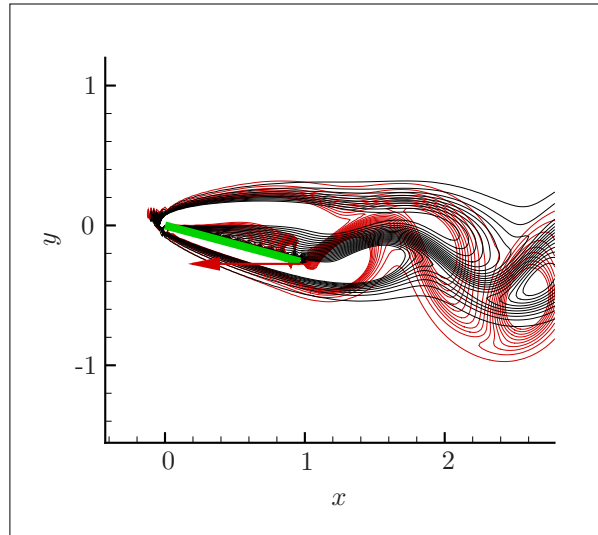
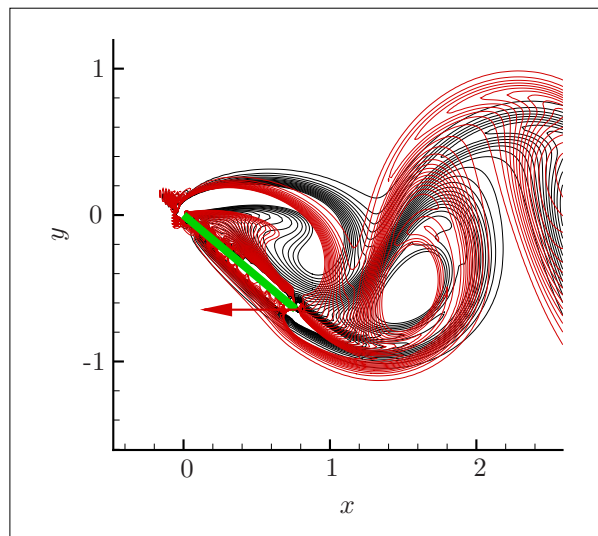
(a)  $\alpha = 15^\circ$ (b)  $\alpha = 40^\circ$ 

Figure 3.8: Vorticity contour at the time of maximum lift for baseline (black) and upstream actuation (red) at the trailing edge at the natural shedding frequency ( $\omega_f = \omega_n$ ).

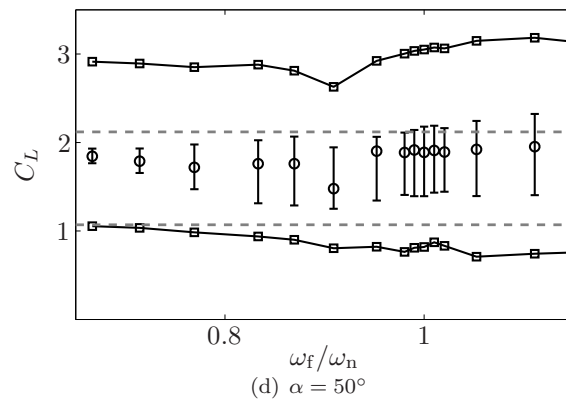
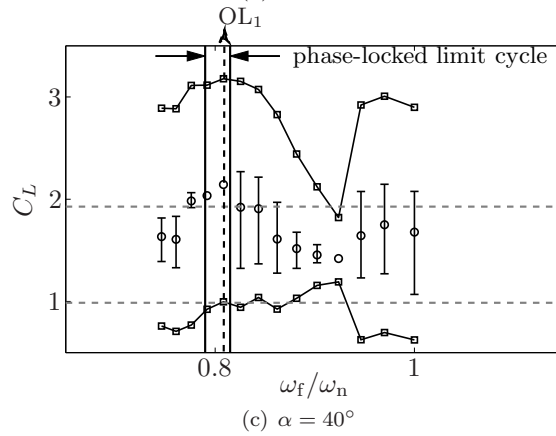
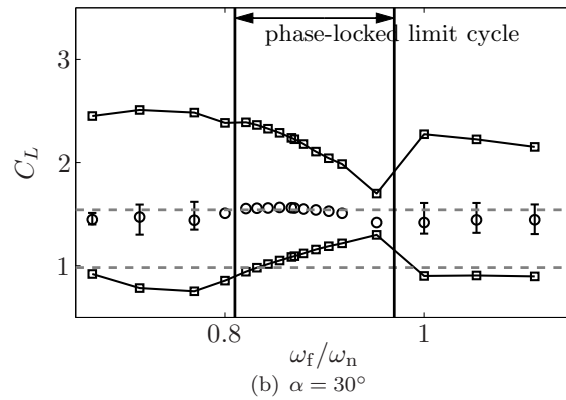
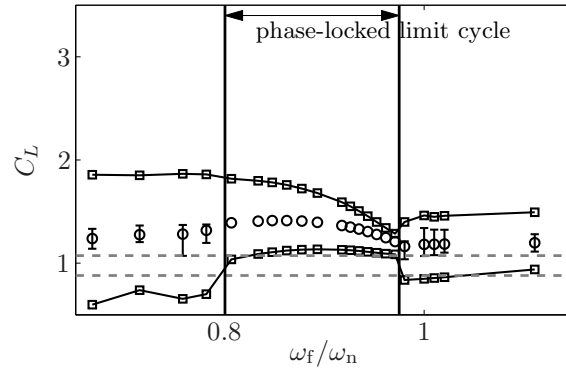


Figure 3.9: Trailing-edge actuation: maximum and minimum lift ( $\square$ ), average lift ( $\circ$ ), and period-averaged lift (error bar) over a range of open-loop forcing frequency,  $\omega_f$ . Maximum and minimum lift of baseline (---) case is shown as a reference.

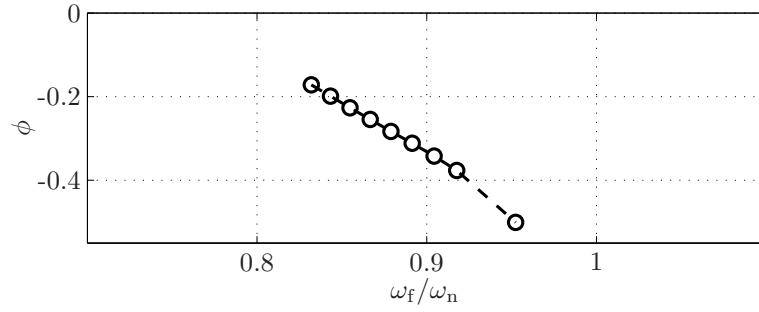


Figure 3.10: Trailing-edge actuation: phase shift of the forcing signal,  $U_j$ , relative to the lift signal,  $C_L$ , for phase-locked flows, over a range of open-loop forcing frequency,  $\omega_f$  ( $\alpha = 30^\circ$ ).

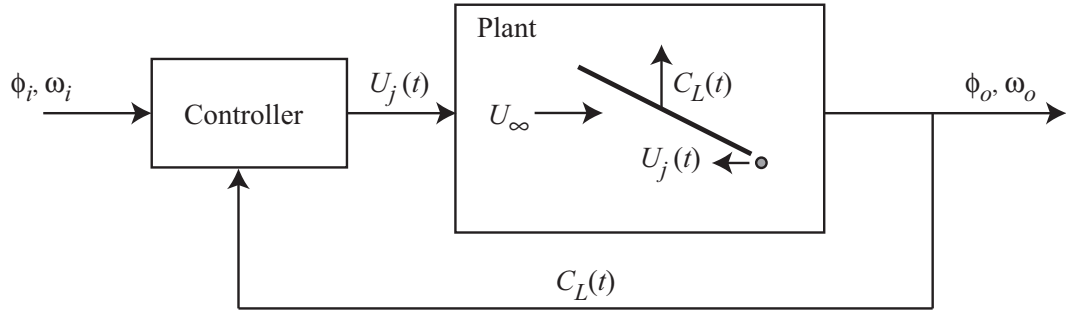


Figure 3.11: Feedback control configuration.

can be expressed as

$$\begin{aligned} C_L(t) &= a_0 + A_L \cos(\omega_i t + \theta), \\ &= a_0 + a_1 \cos(\omega_i t) + b_1 \sin(\omega_i t). \end{aligned} \quad (3.3)$$

Assuming that  $A_L$  and  $\theta$  are slowly varying in time, we can estimate  $a_1$  and  $b_1$  to be the Fourier mode over a moving window,

$$a_1(t) = \frac{2}{T_i} \int_{t-T_i}^t L(t') \cos(\omega_i t') dt', \quad (3.4)$$

$$b_1(t) = \frac{2}{T_i} \int_{t-T_i}^t L(t') \sin(\omega_i t') dt', \quad (3.5)$$

$$\omega_i = \frac{2\pi}{T_i}. \quad (3.6)$$

Then we feedback a phase-shifted version of this demodulated lift signal as the jet velocity,  $U_j$  with

appropriate gain,  $K_p$ ,

$$U_j(t) = a_0 + K_p(a_1(t) \cos(\omega_i t + \phi_i) + b_1(t) \sin(\omega_i t + \phi_i)), \quad (3.7)$$

where  $a_0$  is the average value of the output  $U_j$ , which can be prescribed as 0.5 to fix  $C_\mu = 0.01$ . We also adjust  $K_p$  continuously, such that the rms amplitude of  $U_j$  remains steady and similar to that of open-loop control, i.e.  $U_j$  varies from 0 to 1.

The configuration of our feedback control is shown in Figure 3.11. Lift is fed back to the controller which has two parameters: demodulation frequency,  $\omega_i$ , and the desired phase shift  $\phi_i$ . The controller outputs a sinusoidal  $U_j$  that is phase shifted relative to the dominant frequency of the lift signal. The flow system outputs  $C_L$ , which has a frequency  $\omega_o$  and a phase shift  $\phi_o$  relative to the input signal  $U_j$ .

If  $C_L$  is phase-locked to  $U_j$ , the frequency of  $U_j$  will always be the same as the frequency of  $C_L$ . However, if the demodulation frequency,  $\omega_i$  is not equal to the frequency of the lift signal,  $\omega_o$ , then  $\phi_o$  will be different from  $\phi_i$  (unless  $\omega_o = \omega_i$  in which case  $\phi_o = \phi_i$ ). Thus, it is necessary to add an integral part to the algorithm to adjust  $\omega_i$ , such that,

$$\omega_i^{k+1} = \omega_i^k + \beta(\omega_o^k - \omega_i^k). \quad (3.8)$$

We can adjust  $\omega_i$  until it reaches  $\omega_o$ , and thus obtain the exact desired phase shift and allow the frequency content to be determined only by the flow. Then we have a robust compensator to explore different limit cycles that are phase locked at various  $\phi$  at different  $\alpha$ .

Figure 3.12 investigates the sensitivity of the lift and the frequency of the forced phase-locked limit cycles to the changes in the phase shift,  $\phi$  at  $\alpha = 40^\circ$  and  $50^\circ$ . Feedback was able to phase lock the flow at any desired phase shift after  $2 \sim 5$  periods over a wide range of  $-0.5 \leq \phi \leq 0.5$ . At  $\alpha = 40^\circ$ , as shown in figure 3.12(a),  $FB_1$  corresponds to the limit cycle phase-locked to the actuation at  $\phi_{\text{best}}$ . However, the phase shift that achieved the highest average lift was not  $\phi_{\text{best}}$ . An

even higher-lift limit cycle was achieved near zero phase shift, resulting in as high as 83% increase in the average lift coefficient. A broad range of  $\phi$  ( $-0.28 \leq \phi \leq 0.06$ ) resulted in average lift that was higher than the maximum lift of the baseline flow, that is more than 45% in the average lift enhancement. At  $\alpha = 50^\circ$ , the highest average lift occurred near zero phase shift, and over a range of  $\phi$ ,  $-0.3 \leq \phi \leq 0.16$  the actuation achieved at least 25% enhancement over the average lift of the natural flow. At both  $\alpha$ 's, a larger range of negative phase shift contributed more to lift enhancement than the positive phase shift. Particularly at  $\alpha = 40^\circ$ , there was a sharp decrease in the lift after  $\phi = 0.06$  whereas the lift decrease was more gradual at the negative phase shift. In other words, having most of the control effort prior to the maximum lift (negative phase shift) does not penalize the average lift significantly. However, having the control peak after the maximum lift (positive phase shift) can significantly degrade the lift performance. Thus, forcing seems more effective as the newly forming LEV is pulled down by the TEV (lift-increasing phase). On the other hand, forcing seems the least effective after the maximum lift occurs; when the LEV sits closest to the plate and is pushed away by the growing TEV (lift-decreasing phase). As  $\phi$  approaches 0.5 or -0.5 (out of phase), the forced flow results in the average lift similar to that of an unforced flow, but with a slightly smaller magnitude of oscillation in lift coefficient. This sensitivity of the lift to the control effort during different phases of the vortex shedding cycle (particularly lift-increasing and -decreasing phases) will be revisited in the context of optimized waveform in the next Chapter.

Recall in Figure 3.9(c), we observe a very small domain of attraction near  $\omega_f \approx 0.8$  for the phase-locked limit cycle and the resulting limit cycle has a positive phase shift,  $\phi \approx +0.3$ . However, the phase-locked limit cycles achieved by this feedback have a wide range of frequencies, varying from 0.8 to 0.95 with the corresponding phase shifts ranging from  $-0.5$  to  $0.5$ . These limit cycles were not achieved by any of the forcing frequencies of the open-loop control in Figure 3.9(c). The feedback algorithm results in phase-locked limit cycles that are not attainable by the open-loop forcing.

Figure 3.13 compares the lift signal of the two limit cycles; the best open-loop case at  $\alpha = 40^\circ$ , denoted as  $OL_1$  in Figure 3.9(c) and the corresponding feedback case, denoted as  $FB_1$  in Figure 3.12. With open-loop control at fixed  $\omega_f$ , the flow seems to lock onto the actuation at the higher average

lift cycle during earlier periods, with its phase shift closer to  $\phi_{\text{best}}$ . But after a few periods,  $\phi$  drifts away from  $\phi_{\text{best}}$  and the flow eventually locks onto the lower average lift cycle. On the other hand, the feedback compensator prevents  $\phi$  from drifting away and sustains the phase at  $\phi_{\text{best}}$  producing higher average lift than the open-loop control. Thus, we can conclude that this feedback algorithm stabilizes the limit cycle with a significant lift enhancement that cannot be obtained with the open-loop control.

To ensure that the feedback is still required to sustain the achieved phase-locked limit cycle, FB<sub>1</sub> is investigated further. Feedback is turned off after the phase-locked limit cycle has been achieved for a long time, and the forcing signal is continued with the open-loop forcing at a fixed frequency,  $\omega_f$ , as shown in Figure 3.14. This behavior of unstable phase relationship has also been shown with an open- and closed-loop control model of an oscillating cylinder wake by Tadmor *et al.* (2004). Notice that when the forcing signal is continued with the actuation of  $\omega_f = \omega_{o,OL_1}$ , the flow drifts back to the previous open-loop limit cycle. When it is continued with actuation oscillating at  $\omega_f = \omega_{o,FB_1}$ , the average frequency of the previous feedback output signal, the flow displays a loss of phase-locking to this forcing frequency and it displays a pulling-out phenomenon. These results indicate that the feedback compensator was adjusting its forcing corresponding to the change of output frequency from the flow, and that the feedback is still required to sustain the flow at the high-lift limit cycle.

The feedback algorithm stabilizes the limit cycle with a significant lift enhancement that is not attainable by the open-loop forcing. Furthermore, even with careful tuning of the forcing frequency, open-loop forcing cannot sustain this high-lift limit cycle. Thus, the feedback achieves high-lift unsteady flow states that cannot be achieved or sustained without it.

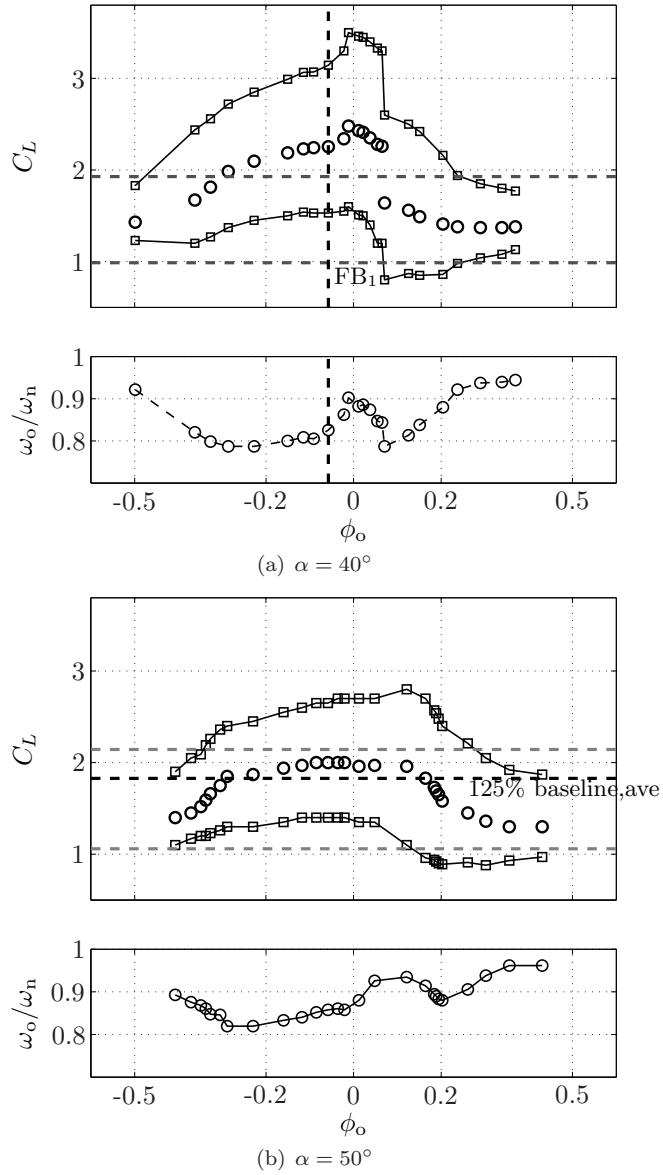


Figure 3.12: Maximum and minimum lift ( $\square$ ) and its average over time ( $\circ$ ) (top) and frequency (bottom) of phase-locked limit cycles at different phase-shift,  $\phi_o$ , for (a)  $\alpha = 40^\circ$  and (b)  $50^\circ$ .

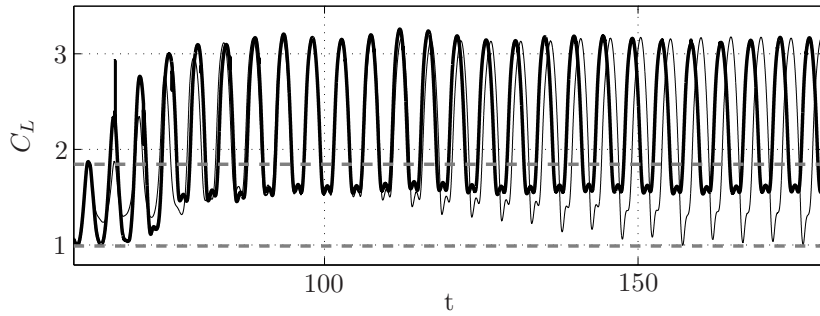
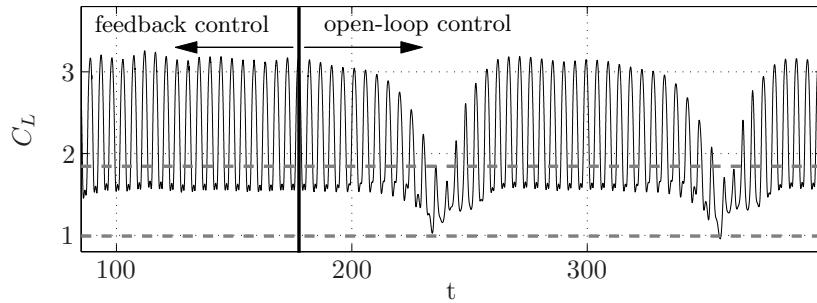
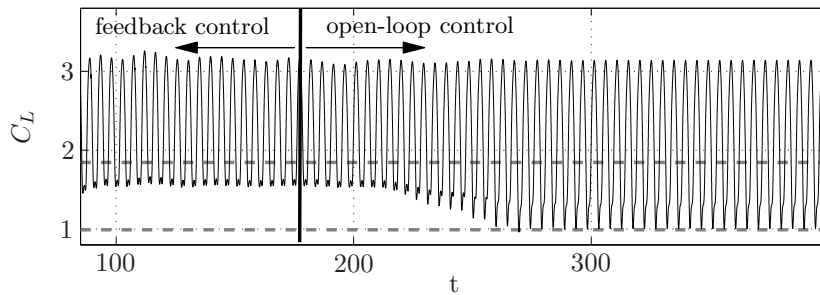


Figure 3.13: Comparison between open-loop control case (—), that phase locked the flow at the highest average  $C_L$  (denoted as  $OL_1$  in Figure 3.9(c)), and the corresponding feedback control case (---) (denoted as  $FB_1$  in Figure 3.12). Forcing frequency of this open-loop control is denoted as  $\omega_{f,OL_1}$ , and the average output frequency of  $C_L$  of the feedback control is denoted as  $\omega_{o,FB_1}$ .



(a)  $\omega_f = \omega_{o,FB_1}$



(b)  $\omega_f = \omega_{f,OL_1}$

Figure 3.14: Continuation of feedback control case in figure 3.13 with open-loop control of  $\omega_f$ .

## Chapter 4

# Optimized waveform at $Re = 300$

With the sinusoidal forcing and feedback, we showed that it is possible to optimize the phase of the control relative to the lift in order to achieve the highest possible period-averaged lift in a consistent fashion. However, continuous sinusoidal forcing could be adding circulation when it is unnecessary, or undesirable. For example, we showed in Sect. 3.3 that the control is more effective prior to the maximum lift than during the lift-decreasing phase. Thus, in this chapter, we use an adjoint-based optimization in order to find the waveform (time history of  $U_j$ ) that maximizes the lift for a given actuation amplitude. The adjoint of the linearized perturbed equations is solved backwards in time to obtain the gradient of the lift to changes in actuation (the jet velocity), and this information is used to iteratively improve the control. Optimal control provides a periodic control waveform, resulting in a high lift shedding cycle with minimal control input. However, if applied in open loop, the flow fails to phase lock onto the optimal waveform, degrading the lift performance. Thus, we also design a controller that uses the previously developed phase-locking strategy, but is applied to the more complicated waveforms deduced by the optimization. This feedback control of the optimized waveform is able to reproduce the high-lift limit cycle from the optimization, but started from an arbitrary phase of the baseline limit cycle. Motivated by the observation that the optimal waveform is close to a pulse, we investigate the response to pulses of different duty cycles. This is enabled by having a feedback strategy that allows us to lock the desired waveform onto the flow.

## 4.1 Numerical Method

Simulations of flow over a two-dimensional flat plate at  $Re = 300$  and an angle of attack of  $40^\circ$  are performed with the immersed boundary projection method combined with a vorticity-streamfunction multi-domain technique (Taira & Colonius, 2007; Colonius & Taira, 2008). We model the actuation as unsteady velocity boundary conditions  $\phi = U_j$  applied at the control point (trailing edge)  $\mathcal{C}$ .

For clarity, the incompressible viscous flow equations ((2.9) and (2.10)) is presented here in operator form by (4.2) and (4.3). The control is implemented as a velocity boundary conditions  $\phi(x, t)$  applied at the actuation points  $\mathcal{C}$  shown in Figure 4.1. In the case of our interest, control is a function only of time, and  $\phi(x, t) = \phi(t) = U_j(t)$ , which is the prescribed velocity at the actuation point.

Three vector fields are first defined: the flow state  $\mathbf{q}$ , the flow perturbation state  $\mathbf{q}'$ , and the adjoint state  $\mathbf{q}^*$ :

$$\mathbf{q} = \begin{pmatrix} \gamma \\ \tilde{f} \end{pmatrix}, \quad \mathbf{q}' = \begin{pmatrix} \gamma' \\ \tilde{f}' \end{pmatrix}, \quad \mathbf{q}^* = \begin{pmatrix} \gamma^* \\ \tilde{f}^* \end{pmatrix}. \quad (4.1)$$

where  $\mathbf{q}$  is a vector of flow variables and the motivation for introducing  $\mathbf{q}'$  and  $\mathbf{q}^*$  will be obvious later in the control derivation.

For clarity, all differential equations are written in operator form in this section. Incompressible viscous Navier-Stokes equation can be written in operator form as

$$\mathcal{N}(\mathbf{q}) = \mathbf{F}\phi \quad (4.2)$$

where the (nonlinear) operator  $\mathcal{N}(\mathbf{q})$  is

$$\mathcal{N}(\mathbf{q}) = \begin{pmatrix} \frac{d\gamma}{dt} + C^T E^T \tilde{f} + \beta C^T C \gamma - C^T n(q) - bc_\gamma \\ ECs \end{pmatrix}. \quad (4.3)$$

$\gamma$  is the discrete circulation and  $\tilde{f} = [\tilde{f}_x \quad \tilde{f}_y]^T$  is a vector of surface forces on the Lagrangian body points applied to satisfy the no-slip condition for a stationary body points or the prescribed velocity

for the actuation points. The vector  $\mathbf{F} = [\mathbf{F}_\gamma \quad \mathbf{F}_{\tilde{f}}]^T$  allocates the control action. Thus  $\mathbf{F}_\gamma = \mathbf{0}$  and  $\mathbf{F}_{\tilde{f}}$  has a single non-zero entry that corresponds to the actuator location associated with the appropriate element of the surface force,  $\tilde{f}$ .

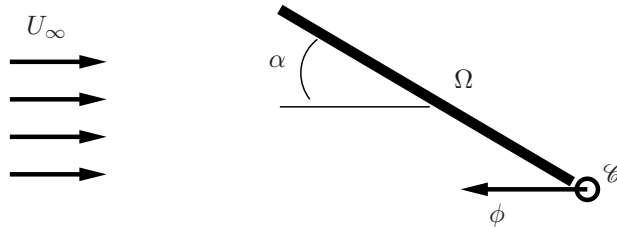


Figure 4.1: Schematic of upstream actuation at the trailing-edge.

## 4.2 Adjoint-based Optimization

We compute the optimal control over a time horizon, using the receding-horizon approach (Bewley *et al.*, 2001). The procedure is similar to previous studies (Bewley *et al.*, 2001; Wei & Freund, 2006) and is only outlined briefly here.

### 4.2.1 Adjoint-based Optimization: Cost Functional and Sensitivity

To maximize lift, we define a cost functional to be minimized

$$\mathcal{J} = - \int_{t_0}^{t_1} \int_{\Omega} \tilde{f}_y^2(\phi(t), x, t) dx dt + C_w \int_{t_0}^{t_1} \int_{\mathcal{C}} \phi^2(t) dx dt, \quad (4.4)$$

where  $t_0$  and  $t_1$  are the start and end times of the optimization horizon and  $\Omega$  is the surface of the body (see Figure 4.1).  $\phi$  is the control input, in this case  $\phi(t) = U_j(t)$ . Again,  $\tilde{f}_y$  is the  $y$  component of forces on the plate calculated in the immersed boundary projection method. The first term is the total squared lift over the optimization horizon. The second term penalizes the actuator amplitude in order to keep  $C_\mu$  to a value commensurate with the open-loop control discussed previously. The control weight,  $C_w$ , is determined by trial and error and is held fixed throughout the optimization.

Consider the linearized perturbation  $\mathcal{J}'$  to the cost functional  $\mathcal{J}$  resulting from an arbitrary

perturbation  $\phi'$  to the control  $\phi$ . The quantity  $\mathcal{J}'$  may be defined by a limiting process as the Fréchet differential (Vainberg, 1964) of the cost functional  $\mathcal{J}$  with respect to  $\phi$  such that

$$\mathcal{J}' \triangleq \lim_{\epsilon \rightarrow 0} \frac{\mathcal{J}(\phi + \epsilon\phi') - \mathcal{J}(\phi)}{\epsilon} \triangleq \int_{t_0}^{t_1} \int_{\Omega} \frac{\mathcal{D}\mathcal{J}(\phi)}{\mathcal{D}\phi} \phi' dx dt. \quad (4.5)$$

In the case of our cost functional as in (4.4), this sensitivity of the cost functional  $\mathcal{J}'$  resulting from a control perturbation  $\phi'$  may be written as

$$\mathcal{J}' = - \int_{t_0}^{t_1} \int_{\Omega} 2(\tilde{f}_y(\phi(t), x, t)) \tilde{f}'_y dx dt + C_w \int_{t_0}^{t_1} \int_{\mathcal{C}} 2\phi(t)\phi' dx dt, \quad (4.6)$$

where  $\tilde{f}'_y$  is the Fréchet differential of  $\phi$  as defined in the following subsection.

#### 4.2.2 Adjoint-based Optimization: Formulation

Now consider the linearized perturbation  $\mathbf{q}'$  to the flow  $\mathbf{q}$  resulting from a perturbation  $\phi'$  to the control  $\phi$ . The quantity  $\mathbf{q}'$  may be defined by the limiting process of a Fréchet differential such that

$$\mathbf{q}' \triangleq \lim_{\epsilon \rightarrow 0} \frac{\mathbf{q}(\phi + \epsilon\phi') - \mathbf{q}(\phi)}{\epsilon}. \quad (4.7)$$

We take  $\mathbf{q}'$  to be the still unknown perturbation to a solution  $\mathbf{q}$  of the flow equation due to a control perturbation  $\phi'$ . Mathematically, this means that

$$\mathcal{N}(\mathbf{q} + \mathbf{q}') = \mathbf{F}(\phi + \phi') \quad (4.8)$$

where the notation for the term on the right-hand side indicates that the vector  $\mathbf{F}$  multiplies the scalar  $\phi + \phi'$ . Linearizing (4.8) in  $\mathbf{q}'$ , or equivalently taking the differential of the governing equation (4.2), yields

$$\mathcal{N}'(\mathbf{q})\mathbf{q}' = \mathbf{F}\phi'. \quad (4.9)$$

The operator  $\mathcal{N}'(\mathbf{q})\mathbf{q}'$  is linear in  $\mathbf{q}'$ , though  $\mathcal{N}'(\mathbf{q})$  is itself a nonlinear function of  $\mathbf{q}$ . Using the same Inner product defined as (A.4) in Appendix A,

$$\langle c, d \rangle = \int_{t_0}^{t_1} \int \gamma_c \cdot (C^T C)^{-1} \cdot \gamma_d dx dt + \int_{t_0}^{t_1} \int \tilde{f}_c \cdot \tilde{f}_d dx dt, \quad (4.10)$$

$$c = \begin{pmatrix} \gamma_c \\ \tilde{f}_c \end{pmatrix}, \quad d = \begin{pmatrix} \gamma_d \\ \tilde{f}_d \end{pmatrix}, \quad (4.11)$$

consider the following identity

$$\langle \mathcal{N}'(\mathbf{q})\mathbf{q}', \mathbf{q}^* \rangle = \langle \mathbf{q}', \mathcal{N}^*(\mathbf{q})\mathbf{q}^* \rangle + b, \quad (4.12)$$

where the operation  $\mathcal{N}^*(\mathbf{q})\mathbf{q}^*$  is a linear operation on the adjoint field  $\mathbf{q}^*$  and the operator  $\mathcal{N}^*(\mathbf{q})$  is itself a function of the solution  $\mathbf{q}$  of the Navier-Stokes problem. The boundary term  $b$  is eliminated by choosing appropriate boundary and initial conditions for the adjoint problem. Causality eliminates the time boundary term at the initial time  $t = t_0$ : there can be no perturbation to the flow (i.e.  $\mathbf{q}' = 0$ ) due to the control before the control is applied. The condition at the end time  $t = t_1$  is eliminated by simply starting with  $\mathbf{q}^* = 0$  at  $t = t_1$  and solving the adjoint system backward in time. Integration by parts may be used to move all differential operations from  $\mathbf{q}'$  on the left-hand side of (4.12) to  $\mathbf{q}^*$  on the right-hand side, resulting in the same adjoint operator derived in Appendix A:

$$\mathcal{N}^*(\mathbf{q}) = \begin{pmatrix} -\frac{d\gamma^*}{dt} + C^T E^T \tilde{f}^* + \beta C^T C \gamma^* - (C^T C) n_L (\gamma_0)^T q_a \\ EC \tilde{f}^* \end{pmatrix}. \quad (4.13)$$

We can now choose a source term  $\mathbf{F}^*$  for our adjoint system

$$\mathcal{N}^*(\mathbf{q})\mathbf{q}^* = \mathbf{F}^*, \quad (4.14)$$

so that the adjoint solution provides the gradient  $\mathcal{D}\mathcal{J}/\mathcal{D}\phi$ . We start by substituting (4.9) and (4.23) into (4.12) with  $b = 0$ , which becomes,

$$\langle \mathbf{F}\phi', \mathbf{q}^* \rangle = \langle \mathbf{q}', \mathbf{F}^* \rangle. \quad (4.15)$$

Comparing (4.15) with (4.6) and (4.5), we would like to obtain

$$\langle \mathbf{q}', \mathbf{F}^* \rangle = \int_{t_0}^{t_1} \int_{\Omega} 2(\tilde{f}_y(\phi(t), x, t))\tilde{f}'_y dx dt, \quad (4.16)$$

so that

$$\langle \mathbf{F}\phi', \mathbf{q}^* \rangle = \int_{t_0}^{t_1} \int_{\Omega} \frac{\mathcal{D}\mathcal{J}(\phi)}{\mathcal{D}\phi} \phi' dx dt + C_w \int_{t_0}^{t_1} \int_{\Omega_0} 2\phi(t)\phi' dx dt. \quad (4.17)$$

The adjoint source term  $\mathbf{F}^*$  that gives (4.16) is

$$\mathbf{F}^*_{\gamma} = 0, \quad \mathbf{F}^*_{\tilde{f}_x} = 0, \quad \mathbf{F}^*_{\tilde{f}_y} = 2(\tilde{f}_y\phi(t), x, t), \quad (4.18)$$

and (4.6) and (4.5) becomes,

$$\mathcal{J}' \triangleq \int_{t_0}^{t_1} \int_{\Omega} \frac{\mathcal{D}\mathcal{J}(\phi)}{\mathcal{D}\phi} \phi' dx dt = \int_{t_0}^{t_1} \int_{\Omega_0} (2C_w\phi(t) + F_{\tilde{f}} \cdot \tilde{f}^*)\phi' dx dt. \quad (4.19)$$

Then, by (4.17) the gradient becomes

$$g(\phi) = \frac{\mathcal{D}\mathcal{J}(\phi)}{\mathcal{D}\phi} = 2C_w\phi(t) + F_{\tilde{f}} \cdot \tilde{f}^*. \quad (4.20)$$

### 4.2.3 Adjoint-based Optimization: Numerical Implementation

At each iteration of the optimization, we modify the controls according to

$$\phi^{k+1}(t) = \phi^k(t) + rg(\phi^k)(t), \quad (4.21)$$

where  $g(\phi)$  is the gradient of the cost function with respect to the controls, and  $r$  is the generalized distance determined iteratively (using Brent's line minimization) to minimize the cost function.  $g(\phi)$  is found by solving

$$g(\phi) = F_{\tilde{f}} \cdot \tilde{f}^* + 2C_w \phi, \quad (4.22)$$

where  $\tilde{f}^*$  are the force unknowns in the linearized adjoint equations (Ahuja & Rowley, 2008)

$$\mathcal{N}^*(\mathbf{q}) \mathbf{q}^* = \mathbf{F}^*. \quad (4.23)$$

Here  $\mathbf{q}^*$  are the adjoint variables (discrete circulations and forces) and  $\mathbf{F}^*$  is given by

$$\mathbf{F}^* = [F_\gamma^* \quad F_{\tilde{f}}^{*\top}]^\top = [0 \quad 2\tilde{f}_y]^\top. \quad (4.24)$$

The adjoint operator requires the full flow field from the (forward) Navier-Stokes simulation (2.1-2.3) at every time step. However, in order to save memory, we saved the flow solution only every few time steps and used a linear interpolation in time. Several test cases were done with a different number of time steps skipped, including a case where the solution was saved at every time step, and no significant differences were noted between them.

All optimizations used zero control ( $\phi = 0$ ) for the first iteration ( $k = 1$ ) on each optimization horizon. At each iteration, we required roughly ten full Navier-Stokes simulations to perform the line minimization (to find  $r$ ).

Optimization was done over a horizon  $T = [t_0, t_1]$ , where the horizon,  $T$ , is long enough to overcome transient effects, but limited by the computational effort to perform all the required iterations and to tune the control weight. We found for this problem that after about two periods the controls converged to an approximately periodic signal with each period corresponding to a vortex shedding cycle. A horizon of 6 periods gave the results presented below, and tests showed that the results were not very sensitive as the horizon was varied from about 5 to 8 periods. Once the iteration of the optimization converges, the control near the end of each optimization horizon

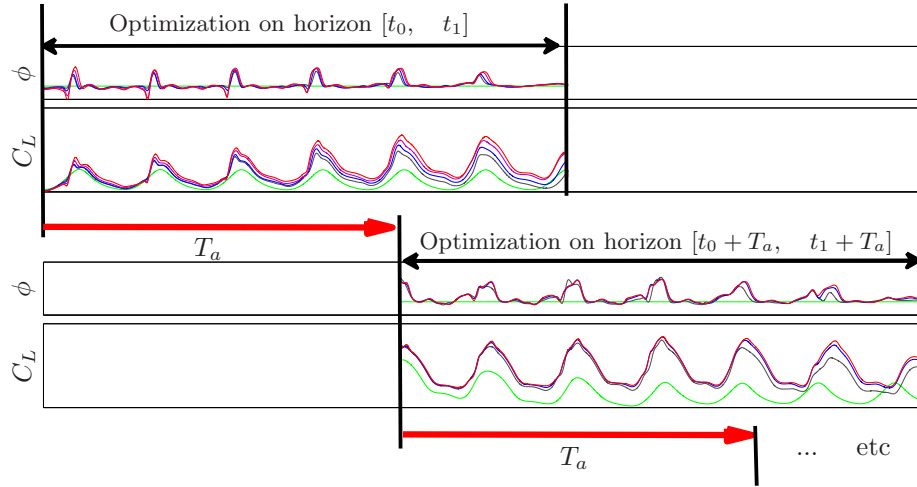


Figure 4.2: Schematic of receding-horizon predictive control. First the optimization of controls are performed on horizon  $[t_0, t_1]$ . Each iteration of optimization gives the update on control. Once the convergence of the control on the optimization is achieved, the flow is ‘advanced’ some portion  $T_a$  of the period  $T$ , and controls near the end of the optimization horizon are discarded and the optimization is begun anew on horizon  $[t_0 + T_a, t_1 + T_a]$ .

(transient of adjoint simulation) is discarded and the optimization is begun anew. This process is depicted in Figure 4.2.

#### 4.2.4 Adjoint-based Optimization: Results

Optimization results in a periodic control waveform after a couple of transient periods. As shown in Figure 4.5, this periodic optimal waveform is not sinusoidal, but rather composed of two distinct pulses per shedding cycle. The larger, later pulse is roughly in phase with the maximum lift. This result will be further discussed in Sect. 4.4 after feedback is designed to achieve the highest-lift, phase-locked shedding cycle with a given optimal or sinusoidal control waveform. Different values of control weight,  $C_w$ , result in a periodic control waveform with similar features, but with different average control input, thus different values of  $C_\mu$ . For example,  $C_w = 0.3$  gives the results shown in Figure 4.5 where  $C_\mu$  is about two times lower than that used for the sinusoidal forcing, but comparable lift is achieved. It should be noted that, although we cannot be assured that this is a global optimal, we observed similar results with different values of control weight and different initial controls (zero, constant, or sinusoid).

### 4.3 Feedback

Optimization provides a periodic control waveform after a couple of transient periods. While it is straightforward to extract a single period of the optimal waveform, the performance can be significantly degraded if this is applied to the plate in open loop as shown in Figure 4.4. Depending on the precise state of the flow upon initiation of forcing, the flow fails to lock onto the optimal waveform or locks on with a different phase than the optimal controller. Moreover, initial transients and subharmonic resonances further degrade the performance. Thus in this section, we design a practically implementable feedback algorithm to achieve phase lock between the lift and the optimal control waveform deduced from the adjoint-based algorithm in the previous section.

For example, we may decompose the optimal control waveform as

$$\begin{aligned}\phi_{\text{optimal}}(t) &= A_0 + \sum_k^{N_k} [A_k \cos(k\omega t) + B_k \sin(k\omega t)] \\ &= A_0 + \sum_k^{N_k} [A_k \cos(k\theta(t)) + B_k \sin(k\theta(t))],\end{aligned}\tag{4.25}$$

where  $N_k$  is the number of harmonics retained and  $\omega$  is the fundamental frequency of the optimal waveform. We used  $N_k = 10$  which provided a reasonable representation (less than 5% deviation from the original optimized waveform).

In order to implement this optimal waveform with a consistent phase difference between each of the harmonics, instantaneous phase information of the lift signal is required. The frequency of the lift signal is tracked with an Extended Kalman Filter (EKF) to estimate the phase,  $\theta(t)$  for use in Eq. 4.25. To improve the EKF phase estimate, a narrowband filter is first used on the lift cycle to obtain a more nearly sinusoidal signal as input to the EKF. The EKF frequency estimate is then used to tune the filter to avoid introducing phase lag. The overall feedback algorithm is illustrated in Figure 4.3.

First, we perform a narrowband filtering of the lift according to

$$\omega_i = 2\pi/T_i, \quad (4.26)$$

$$a_1(t) = \frac{2}{T_i} \int_{t-T_i}^t C_L(t') \cos(\omega_i t') dt', \quad (4.27)$$

$$b_1(t) = \frac{2}{T_i} \int_{t-T_i}^t C_L(t') \sin(\omega_i t') dt', \quad (4.28)$$

$$y(t) = a_1(t) \cos(\omega_i t) + b_1(t) \sin(\omega_i t). \quad (4.29)$$

The filtered lift,  $y(t)$  retains the dominant frequency, initially estimated as  $\omega_i$ , and filters out higher harmonics. Next,  $y(t)$  is modeled as a pure sinusoid

$$\hat{y}(t) = \hat{a} \sin(\hat{\theta}(t)), \quad (4.30)$$

$$\hat{\theta}(t) = \hat{\omega}_o t, \quad (4.31)$$

where  $\hat{\theta}$  is estimated with the EKF; values for noise processes are chosen in the EKF so that the algorithm converges in a few cycles. Our implementation of the EKF follows closely the description in Tadmor (2004) and Pastoor *et al.* (2008) and is described in Appendix B.

When computing  $y(t)$ , the initial estimate for  $\omega_i$  is updated with the estimate  $\hat{\omega}_o$ , the frequency estimated by the EKF, and we write

$$\phi_{\text{optimal}}(t) = A_0 + \sum_k^{N_k} [A_k \cos(k(\hat{\theta}(t) - \theta_{\text{desired}}(t))) + B_k \sin(k(\hat{\theta}(t) - \theta_{\text{desired}}(t)))], \quad (4.32)$$

where  $\theta_{\text{desired}}$  is an additional (specified) phase shift relative to the lift signal.

Also, note that this feedback controller can be simply implemented for the sinusoidal waveform by setting  $N_k = 1$ ,  $A_1 = 0$ , and  $A_0 = B_1 = 0.5$  for  $C_\mu = 0.01$ .

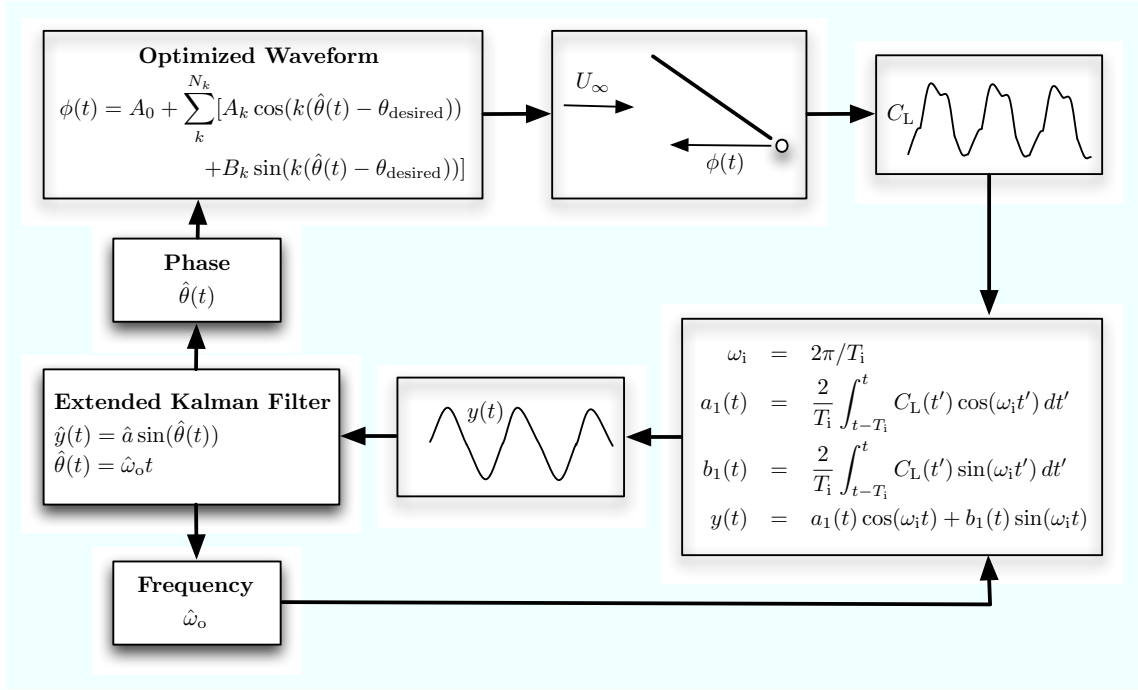


Figure 4.3: Schematic of feedback.

## 4.4 Results of Optimized Feedback Control

As shown in Figure 4.4, feedback control of the optimized waveform is able to reproduce the high-lift limit cycle that the optimization achieved, but starting from an arbitrary phase of the baseline limit cycle. The feedback system converges to something very close to the previous solution after 4 to 5 periods, and is indistinguishable after about 10 cycles.

Figure 4.5 compares a few periods of the optimal control signal ( $U_j(t)$ ) and the resulting lift coefficient. The results are plotted against the closed-loop controlled case with a sinusoidal waveform where this compensator phase locked the flow at a limit cycle associated with the highest average lift at a given  $C_\mu = 0.01$ . The optimized control is not sinusoidal, but rather composed of two distinct pulses per shedding cycle. The larger, later pulse is roughly in phase with the maximum lift. In Figure 4.6, we overlay the vorticity contours at the minimum and maximum lift for the baseline and sinusoidal forcing and compare vorticity contours for the optimized control to the sinusoidal forcing in Figure 4.7. Maximum lift is found when the LEV is brought down to the suction side of the plate

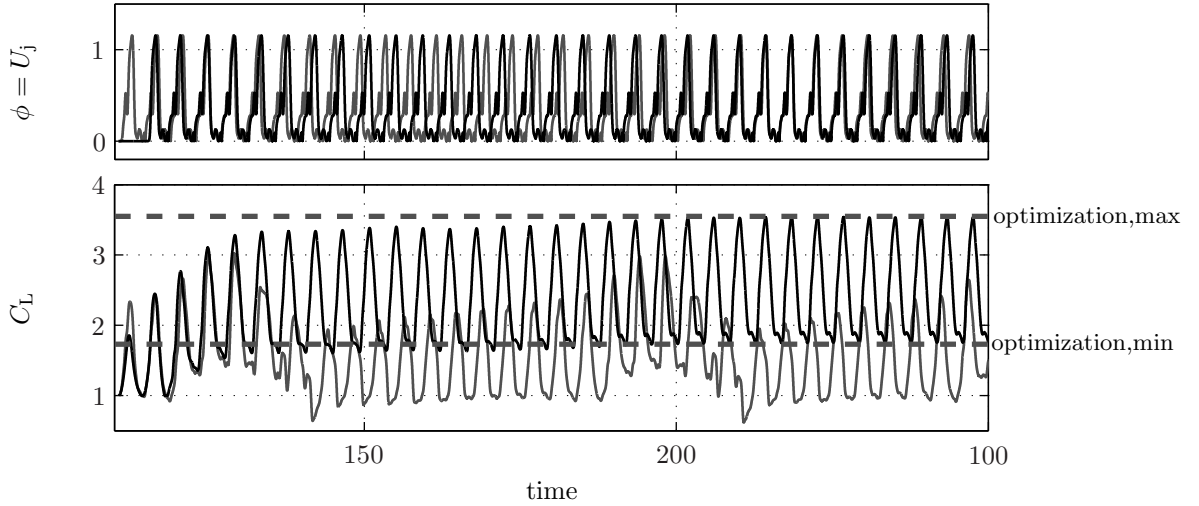


Figure 4.4: Comparison between open-loop control case (grey) and the feedback control case (black) with optimized waveform ( $N_k = 10$ ) at  $\alpha = 40^\circ$ .

as it grows in strength. The lift decreases as the new vortex structure of the opposite sign is formed at the trailing edge. Minimum lift occurs as this TEV pushes up the LEV sitting on the plate, and finally halts its growth causing it to pinch-off and shed into the wake.

For both sinusoidal and optimized control, the primary effect of actuation is to create extra vorticity which is fed into the TEV as the vortices are alternately being formed and shed. After the first local minimum lift, as the new LEV is being formed, both waveforms start to feed extra circulation at the trailing edge, leading to more definite pinch off of the LEV at the following global minimum lift. The magnitude of actuation increases as the growing LEV (lift is increasing) is pulled down by the growing TEV, and finally reaches its peak near the maximum lift. The corresponding TEV is strengthened and caused to shed from the trailing edge, thereby allowing the LEV to grow larger. This results in more vertically elongated TEV that induces stronger downwash near the trailing edge, causing the LEV to sit closer to the plate, leading to higher lift compared to the baseline.

The flow field for the optimized control does not look very different from the sinusoidal forcing. However, in the optimized control, the short pause between the two pulses slows down the growth of the TEV momentarily. This separates the TEV into two structures connected by a thin vortex

sheet. The effect of the dip between the two pulses will be investigated further with the feedback control later in this section.

The most distinct feature of the optimized control compared to sinusoidal forcing is the gradual increase in  $\phi$  during the most of the cycle followed by a more rapid decrease after its peak. A gradual addition of circulation alters the formation of the TEV such that it interferes minimally with the natural formation of LEV and only acts as a downwash to push the LEV closer to the plate. Immediately after the maximum lift, the forcing is turned off sharply. This phase of the shedding cycle is where the optimized control achieves similar magnitude of lift with minimal control input compared to the sinusoidal control. Since the shedding of the LEV is probably unavoidable in two-dimensional flow (no spanwise flux of vorticity in  $z$ -direction) after the maximum lift has been achieved, letting it shed naturally may be the most energy efficient. For the periods shown in Figure 4.5, optimized control resulted in an average lift and drag coefficients of  $\overline{C_{L,ave}} = 2.50$  and  $\overline{C_D} = 2.06$ , corresponding to the average lift-to-drag ratio of  $\overline{C_L/C_D}=1.20$  with  $C_\mu = 0.005$  and  $C'_\mu = 0.010$ . With sinusoidal waveform, the feedback achieved  $\overline{C_L} = 2.25$  and  $\overline{C_D} = 1.83$  ( $\overline{C_L/C_D} = 1.20$ ) with  $C_\mu = C'_\mu = 0.010$ . Compared to baseline flow ( $\overline{C_L} = 1.35$ ,  $\overline{C_D} = 1.20$ , and  $\overline{C_L/C_D} = 1.104$ ), optimized control resulted in more than 85% increase in average lift. Figure 4.8 compares the average lift values from the optimized control to the results from the feedback controlled cases with sinusoidal waveform where the compensator phase locked the flow at a limit cycle with the highest average lift at different values of  $C_\mu$ . At  $C_\mu$  below 0.0065, the lift performance of the sinusoidal control decreases sharply and approaches close to the average lift of the natural flow at  $C_\mu = 0.005$ . However, optimized control is able to produce high lift even at low  $C_\mu = 0.0025$ .

The feedback controller now allows us to phase-lock an essentially arbitrary waveform, and we can utilize this fact to investigate which features of the optimized waveform are critical to high lift. In Figure 4.9, we demonstrate the effect of smoothing the optimal waveform by retaining fewer harmonics in the Fourier expansion. Using  $N_k = 4$ , for example, smoothes out the dip between the two highest maxima, but has little impact on the lift achieved. This indicates that, during this phase of the shedding cycle, the sensitivity of the first term (lift-maximizing term) in Eq. 4.4 to the change

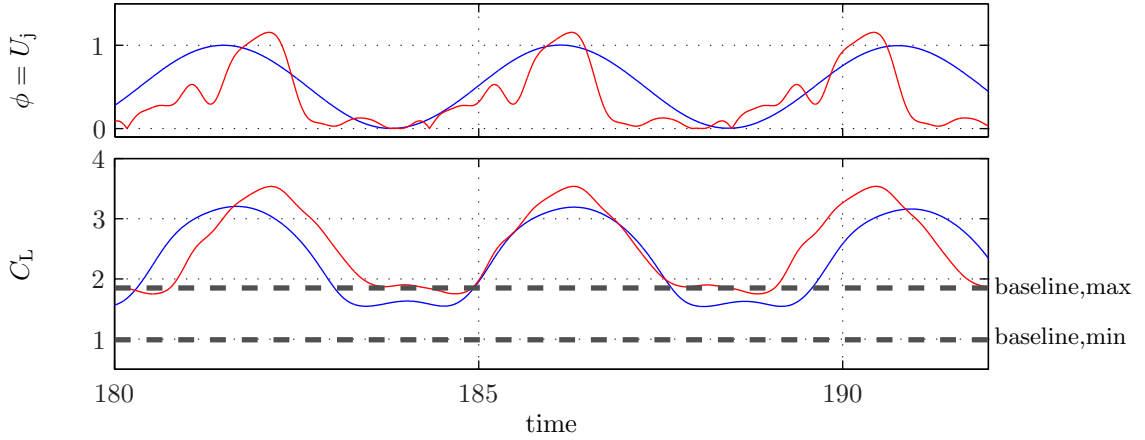


Figure 4.5: Comparison of optimized control (—) with closed-loop sinusoidal forcing(—) at  $\alpha = 40^\circ$ . Maximum and minimum lift of baseline (- - -) case is shown as a reference.

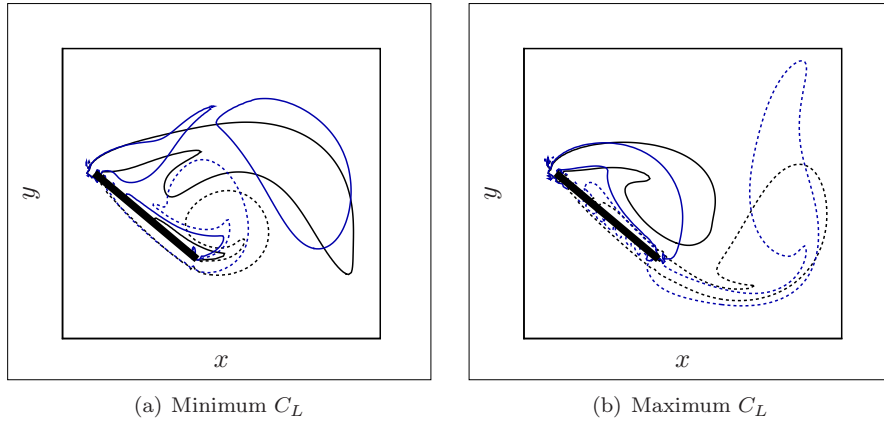


Figure 4.6: Vorticity contour at the (a) minimum and (b) maximum lift for baseline (black) and sinusoidal actuation (blue). Dashed and solid lines represent counterclockwise and clockwise vorticity.

in  $\phi$  is small compared to the second term (control-penalizing term). The short pause between the two pulses may be just an energy-saving feature of the optimal control.

Figure 4.10 investigates the sensitivity of the lift performance of the phase-locked limit cycles to the changes in the phase shift,  $\theta_{\text{desired}}$  with the optimal control ( $N_k = 10$ ). Feedback is able to phase lock the flow at any desired phase shift after  $3 \sim 5$  periods over a wide range of  $\theta_{\text{desired}}$ . Due to pulse-like feature of the optimal waveform, the lift is quite sensitive to changes in the phase shift, with the average lift dropping below the maximum lift of the baseline with  $20^\circ$  phase changes. Because the optimized waveform rapidly decreases immediately after its peak, forcing with the peak

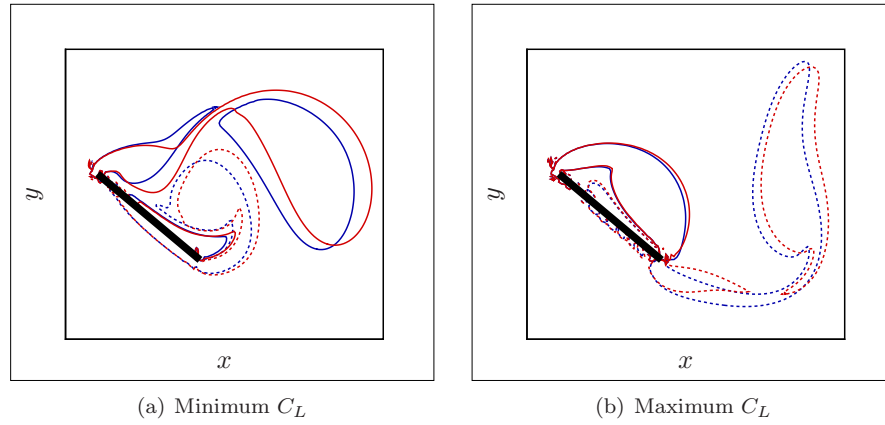


Figure 4.7: Vorticity contour at the (a) minimum and (b) maximum lift for sinusoidal actuation (blue) and optimized actuation (red). Dashed and solid lines represent counterclockwise and clockwise vorticity.

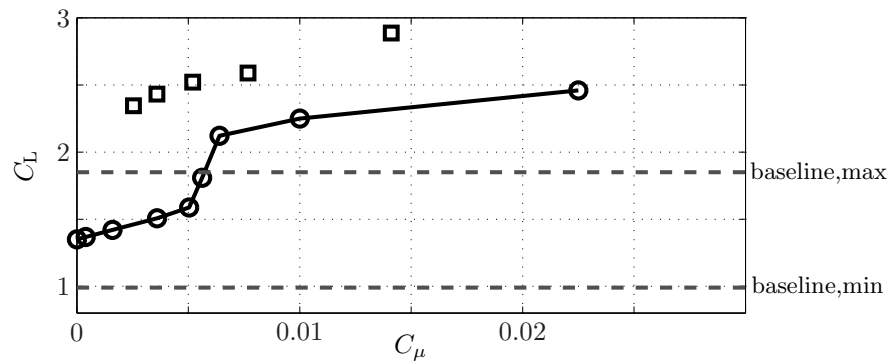


Figure 4.8: Average lift of optimized control ( $\square$ ) and closed-loop sinusoidal forcing ( $\circ$ ) at different values of  $C_\mu$  at  $\alpha = 40^\circ$ . For the optimized control, different values of the control weight,  $C_w$  is used in (4.4), resulting in corresponding values of  $C_\mu$  as shown.

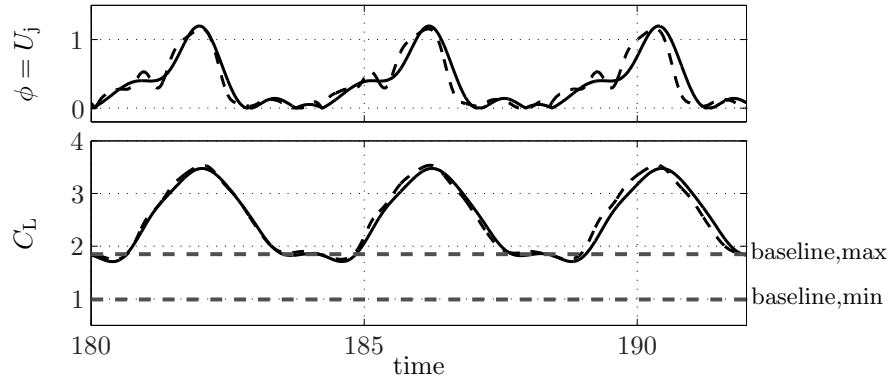


Figure 4.9: Comparison between feedback control cases with optimized waveform at  $\alpha = 40^\circ$ :  $N_k = 10$  (dashed) and  $N_k = 4$  (solid).

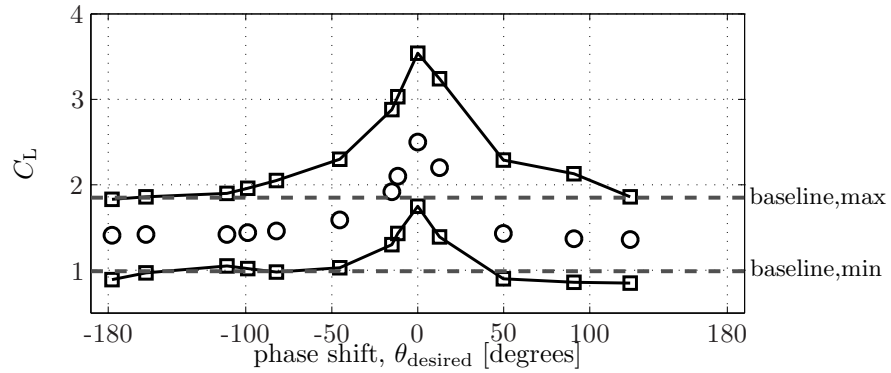


Figure 4.10: Maximum and minimum lift ( $\square$ ) and average lift ( $\circ$ ) of phase-locked limit cycles at different phase shift with optimized waveform ( $N_k = 10$ ) at  $\alpha = 40^\circ$ . Maximum and minimum lift of baseline (---) case is shown as a reference.

prior to the maximum lift (at negative phase shift) impacts the lift significantly. Also, positive phase shift penalizes the lift performance since the magnitude of  $g(\phi)$  (sensitivity of the cost functional, Eq. 4.4 to changes in control,  $\phi$ ) is small during the lift-decreasing phase; thus, control is not as effective. As the phase shift approaches  $\pm 180^\circ$  (out of phase), the forced flow results in the average lift similar to that of an unforced flow.

## 4.5 Sinusoidal Pulse

The optimization provided a pulsatile waveform roughly in phase with the maximum lift. The optimized waveform features a slow increase prior to its maximum and sharply drops to zero control

afterwards. Control is mostly important as the new vortex is formed as the lift is increasing, and when the maximum lift is achieved, control could be counterproductive.

Motivated by the pulsatile waveform the optimization provided, we investigate the lift response to pulses of different duty cycles. We define the duty cycle as a percentage of the width of a sinusoidal waveform to the period of actuation. Thus, a duty cycle of 100% gives a continuous sinusoidal used in the previous sections and a duty cycle of 50% results in a sinusoidal waveform with its width that is half the actuation period. Figure 4.11 investigates the effect of this sinusoidal pulse by decreasing its duty cycle while keeping its maximum or its average the same. With each waveform of different average  $U_j$  or maximum  $U_j$ , the feedback was used to phase lock the flow at a limit cycle with a different phase shift, and the highest average lift was observed when the forcing was in phase with the lift for all cases considered, which is shown in the figure. By decreasing the duty cycle of a sinusoidal pulse, we were able to achieve high lift with much smaller  $C_\mu$  than continuous sinusoidal forcing (DC=100%). It is interesting to note that a duty cycle of 62.5% resulted in higher lift than 100% even though the average  $U_j$  was decreased by almost 40%. This might be due to higher magnitude of  $dU_j/dt$  near its maximum resulting in more effective pinch off of the LEV letting subsequent LEV to form. We find that the sinusoidal pulse with its duty cycle as small as 25% achieves similar average lift enhancement as a continuous sinusoid when the forcing is in phase with the lift. However, smaller duty cycles were not able to sustain the lift enhancement and result in a similar average lift of the baseline flow.

By keeping average  $U_j$  constant, we can decrease the duty cycle further without sacrificing the lift performance.

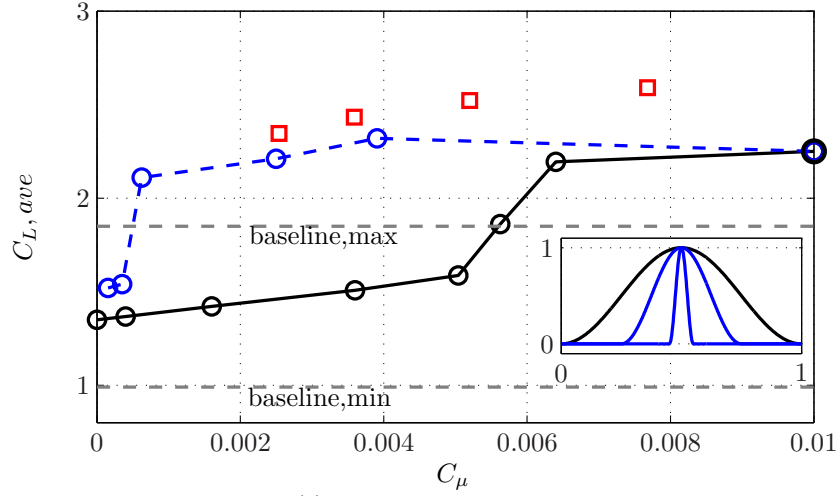
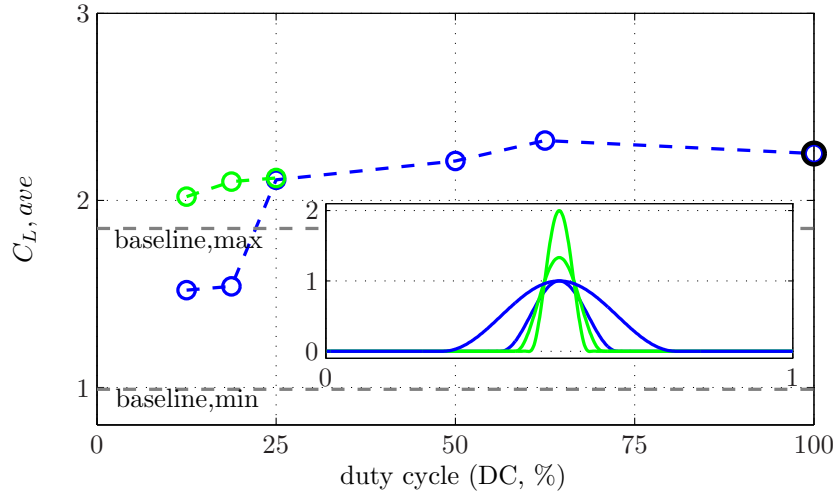
(a) Constant maximum  $U_j$ (b) Constant average  $U_j$ 

Figure 4.11: Sinusoidal pulses of different widths with either a constant maximum (blue) or average (green)  $U_j$ . Duty cycle is defined here as a percentage of the width of a sinusoidal waveform to the period of actuation. Thus, a duty cycle of 100% gives a continuous sinusoidal waveform (black). The feedback was used to phase lock the flow near zero phase shift. This phase shift results in the highest average lift for all cases considered. For the optimized control (red), different values of the control weight were used in each optimization to result in different values of  $C_\mu$  as shown.

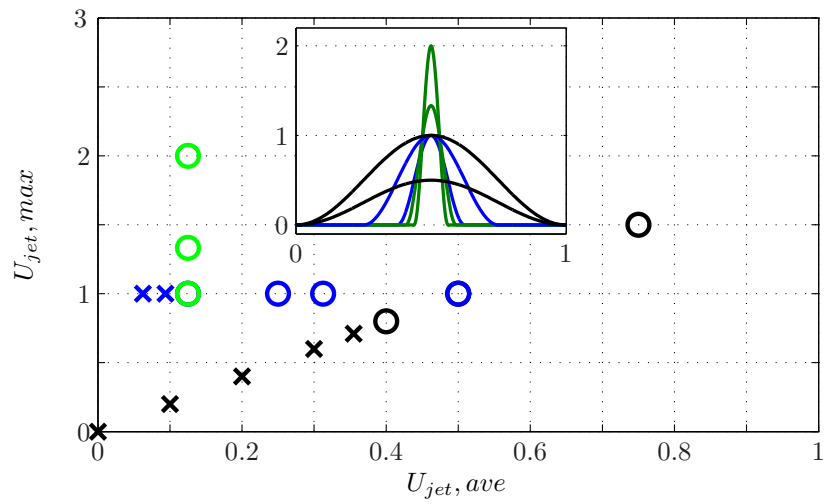


Figure 4.12: Sinusoidal pulse with constant maximum (blue) and average (green)  $U_j$ . Circles and x-marks indicate higher and lower average  $C_L$ , respectively, than the maximum lift achieved by baseline shedding cycle.

## Chapter 5

# Control at $Re = 3000$

At  $Re=300$ , the optimal waveform was not a continuous sinusoidal, but rather pulsatile. In fact, we showed that a sinusoidal pulse whose width is as small as 25% of the actuation period (duty cycle of 25%) resulted in a similar lift enhancement as a continuous sinusoidal (duty cycle of 100%), when the control was nearly in phase with the lift in both cases. In this chapter, we investigate the nature of this optimal forcing waveform at a higher  $Re$  of 3000. Particularly, we consider the lift response to the sinusoidal pulses with different widths compared to the actuation period (duty cycle).

Greenblatt *et al.* (2008) performed a series of experiments on a flat-plate airfoil and an Eppler E338 airfoil at Reynolds numbers ( $3000 \leq Re \leq 50,000$ ), in which dielectric barrier discharge (DBD) plasma actuators were employed at the leading edges to effect flow control. The DBD actuator was calibrated in a quiescent environment ( $U_\infty = 0$ ) and generated wall-parallel flow at the leading edges with relatively small magnitude of wall-normal velocities. Using this model, Greenblatt *et al.* (2008) found the optimum reduced frequencies  $F^+$  for generating poststall lift were approximately between 0.4 and 1.0, which resulted in an increase in maximum lift coefficient of 0.4 to 0.8 at high post-stall angles of attack.

In this chapter, we consider the same geometry and Reynolds number, a flat plate with a thickness-to-chord ratio of 4% at  $Re = 3000$ , as Greenblatt *et al.* (2008), in an attempt to better understand the effects of control on the dynamics of vortex shedding, and to apply the tools and knowledge gained at the lower Reynolds number of 300 in the last two chapters. Greenblatt *et al.* (2008) focused on the long-time average lift and explained the effect of control using representative

snapshots of smoke visualization. In this chapter, we consider more detailed time-dependent aspects of the lift and corresponding flow fields, particularly the flow structures at the minimum and maximum lift, and the phase of pulses relative to the lift. This allows us to more precisely compare different actuated flow fields and distinguish the differences responsible for higher or lower instantaneous lift, along with identifying different vortex evolutions. Finally, we show that for certain frequencies and actuator waveforms, there occur stable limit cycles in which the flow is phase locked to the actuation.

For a range of angles of attack, Greenblatt *et al.* (2008) observed the greatest lift enhancement over a range of frequencies  $0.4 < F^+ < 0.6$ . Control resulted in a 50% increase in lift at angles of attack greater than about 20 degrees, with results at  $\alpha \leq 10^\circ$  showing at most equivalent lift to the baseline case.

In our simulations, we therefore consider two representative angles of attack,  $\alpha = 10^\circ$  and  $20^\circ$ .

## 5.1 Numerical Method

Simulations of flow over a two-dimensional flat plate at  $Re = 3000$  are performed with the immersed boundary projection method combined with a multi-domain technique (Taira & Colonius, 2007; Colonius & Taira, 2008) described in Chapter 2. In what follows, all velocities and length scales are nondimensionalized by the freestream velocity and the chord,  $U_\infty$  and  $c$ , respectively. The finest grid, encompassing the body, is comprised of a rectangular domain extending to  $[-0.5, 2.5] \times [-0.9, 0.6]$  in the streamwise ( $x$ ) and vertical ( $y$ ) directions with a uniform grid spacing of 0.005 units ( $\Delta x = \Delta y = 0.005$ ). The constant time step was 0.0005. The coarsest grid extended to  $[-8, 32] \times [-12, 12]$ . The coarsest grid extended to  $[-2, 10] \times [-3.6, 2.4]$ . Selected cases were run on finer grids ( $\Delta x = 0.00375$ ) and with larger extents (twice the coarsest grid) to demonstrate convergence and independence to far-field boundary conditions.

In the previous chapters at  $Re = 300$ , we modeled the actuation by specifying the jet velocity at the actuation point as part of the boundary conditions on the body, and the force needed to satisfy

that specified velocity was calculated in the simulation. In order to mimic the plasma actuator used in the experiments, we introduce a specified body force expressed as

$$\mathbf{f}_{act} = \hat{\mathbf{f}}_{act} \delta(x - x_0) \phi_{control}(t) \quad (5.1)$$

to the right-hand side of the momentum equation, equation 2.1. Here  $\hat{\mathbf{f}}_{act}$  prescribes the strength and the direction of the actuator and  $\phi_{control}(t)$  is a control waveform described below. The location of the actuator is specified with  $(x_0, y_0)$ . In the computation, the Dirac delta function,  $\delta()$ , is replaced by a discrete delta function,  $\bar{\delta}()$  proposed by Roma *et al.* (1999) that regularizes the singularity across 3 cells in both the  $x$ - and  $y$ -directions in the following manner:

$$\bar{\delta} = \begin{cases} \frac{1}{6\Delta x} \left[ 5 - 3\frac{|x|}{\Delta x} - \sqrt{-3\left(1 - \frac{|x|}{\Delta x}\right)^2 + 1} \right] & \text{for } 0.5\Delta x \leq |x| \leq 1.5\Delta x, \\ \frac{1}{3\Delta x} \left[ 1 + \sqrt{-3\left(\frac{x}{\Delta x}\right)^2 + 1} \right] & \text{for } |x| \leq 0.5\Delta x, \\ 0 & \text{otherwise.} \end{cases} \quad (5.2)$$

The function is shown here for the  $x$ -direction with a mesh width of  $\Delta x$ . This delta function is also used in the immersed boundary projection method to represent the immersed boundary.

We place the actuation at the leading edge directed parallel to the plate towards the trailing edge as illustrated in Figure 5.1. The actuation is positioned  $3\Delta x = 0.015$  from the leading edge in the normal direction to the plate, since the peak of the wall-parallel velocity profile produced by DBD plasma actuation in Greenblatt *et al.* (2008) was observed at  $0.015c$ .

In order to add the right magnitude of  $\mathbf{f}_{act}$  in order to generate the steady peak jet velocity comparable to the freestream velocity, we first simulate the sinusoidal blowing at different frequencies with prescribed  $\mathbf{f}_{act}$  in an initially quiescent free space. Once steady state is achieved, the velocity at the center of the forcing is selected as the characteristic velocity  $U_j$ . For example,  $|\mathbf{f}_{act}| = 0.1$  corresponds to  $\overline{U}_j = U_{j,max} = 0.5$  and  $C_\mu = 0.01$ .

In the experiments, Greenblatt *et al.* (2008) modulated a high frequency (5kHz) signal with a rectangular waveform at  $F^+$ , thus a duty cycle of 100% results in a steady forcing with just a

high frequency component. However, the goal of this chapter is to investigate the lift response to different waveforms motivated by the nature of the optimal forcing found at  $Re = 300$ , i.e. pulses of different widths compared to a continuous sinusoid. Thus, we define a duty cycle as percentage of the width of a sinusoidal waveform to the period of actuation, so that a duty cycle of 100% refers to a continuous sinusoidal forcing. Even though the resulting representations of the waveforms are different at high duty cycles, at low duty cycles, the difference becomes less significant. At  $DC = 5\%$ , the resulting sinusoidal forcing could be a reasonable representation of a rectangular waveform used in the experiments.

Once  $|\mathbf{f}_{act}|$  is determined to generate a desired velocity at the center of the forcing,  $\phi_{control}(t)$  is a actuation waveform that varies from 0 to 1. We first decompose the sinusoidal-pulse waveform with a specified duty cycle as

$$\begin{aligned}\phi_{control}(t) &= A_0 + \sum_k^{N_k} [A_k \cos(k\omega t) + B_k \sin(k\omega t)] \\ &= A_0 + \sum_k^{N_k} [A_k \cos(k\theta(t)) + B_k \sin(k\theta(t))],\end{aligned}\tag{5.3}$$

where  $N_k$  is the number of harmonics retained and  $\omega$  is the fundamental frequency of the optimal waveform. We used  $N_k = 50$  which provided a reasonable representation (less than 5% deviation from the perfect sinusoidal pulse for all the duty cycles considered). Then, we march along  $\phi_{control}$  with  $\theta(t) = 2\pi/T_{control} * t$  where  $T_{control} = 1/F^+$  is the period of actuation.

Also, note that (5.3) becomes a continuous sinusoidal waveform (duty cycle,  $DC = 100\%$  in Figure 5.2) by setting  $N_k = 1$ ,  $A_1 = 0$ , and  $A_0 = B_1 = 0.5$ . Figure 5.2 shows an example of the sinusoidal pulses.

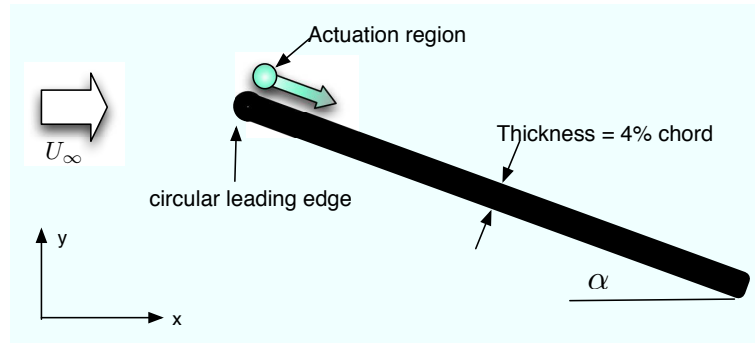


Figure 5.1: Schematic of flat plate of thickness-to-chord ratio of 4% and actuation at the leading edge.

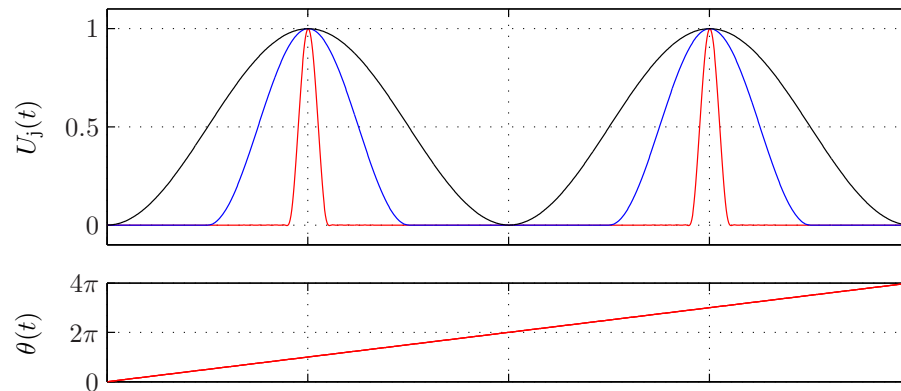


Figure 5.2: Sinusoidal pulse waveform,  $U_j(t)$  and phase,  $\theta(t)$  with duty cycle,  $DC = 5\%$  (red),  $50\%$  (blue),  $100\%$  (black).  $\theta(t) = 2\pi$  is a period of every pulse. Duty cycle is defined here as a percentage of the width of a sinusoidal waveform to the period of actuation. Thus, a duty cycle of  $100\%$  gives a continuous sinusoidal waveform (black).

## 5.2 Uncontrolled flow

Figure 5.3 shows computed lift coefficients over a range of  $\alpha$  and the experimental data of Greenblatt *et al.* (2008) and of Alam *et al.* (2010) (with  $Re = 5,000$  and  $10,000$ ). Even though the computations display a similar trend as the experiments, the magnitude of lift in the two-dimensional simulation is almost twice as high as that of the experiments. Later simulations of the same geometry and  $Re$  by Schneider *et al.* (2008) also overpredicted the lift by a similar magnitude as in our case at high angles of attack.

Of course, the experiments used finite-aspect-ratio models, (AR=3.0 for Greenblatt *et al.* (2008) and 2.7 for Alam *et al.* (2010)). Both experiments (Greenblatt *et al.*, 2008; Alam *et al.*, 2010) used endplates to try to enforce two-dimensional flow. It has been noted that accurate measurements of lift or drag with endplates and small aspect ratio models are difficult to obtain at low Reynolds numbers because of the interaction between the thick boundary layers on the endplates and the flow around the wing, which results in a three-dimensional flow along the span of the model (Mueller, 1999). Mueller (1999) investigated the effect of endplates on two-dimensional measurements by considering two different models (3-piece model and 2-piece model). With the 3-piece model, the middle section of the airfoil was free to move between two other sections of the same airfoil and the two other sections were fixed to the endplates in the wind tunnel. A small gap was present between the end models and the center piece, which was connected to the force balance, so that the center piece adjusts itself to where the flow is more two-dimensional and the force measurements were less effected by the corner flow at the endplates. This 3-piece model gave forces closer to 2-dimensional results, resulting in higher lift than the 2-piece model that was used in Greenblatt *et al.* (2008) and Alam *et al.* (2010). Mueller (1999) found that these end effects become more significant as Reynolds number was decreased, resulting in difference in lift by up to a factor of two at  $Re \approx 20,000$ .

Figure 5.4 shows the time history and power spectrum of the baseline flow at  $\alpha = 10^\circ$  and  $\alpha = 20^\circ$ . The lift histories are analyzed with a Fourier transform to detect any dominant shedding frequencies. Also, streaklines and vorticity of representative instances of the baseline flow in Figure 5.6 and

Figure 5.5 show examples of the shedding cycles at  $\alpha = 10^\circ$  and  $20^\circ$ , respectively. At  $\alpha = 10^\circ$ , the shedding occurs with a dominant shedding frequency (periodic) at  $F^+ = 0.65$ . Since the Strouhal number is defined with the projected chord length to the freestream and  $St$  and  $F^+$  are related by:

$$F^+ = fc/U_\infty, \quad St = fc \sin(\alpha)/U_\infty, \quad St = F^+ \sin(\alpha), \quad (5.4)$$

this corresponds to Strouhal number of  $St = F^+ \sin(\alpha) \approx 0.11$ .

However at  $\alpha = 20^\circ$ , there are several recognizable frequencies, one at  $F^+ = 0.2$  and another at  $F^+ = 0.4$ , which corresponds to  $St \approx 0.14$ . At  $Re = 300$ , we observed a very organized periodic vortex shedding at high angles of attack. However at  $Re = 3000$ , the separated shear layer becomes unstable and smaller vortices form as a result of this instability. The fluctuations in the lift due to the shear layer instability are intermittent, leading to a broadly smeared power spectrum with no dominant peak at  $\alpha = 20^\circ$ . The flow exhibits shear-layer instability at both the leading and trailing edges leading to chaotic lift cycles as shown in Figure 5.5. The flow field clearly shows separation from the leading edge and subsequent rollup of the shear layer into distinct vortices.

In the simulation, the flow field displays strong roll up of trailing-edge vortex, leading to vicious interaction with the vortices from the leading edge near the plate's surface. However, the flow field in Greenblatt's experiments show more separated flow without a distinct trailing edge vortices, although there seems to be Kelvin-Helmholtz vortices in the separating shear layer at the trailing edge. This may be due to the three-dimensionality in the unforced flow from the corner flow of endplates in the experiments. Also, since the smoke was introduced upstream of the leading edge in the experiments, it may not clearly capture roll up of shear layers at the trailing edge. We show later that there is a much better correspondence in the forced flow.

### 5.3 Actuation at $\alpha = 10^\circ$

We first consider the actuation at an angle of attack of  $\alpha = 10^\circ$ . In Figure 5.7 we compare the streaklines of the controlled flow (at  $F^+ = 0.42$ ) at an instant of time to the smoke visualization

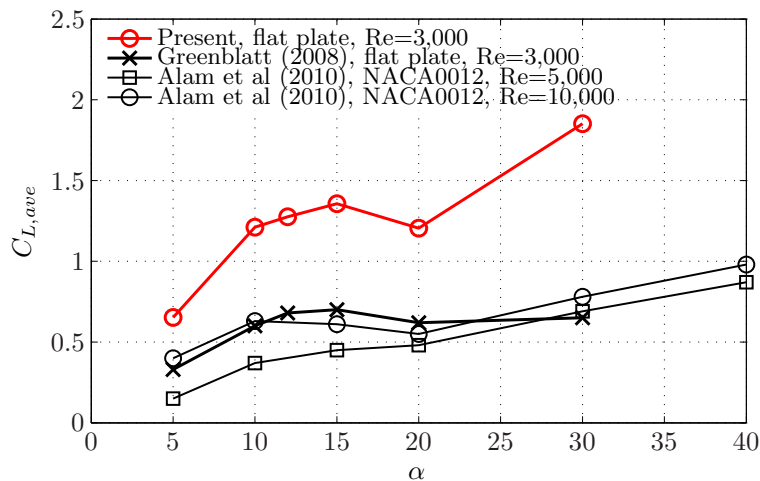
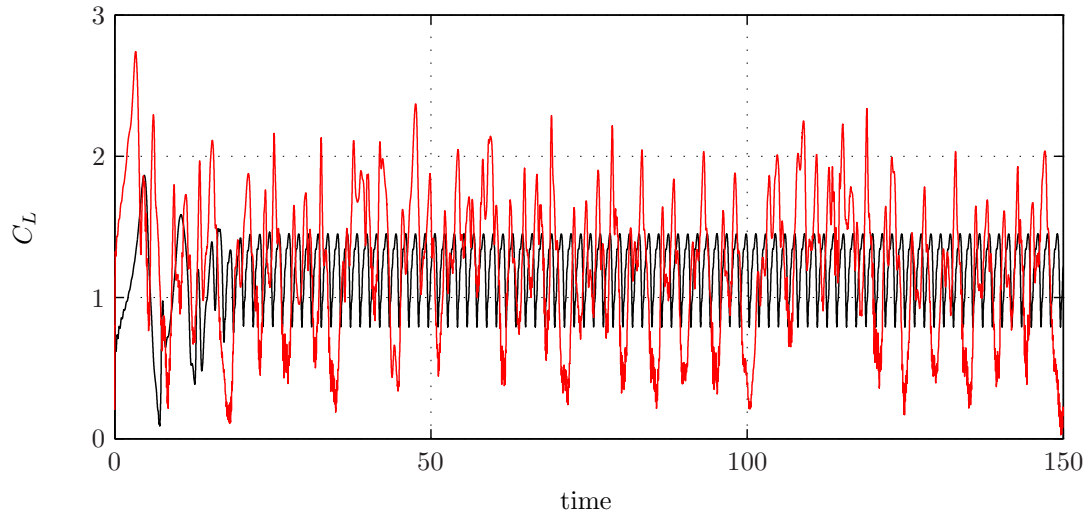


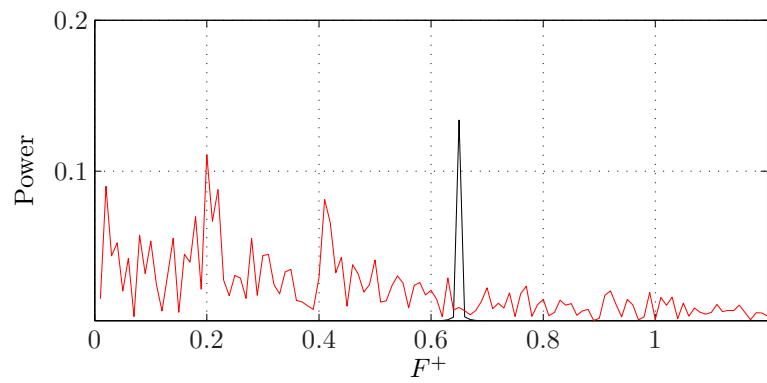
Figure 5.3: Average lift coefficient of the baseline flow, comparing results here with experimental data by Greenblatt *et al.* (2008) at  $Re = 3,000$  and by Alam *et al.* (2010) at  $Re = 5,000$  and  $10,000$ .

of Greenblatt *et al.* (2008). This frequency corresponds to the maximum lift enhancement observed in any of the experimental conditions. Figure 5.7(b) was selected from a series of snapshots within a periodic shedding cycle from the simulations to match the experimental smoke visualization. In Figure 5.8, we also present the streaklines and vorticity field at the moment of minimum and maximum lift and time corresponding to the maximum of the input waveform to the actuator. The time history of the lift and the input waveform is presented in Figure 5.9. By contrast with the baseline (uncontrolled) flow, the forced flow is in very good visual agreement with the experiments. It seems likely that the uniform actuation across the span of the wing forces more two-dimensional flow structures.

Greenblatt *et al.* (2008) presented Figure 5.7(a) as a representative snapshot of best lift enhancement at  $\alpha = 10^\circ$  and noted that the control produces a long, relatively high aspect-ratio bubble in the streamwise direction on the upper surface. Although this is also the case in our simulation (Figure 5.7(b)), we find that the corresponding lift is not at the maximum at this instant. The control is applied shortly after the shown phase (Figure 5.8(c)). The control pinches off the long bubble and allows a LEV to form and the maximum lift is achieved (Figure 5.8(b)). Also, throughout the shedding cycle, the trailing-edge vortex rolls up, not at the trailing edge, but more downstream in



(a) Lift history



(b) Lift history

Figure 5.4: Lift and power spectrum of baseline flow at  $\alpha = 10^\circ$  (black) and  $\alpha = 20^\circ$  (red).

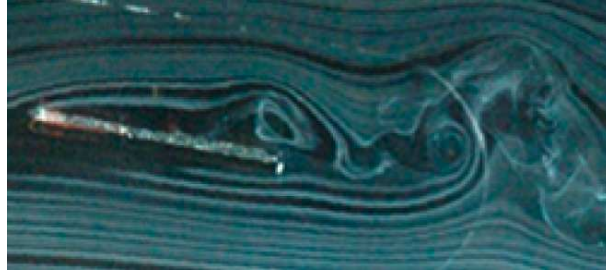
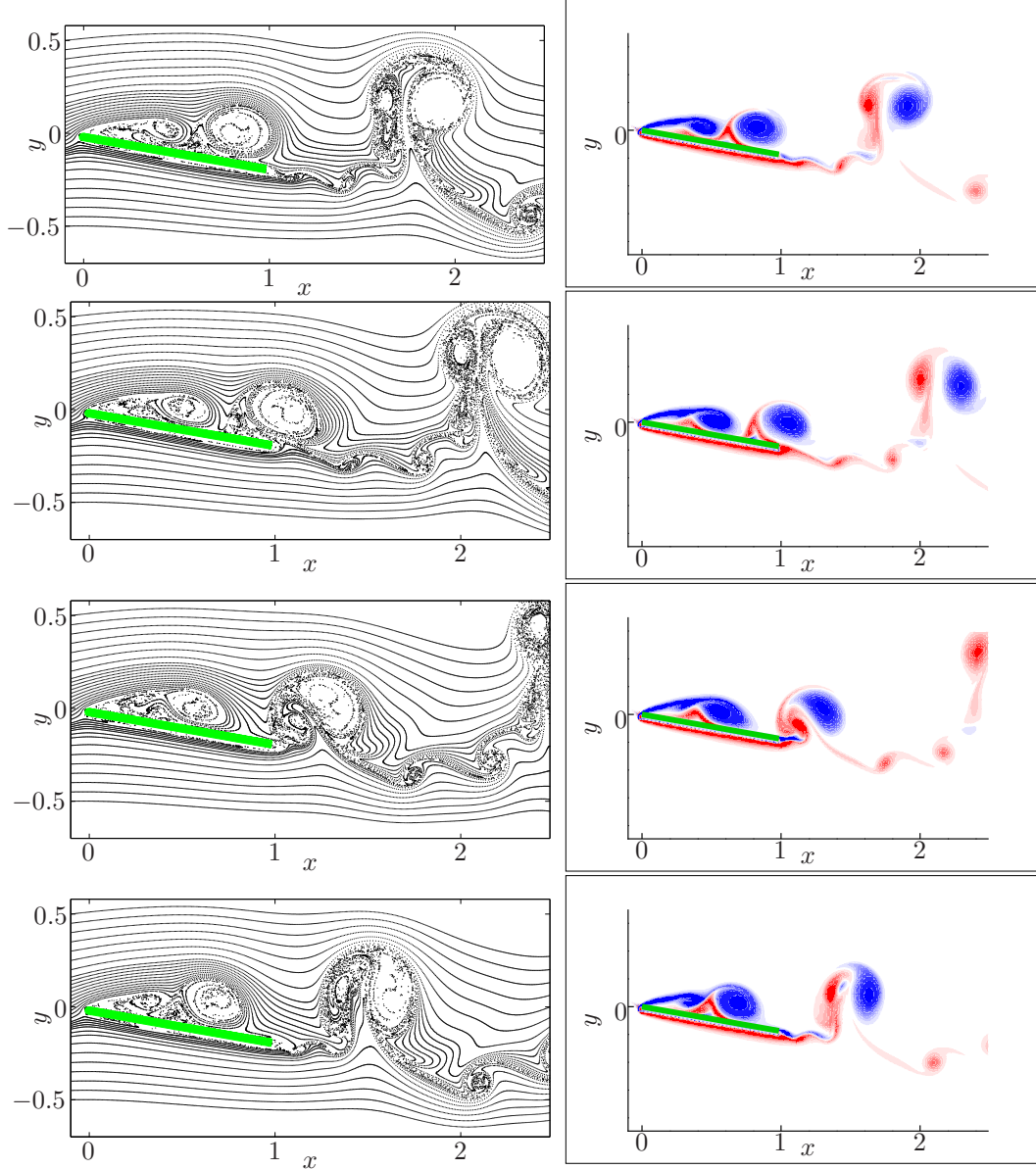
(a) Greenblatt *et al.* (2008): baseline at  $\alpha = 10^\circ$ (b) Present simulation: baseline at  $\alpha = 10^\circ$ (c) Present simulation: baseline at  $\alpha = 10^\circ$ 

Figure 5.5: (a) Smoke-visualization by Greenblatt *et al.* (2008), and (b) streaklines and (c) vorticity field from present simulation of baseline flow ( $\alpha = 10^\circ$ ).

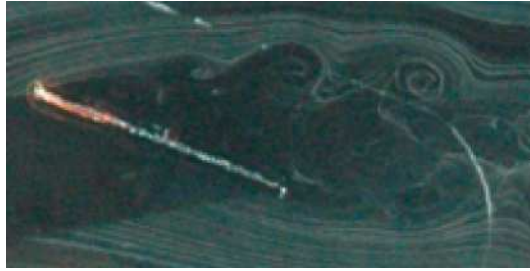
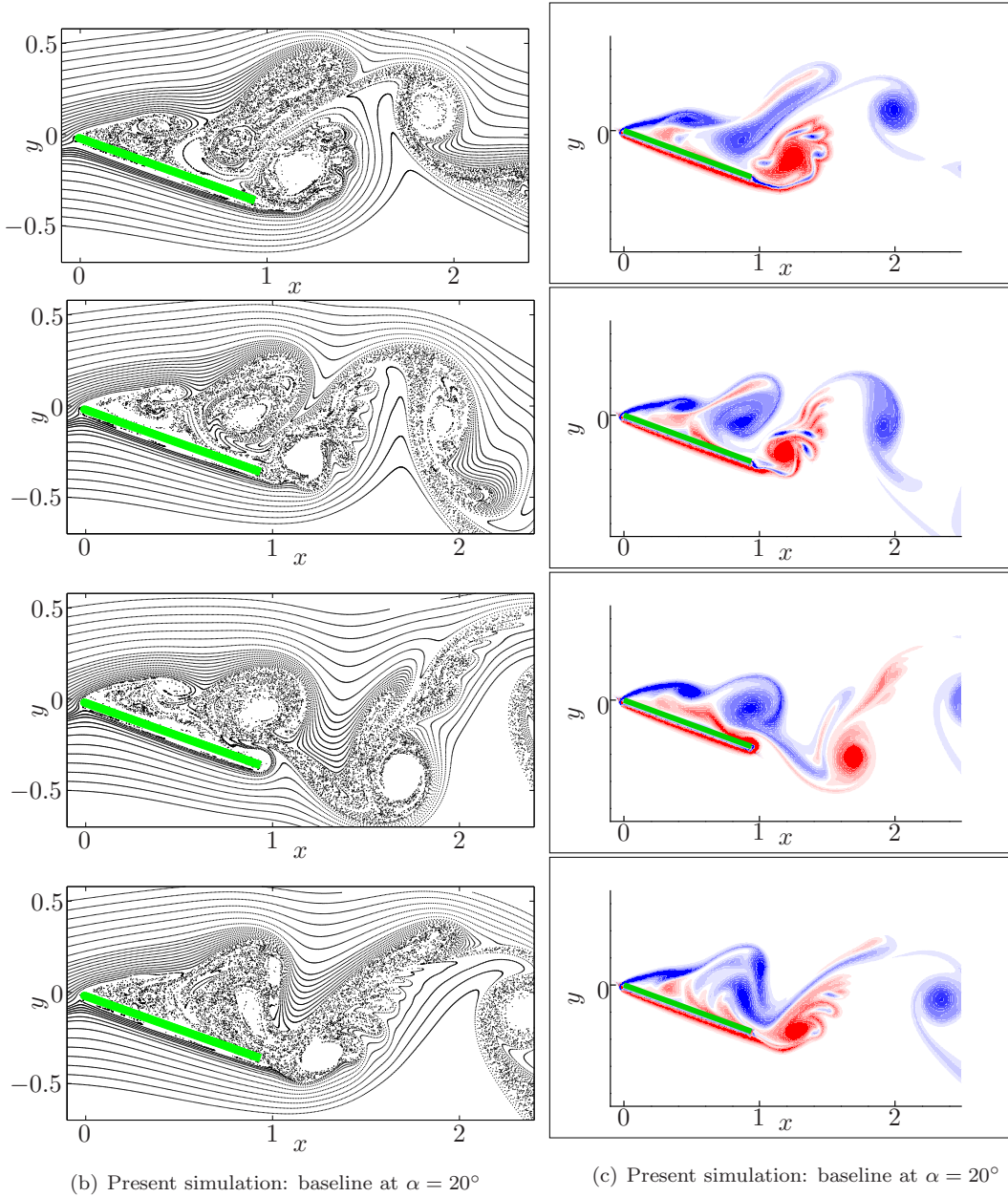
(a) Greenblatt *et al.* (2008): baseline at  $\alpha = 20^\circ$ 

Figure 5.6: (a) Smoke-visualization by Greenblatt *et al.* (2008), and (b) streaklines and (c) vorticity field from present simulation of baseline flow ( $\alpha = 20^\circ$ ).

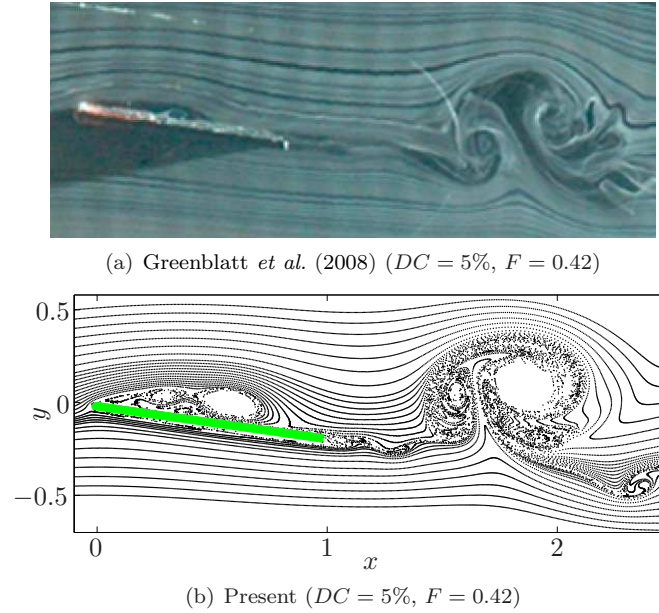


Figure 5.7: (a) Smoke-visualization by Greenblatt *et al.* (2008) and (b) streaklines of fluid particles of actuated flow with  $DC = 5\%$ ,  $F = 0.42$  ( $\alpha = 10^\circ$ ).

the wake. The main difference between the baseline and controlled flow seems to be maintaining negative vorticity near the plate's surface during most of the shedding cycle to minimize interference from the trailing-edge vortex.

Figure 5.10 investigates the dependence of controlled limit cycles on forcing frequencies  $F^+$  at two different duty cycles ( $DC = 5\%$  and  $100\%$ ). Rectangular pulse was used with  $DC = 5\%$  (see actuation profile in Figure 5.9) and a continuous sinusoidal waveform was used for  $DC = 100\%$  cases. Pulses with duty cycle of  $5\%$  phase locked the flow over the forcing frequencies  $0.4 \leq F^+ \leq 1.5$  whereas continuous sinusoidal ( $DC = 100\%$ ) phase locked the flow over  $0.6 \leq F^+ \leq 2.2$ . Obviously, as the duty cycle is varied, the harmonic content of the forcing waveform is changed. For  $DC = 100\%$ , the input is sinusoidal, while, in the limit as DC goes to zero, the forcing is a train of impulses. For low frequency near  $F^+ < 0.5$ , the higher harmonics of the pulses seem to have stabilizing effect, whereas they seem to have destabilizing effect for high frequency  $F^+ > 1.5$ .

It is interesting to note that for continuous sinusoidal forcing ( $DC = 100\%$ ) at high frequency  $F^+$  near 1.8, the flow is stabilized near its *minimum* lift. Figure 5.11 and Figure 5.12 shows an

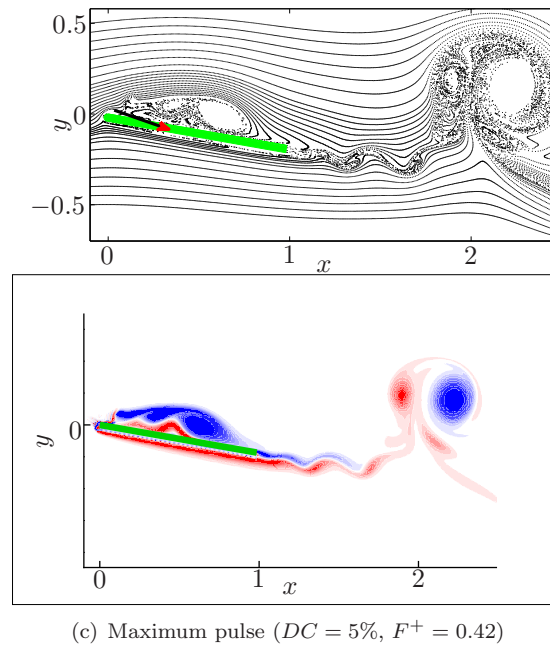
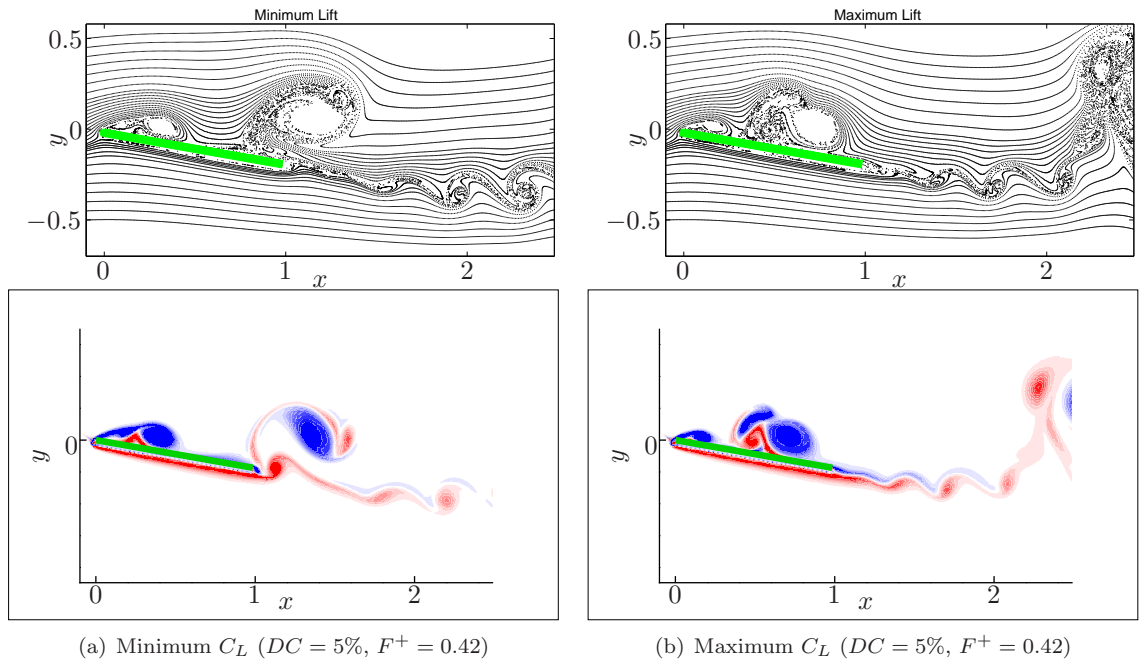


Figure 5.8: Streaklines (top) and vorticity field (bottom) at (a) minimum and (b) maximum lift and (c) maximum pulse with  $DC = 5\%$  and  $F^+ = 0.42$  ( $\alpha = 10^\circ$ ).

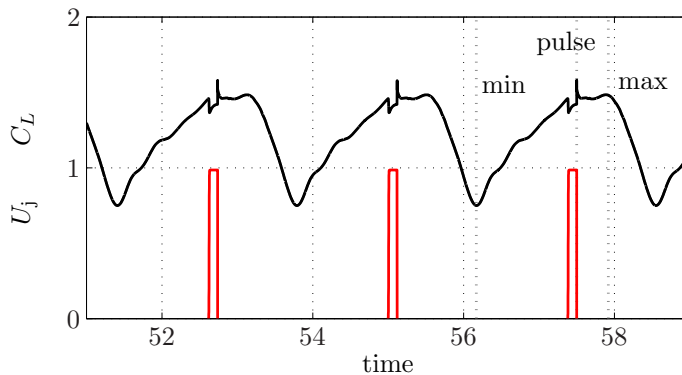


Figure 5.9: Time history of lift and  $U_j$  of actuated flow at  $F^+ = 0.42$  with  $DC = 5\%$  ( $\alpha = 10^\circ$ ). Dashed lines indicate the moment of minimum (min) and maximum (max) lift and time corresponding to the maximum of the input waveform to the actuator (pulse).

example of the time history and flow field of the phase-locked flow at high frequency actuation at  $F^+ = 1.9$ . At this high frequency, the pulses generate a train of small vortices that advect down the plate surface without mutual interactions.

## 5.4 Actuation at $\alpha = 20^\circ$

We now consider actuation at an angle of attack of  $20^\circ$ . The average lift increase over a range of forcing frequencies with a duty cycle of 5% is compared to the results by Greenblatt *et al.* (2008) in Figure 5.13. We examine the long time averaged lift increment since this is what was presented in Greenblatt *et al.* (2008). For  $0.4 \leq F^+ \leq 0.7$ , the simulations produce a flow that is phase locked to the actuation. For these phase-locked shedding cycles, the resulting average-lift increase is consistent with that of Greenblatt's. For other forcing frequencies, the actuation is exciting a lower frequency response that is modulating the vortex shedding, leading to aperiodic lift response and a larger lift oscillation. Even though the data shown in Figure 5.13 represent a long time average ( $t \approx 150$ ), it is still less than half as long as Greenblatt's average over  $t > 400$ . This could explain the fluctuations in the average lift for chaotic limit cycles that are present in Figure 5.13.

Streaklines of the controlled flow at an instant of time are compared to the smoke visualization snapshot of optimal control at  $F^+ = 0.42$  by Greenblatt *et al.* (2008). The similarity between the two

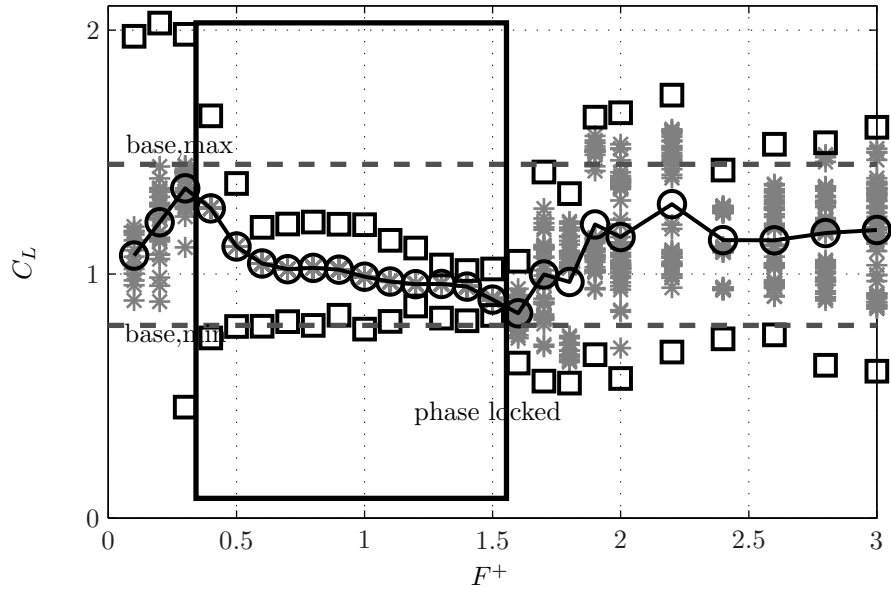
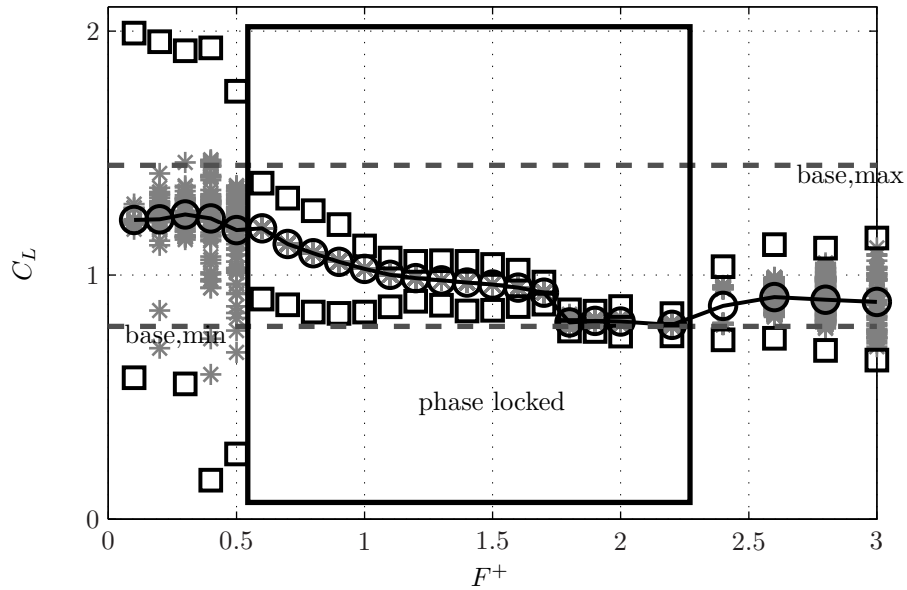
(a)  $DC = 5\%$ (b)  $DC = 100\%$ 

Figure 5.10: Sinusoidal pulse with (a)  $DC = 5\%$  and (b)  $100\%$  ( $\alpha = 10^\circ$ ). Squares represent the maximum and minimum lift, and circles represent overall average lift. The period-averaged lift once per cycle of actuation is plotted in gray(\*), and the flow is observed to be periodic (phase-locked) when these collapse to a single point (meaning they are the same each cycle).

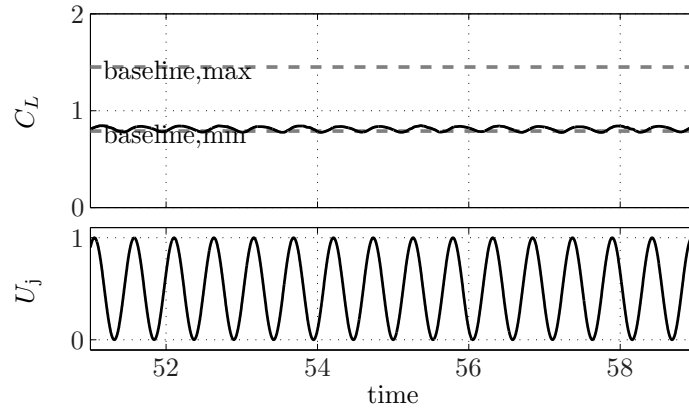


Figure 5.11: Time history of lift and  $U_j$  of actuated flow at  $F^+ = 1.9$  with  $DC = 100\%$  ( $\alpha = 10^\circ$ ).

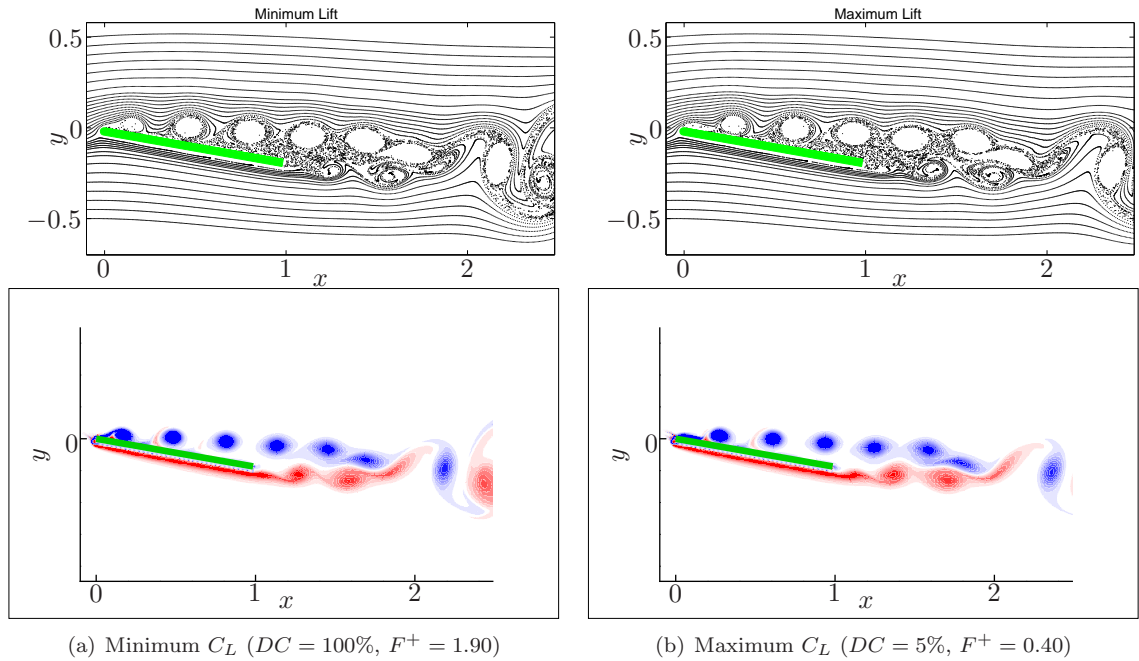


Figure 5.12: Streaklines (top) and vorticity field (bottom) at (a) minimum and (b) maximum lift with  $DC = 100\%$  and  $F^+ = 1.90$  ( $\alpha = 10^\circ$ ).

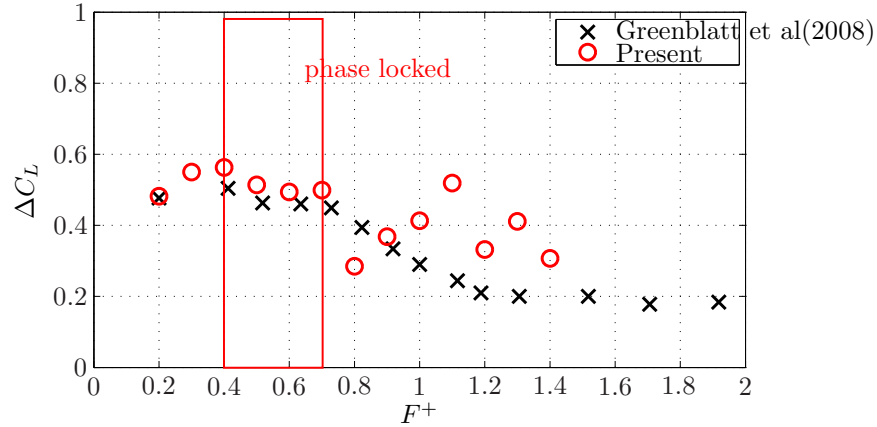


Figure 5.13: Average lift increase over a range of forcing frequency at  $\alpha = 20^\circ$  with 5% duty cycle (DC) compared to the results by Greenblatt *et al.* (2008).

is quite remarkable. Again, the coherent actuation along the entire span appears to reduce the effect of the three-dimensionality. Greenblatt *et al.* (2008) presented Figure 5.14(a) as a representative snapshot of optimal control to explain the effect of control, namely that the shear layer at the leading edge rolls up into a vortex that attaches to the airfoil surface. By examining visualizations at different phases of actuation, we find that the comparable instantaneous flow field actually corresponds to near the minimum lift in our simulation (Figure 5.15(a)). As the leading-edge vortex (LEV) grows bigger, it is kept closer to the plate due to the strong downwash from the shed trailing-edge vortex (TEV). The control (a short pulse) pinches off the LEV, immediately allowing the next LEV to form. The resulting vortices, with their cores nearly equidistant, stay closer to the plate's surface and produce a low pressure region that increases the lift, resulting in the maximum lift (Figure 5.15(b)). Compared to the baseline flow field, the control (short pulses in this case) seems to act as a pinch-off mechanism of the LEV and enforces regular formation of each subsequent LEV. This maintains several vortices on the plate for most of the shedding cycle, pushing newly forming TEV downstream to the wake. Finally, this process prevents these newly forming TEV from pushing the LEV up, but rather uses downwash from the TEV in the wake to keep the vortices from the leading edge closer to the plate's surface.

We find that, while low frequency actuation enhances lift by keeping two to three vortices on the

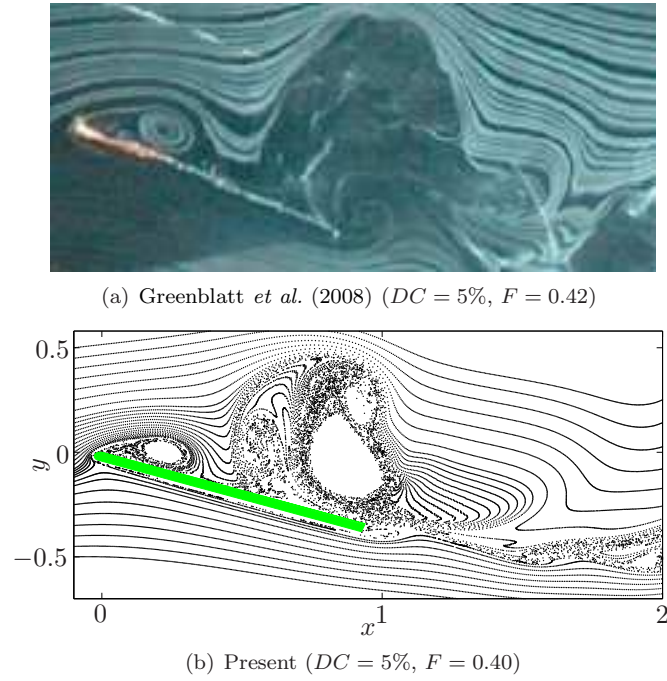


Figure 5.14: (a) Smoke-visualization by Greenblatt *et al.* (2008) and (b) streaklines of fluid particles of actuated flow with  $DC = 5\%$ ,  $F = 0.40$  ( $\alpha = 20^\circ$ ).

plate's surface, with minimum interference from the TEV, high frequency actuation does not provide enough time for a sufficiently large LEV to form, but instead generates a train of smaller vortices. This results in less of the aforementioned favorable influence on the formation of the TEV, but leads to nonlinear interaction of these small vortices with the TEV near the plate. Thus, actuation at high frequency tends to generate more chaotic lift response and large lift oscillations.

The effect of varying the duty cycle is examined in Figure 5.16, which shows the period-averaged lift over each cycle of actuation as  $F^+$  is varied. First, we observe that the range of forcing frequencies that produce phase-locked limit cycles decreases as duty cycle is increased. At 50% duty cycle, only forcing at  $F^+ = 0.6$  led to a phase-locked limit cycle. Also, for high duty cycles ( $DC \geq 50\%$ ) we observe a period doubling in the lift's response to high forcing frequency,  $1.0 \lesssim F^+ \lesssim 1.4$ . For these cases, the response was periodic at half the frequency of the forcing frequency, thus each shedding cycle occurs over two forcing cycles.

Of the various frequencies and duty cycles considered, we find that a phase-locked response

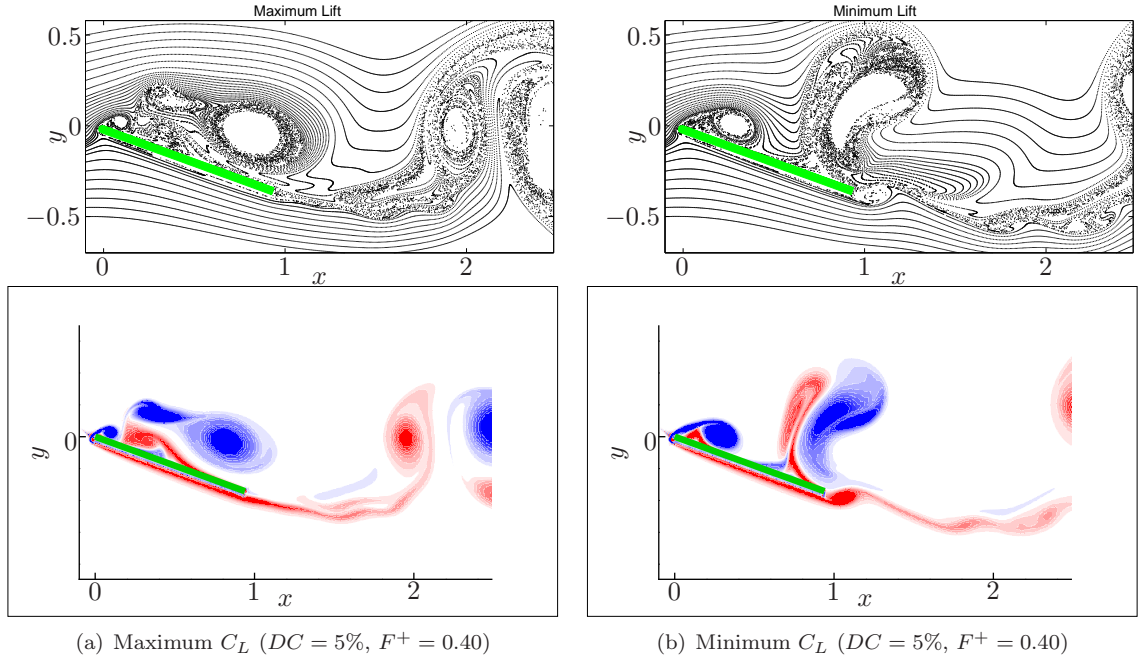


Figure 5.15: Streaklines (top) and vorticity field (bottom) at (a) minimum and (b) maximum lift with  $DC = 5\%$  and  $F^+ = 0.40$  ( $\alpha = 20^\circ$ ).

occurred when forced at  $F^+ = 0.6$ , or its first harmonic at  $F^+ = 1.2$  for  $DC \geq 50\%$ . In the latter case, the vortex shedding cycle still occurred at  $F^+ = 0.6$ . It is interesting to note that this  $F^+ = 0.6$  corresponds to  $St = 0.2$  which agrees with the wake Strouhal number for vortex shedding behind two-dimensional bluff bodies.

In the region of forcing frequencies with a phase-locked response, similar lift enhancement is observed with duty cycle of 5% and 50%, which is consistent with the results by Greenblatt *et al.* (2008). It was also observed from the results at  $Re = 300$  that a pulsatile waveform resulted in higher lift than a continuous sinusoidal forcing (holding  $U_{jet}$  constant). This is consistent with the observations by Amitay & Glezer (2006) at  $Re = 3.1 \times 10^5$  that the separated flow over a stalled airfoil is receptive to pulses of very short duration compared to the the shedding period.

We now examine the phase-locked response at  $F^+ = 0.5$  and  $F^+ = 0.6$  in more detail. Figure 5.17 compares time histories of lift response that are phase-locked at  $F^+ = 0.5$  and the corresponding

streaklines and vorticity are shown in Figure 5.18 and Figure 5.19, respectively. Flow fields at the minimum lift are similar for the cases shown. However, the flow fields at the maximum lift display different LEV structures on the plate's surface. Actuation at  $F^+ = 0.50$  with  $DC = 5\%$  pinches off the LEV about halfway between the minimum and maximum lift, resulting in approximately equal distance between the pinched-off vortex and the newly forming LEV. For actuation at  $F^+ = 1.0$  with  $DC = 50\%$  and  $100\%$ , each shedding cycle consists of two forcing cycles, with the first actuation peak at the minimum lift, and the second actuation peak shortly before the maximum lift. At the minimum lift, as the new vortex is forming at the leading edge, the first pulse separates it into two distinct structures, and the following pulse forces them to pinch off as a vortex pair. A short time later, maximum lift is achieved as a vortex pair and the newly forming vortex together produce a low pressure region on the plate's surface to enhance the lift.

Figure 5.20 compares time histories of limit cycles that are phase-locked at  $F^+ = 0.6$  and the corresponding streaklines and vorticity fields are shown in Figure 5.21 and Figure 5.22, respectively. By comparing the lift history for the different duty cycles, several observations can be made. First, the actuation profile in Figure 5.20(d) ( $F^+ = 1.20$  with  $DC = 100\%$ ) contains an extra pulse over each shedding period than the actuation profile in Figure 5.20(b) ( $F^+ = 0.60$  with  $DC = 50\%$ ). However, this extra pulse did not affect periodicity of the shedding cycle nor change its lift characteristics, i.e. minimum, maximum, and average lift. Although the extra pulse generates a vortex pair near the leading edge, the streaklines over the vortex pair (Figure 5.20(d)) are similar to the streaklines over the single vortex in Figure 5.20(b).

Also, forcing at  $F^+ = 0.6$  with  $DC = 5\%$  resulted in phase-locked response (Figure 5.20(a)), whereas, the extra pulse that exists in  $F^+ 1.20$  (with the same  $DC = 5\%$ ) destabilizes the lift limit cycle and leads to an aperiodic response. Forcing at  $F^+ = 1.2$  stabilized the lift limit cycle only with  $DC > 50\%$ , indicating that the pulse cannot be too narrow in order to result in stable limit cycle. Since dynamics of the vortex pairing resulting from period doubling can be more sensitive to disturbances than a single vortex, pulses might need to be gradual (smooth) for the vortices to have the same dynamics over every shedding period. Also, the pulses cannot seem be too broad in order

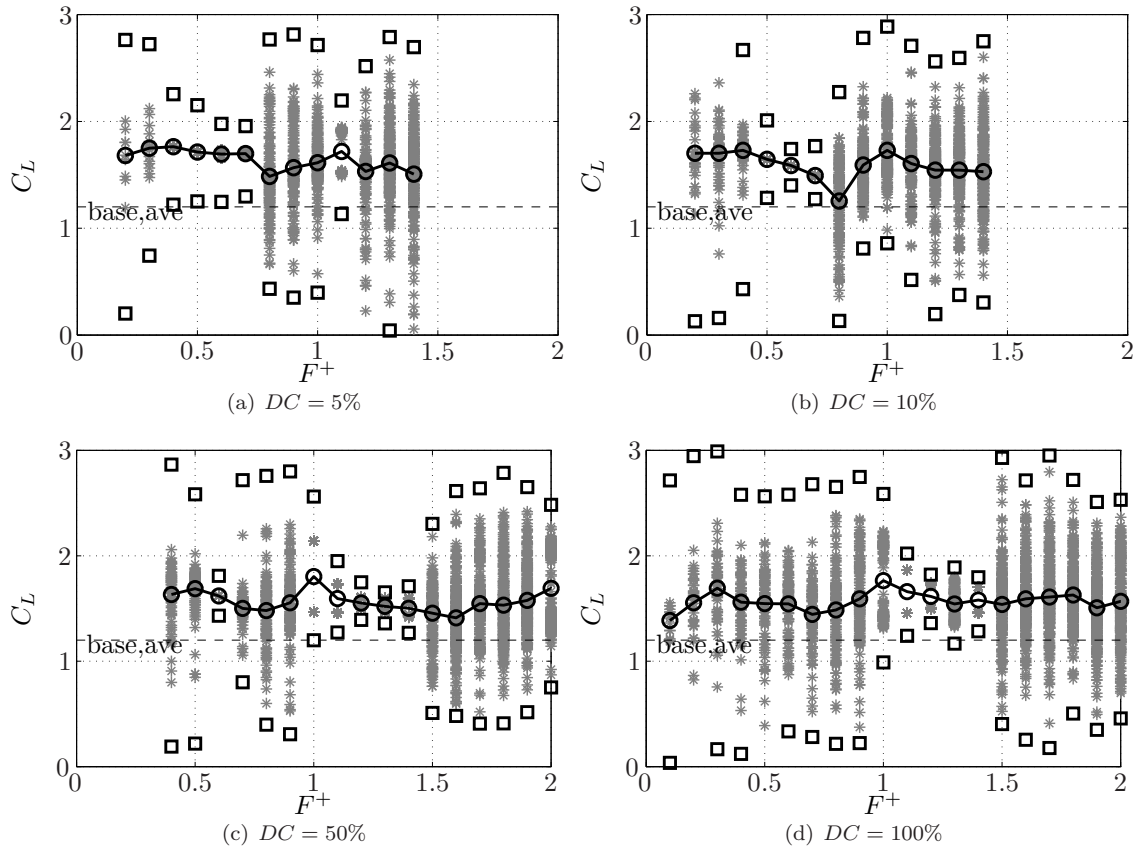


Figure 5.16: Sinusoidal pulse with  $DC = 5\%$ ,  $10\%$ ,  $50\%$ , and  $100\%$  ( $\alpha = 20^\circ$ ). Squares represent the maximum and minimum lift, and circles represent overall average lift. The period-averaged lift once per cycle of actuation is plotted in gray(\*), and the flow is observed to be periodic (phase-locked) when these collapse to a single point (meaning they are the same each cycle).

to effectively pinch off the vortices, since actuating at  $F^+ = 0.6$  resulted in phase-locked limit cycles only for  $DC < 100\%$ .

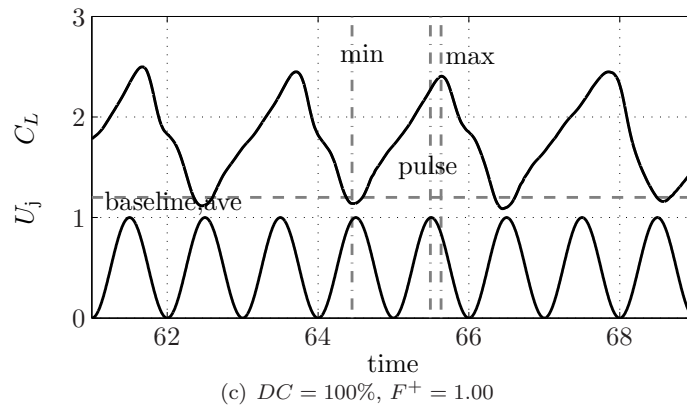
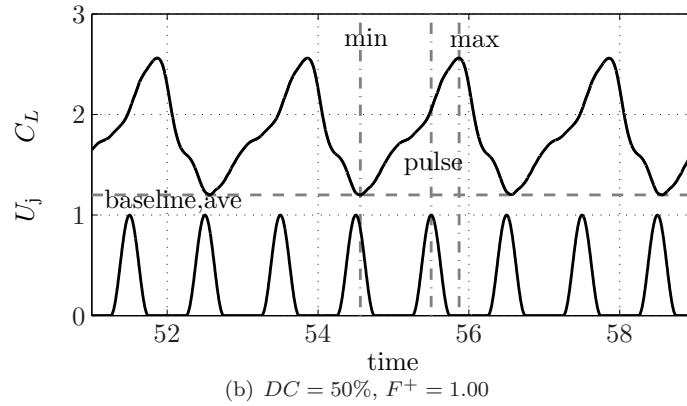
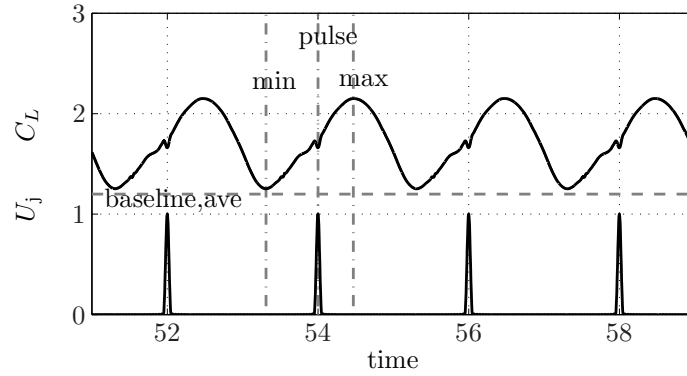


Figure 5.17: Time history of lift of actuated flow phase-locked at  $F^+ = 0.5$  ( $\alpha = 20^\circ$ ).

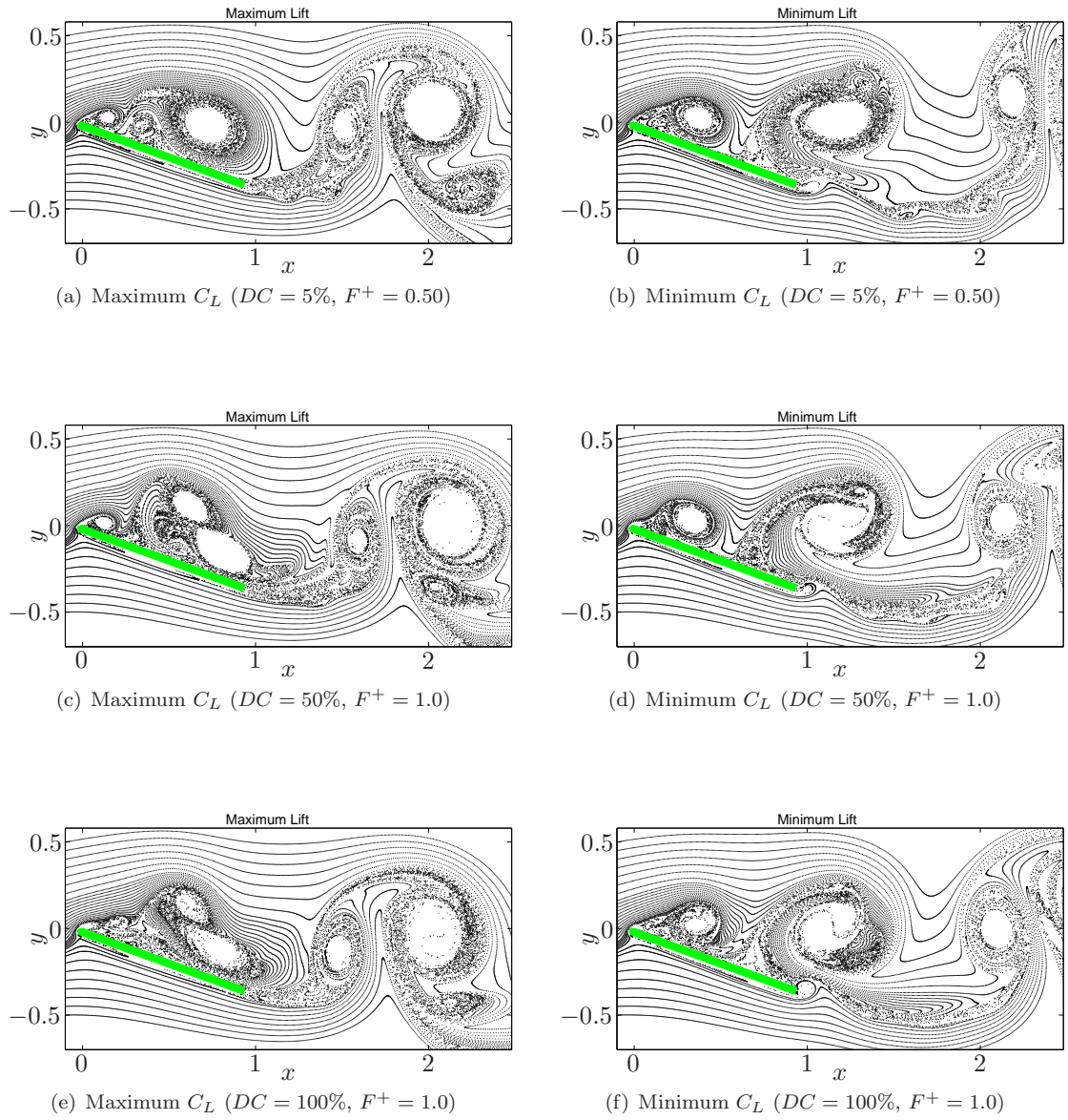


Figure 5.18: Streamlines of actuated flow phase-locked at  $F^+ = 0.5$  ( $\alpha = 20^\circ$ ).

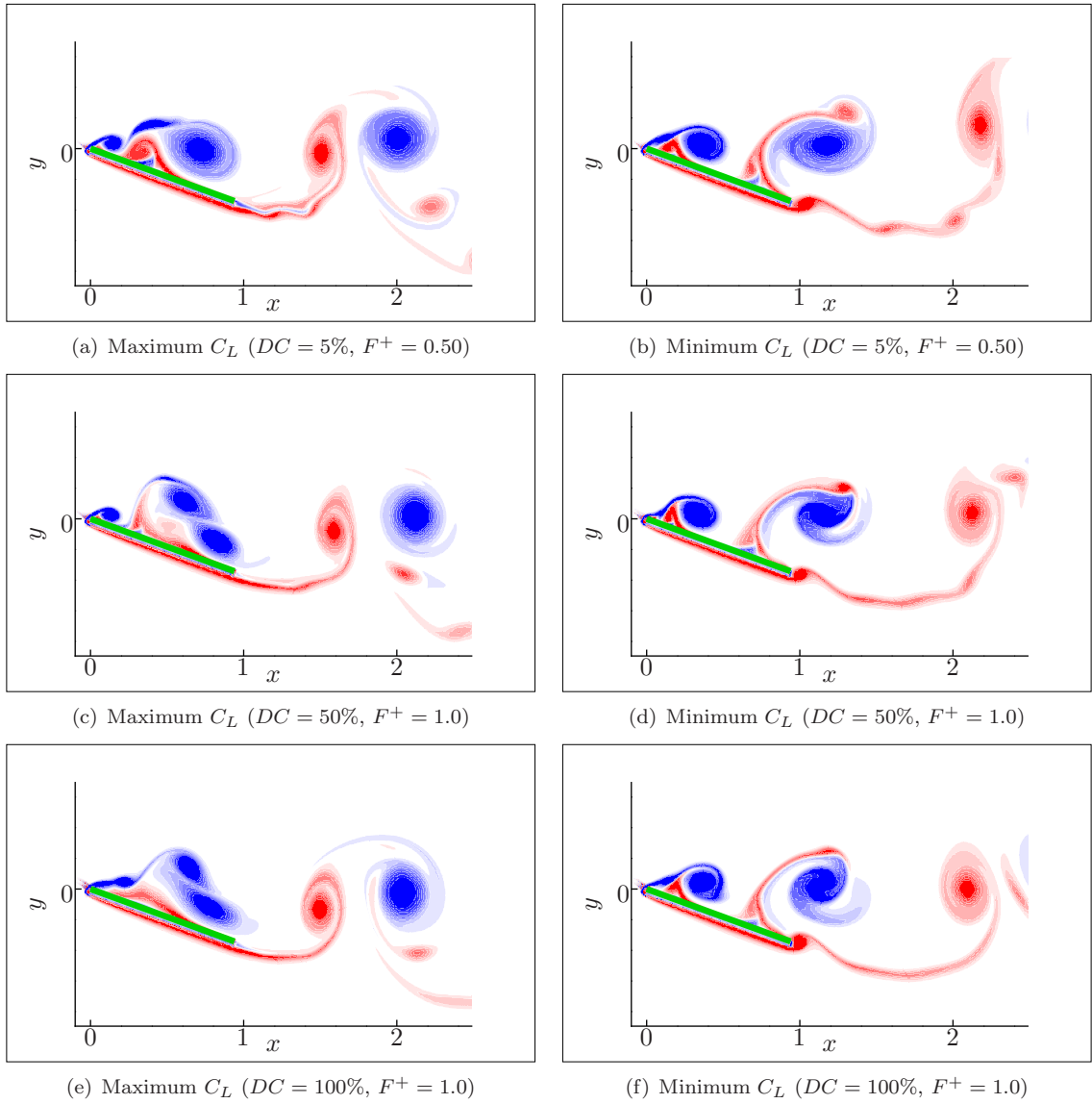


Figure 5.19: Vorticity field of actuated flow phase-locked at  $F^+ = 0.5$  ( $\alpha = 20^\circ$ ).

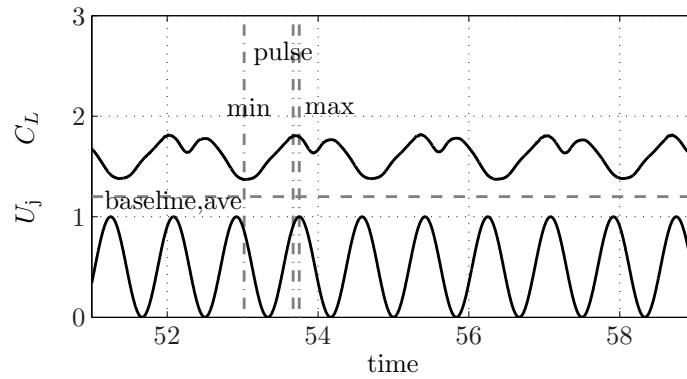
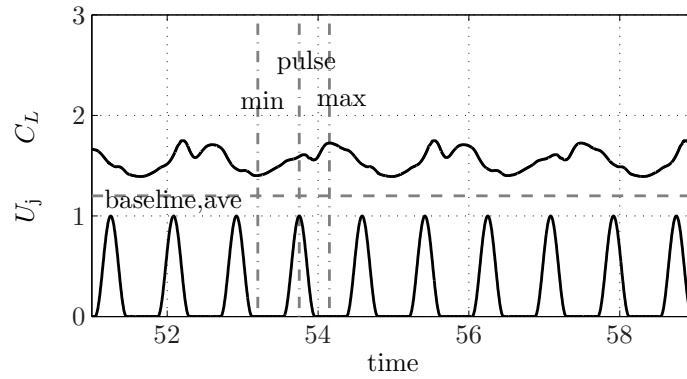
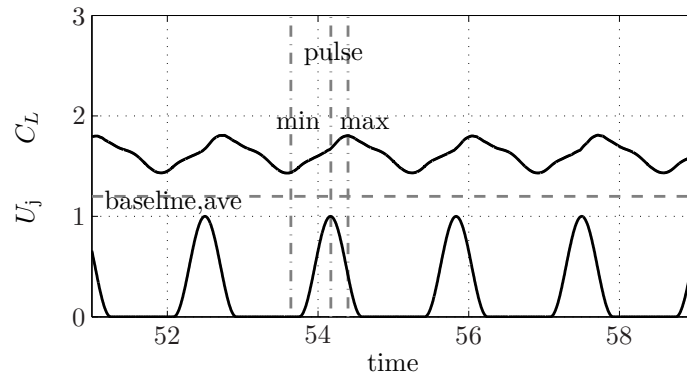
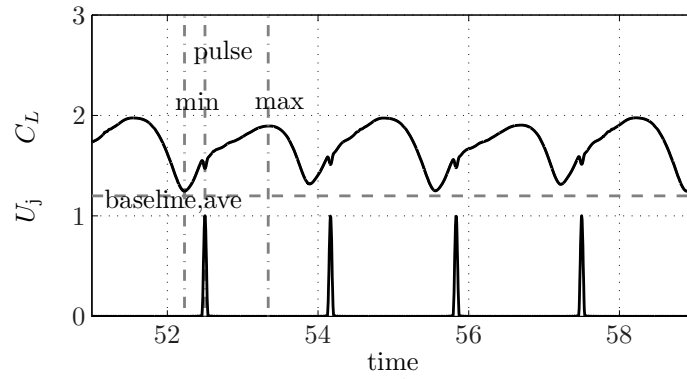


Figure 5.20: Time history of lift of actuated flow phase-locked at  $F^+ = 0.6$  ( $\alpha = 20^\circ$ ).

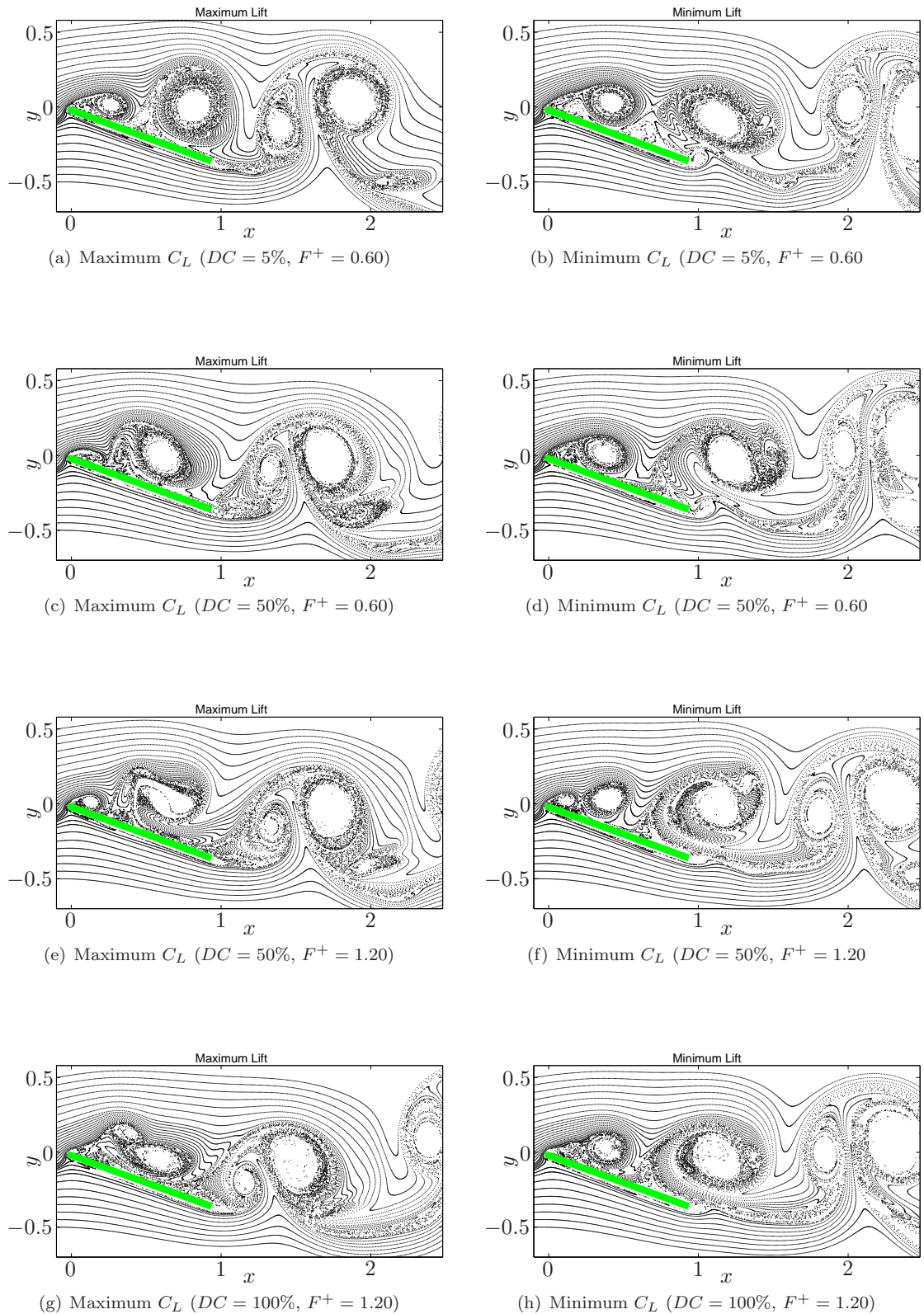


Figure 5.21: Streaklines of actuated flow phase-locked at  $F^+ = 0.6$  ( $\alpha = 20^\circ$ ).

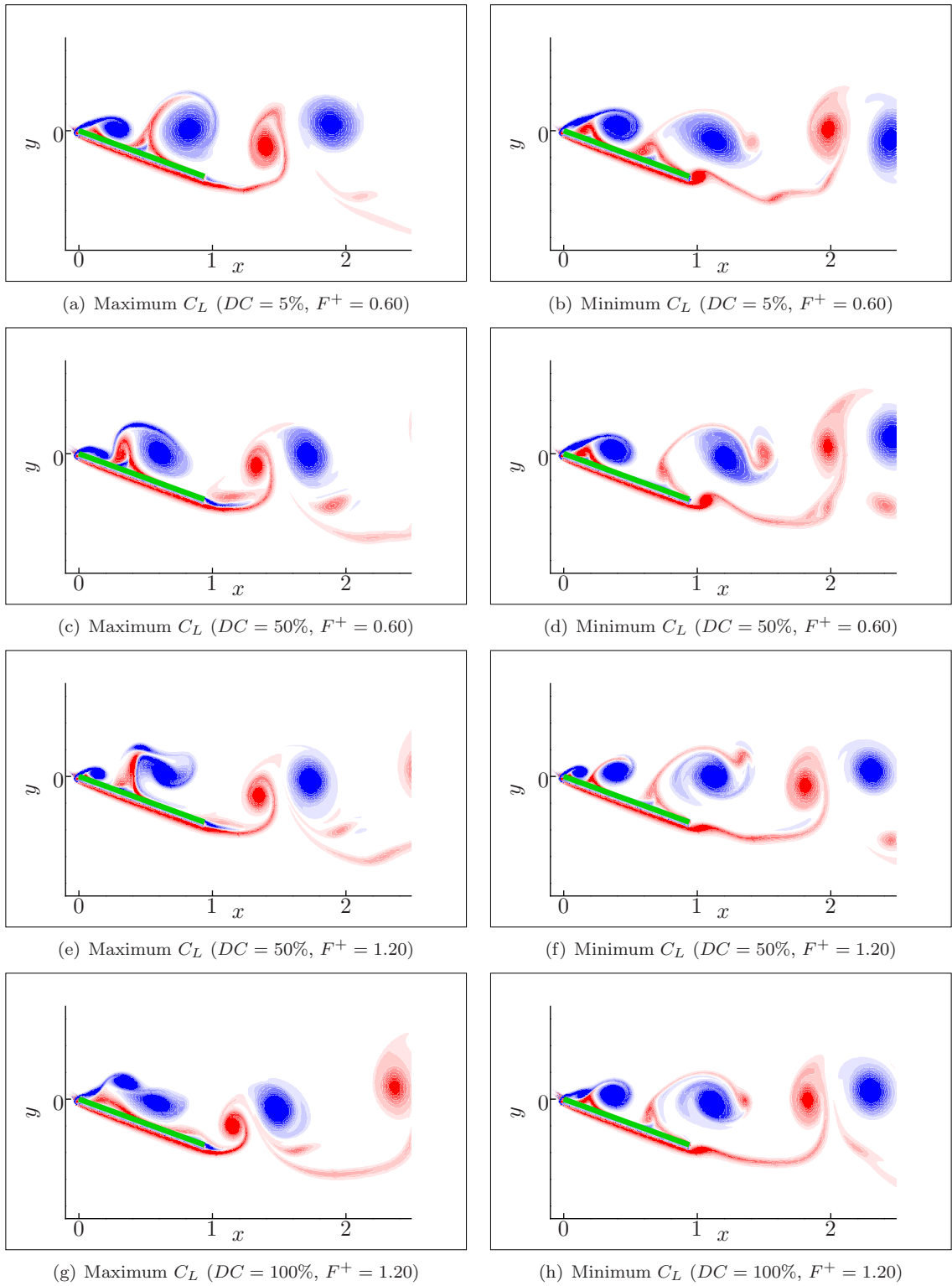


Figure 5.22: Vorticity field of actuated flow phase-locked at  $F^+ = 0.6$  ( $\alpha = 20^\circ$ ).

# Chapter 6

## Conclusions

In this thesis, we examined flow control and the potentially favorable effects of feedback, associated with unsteady actuation in separated flows over airfoils. We presented results from a numerical study of unsteady actuation on a two-dimensional flat plate at post-stall angles of attack at Reynolds number of 300 and 3000. At  $Re = 300$ , with a sinusoidal forcing, we showed that the highest-lift vortex shedding cannot be maintained with conventional open-loop forcing because the flow does not phase lock with the actuation signal. We designed our physically motivated phase controller to show that the feedback may provide continuous modification of the control input according to the response of the flow system to achieve higher lift. Also, rather than optimizing the phase of the control relative to the lift using only sinusoidal waveform, we investigated the possibility of optimizing the lift using more general (non-sinusoidal) actuation waveforms using a gradient-based approach. This optimization over a finite horizon resulted in a periodic waveform, however, implementing in open loop was fragile to disturbances and sensitive to different initial conditions. In order to overcome this obstacle, we designed a controller that uses the previously developed phase-locking strategy, but was applied to the more complicated waveforms deduced by the optimization. This provided a robust and practical approach to giving near-optimal performance. Moreover, the optimal waveform was not sinusoidal, but more pulse-like. Using the feedback strategy, we showed that a sinusoidal pulse whose width is as small as 25% of the actuation period (duty cycle of 25%) resulted in a similar lift enhancement as a continuous sinusoidal (duty cycle of 100%), when the control was nearly in phase with the lift in both cases. Finally, we considered a higher  $Re$  of 3000 and investigate the lift

response to different waveforms motivated by the nature of the optimal forcing found at  $Re = 300$ . We considered different frequencies and actuation waveforms with different duty cycles. We showed that for certain frequencies and actuator waveforms, there occur stable limit cycles in which the flow is phase locked to the actuation. Forcing with duty cycle of 5% was as effective as higher duty cycles or a continuous sinusoidal. Also, as the duty cycle was increased, the range of forcing frequencies for the phase-locked limit cycles decreased.

## 6.1 Control at $Re = 300$

### 6.1.1 Sinusoidal Forcing

Open-loop control at the leading and trailing edges directed upstream or downstream parallel to the freestream was investigated. In general, forcing at its natural shedding frequency,  $\omega_f = \omega_n$ , resulted in larger oscillations in the magnitude of force on the plate. The increase of the force on the plate also results in the increase of both lift and drag coefficients since they are only the vertical and horizontal component of the force vector, respectively. However, we only considered the lift component for the purpose of demonstrating the control algorithm to achieve high vortex-induced force on the plate. Upstream actuation at both leading and trailing edges led to the enhancement of average lift. However, lower average lift was observed when the actuation was directed downstream, parallel to the flow. The most effective lift enhancement was observed with upstream actuation at the trailing edge. This upstream actuation increases the local velocity gradient which increases the magnitude of circulation feeding into the vortical structure generated from the edge. In the case of trailing-edge actuation, this induces a stronger downwash near the trailing edge and the LEV is pulled down closer to the plate as a result.

The hydrodynamics were phase locked to the actuation at lower angle of attack,  $\alpha$ . However, at sufficiently high  $\alpha$  ( $\alpha \geq 30^\circ$  for trailing-edge actuation and  $\alpha \geq 20^\circ$  for leading-edge actuation), actuation led to the excitation of a subharmonic resonance. The subharmonic limit cycle consisted of several periods with a different period-averaged lift over each actuation period. When the forcing

signal was at a particular phase shift relative to the lift signal (in-phase at  $\alpha = 50^\circ$ ), it was observed that the actuation achieved the highest period-averaged lift. However, the succeeding period became slightly out of phase and the lift decreased.

The highest period-average lift within the subharmonic limit cycle was higher than the average lift of any phase-locked flow with open-loop forcing. Particularly with upstream actuation at the trailing edge, this period-averaged lift was higher than the maximum lift obtained during natural shedding. We also observed that if the forcing frequency was adjusted slightly from the value associated with the natural vortex shedding, it was possible to obtain a phase-locked response that matched individual cycles of the subharmonic response. This suggested that feedback might be useful to slightly adjust the frequency and or phase of actuation to lock it to a particular phase of the lift, thus achieving a phase-locked flow with the maximal period-averaged lift over every cycle of acutation.

Thus, we feedback lift in order to output a sinusoidal forcing with a specified phase shift relative to the lift signal. This feedback compensator was able to phase lock the flow at the desired vortex shedding limit cycle that was not sustainable with any of the open-loop periodic forcing. The feedback achieved the highest-lift limit cycle near zero phase shift, with as high as 83% increase in the average lift coefficient (twice the lift increase of open-loop forcing at  $\omega_n$ ). This feedback should provide a greater robustness with respect to disturbances, such as changes in flight conditions, since it provides a continuous modification of the forcing relative to the measured lift.

### 6.1.2 Optimization of the Control Waveform

With the sinusoidal forcing and feedback, it proved possible to optimize the phase of the control relative to the lift in order to achieve the highest possible period-averaged lift in a consistent fashion. However, it was unclear whether the sinusoidal waveform itself was optimal. Some investigators have suggested that more pulsatile forcing can achieve the same benefit with lower energy input. In order to investigate the effect of the waveform, we developed a gradient-based (adjoint) approach to optimize the control waveform. The cost function was chosen to maximize the lift force on the

plate, while penalizing the control effort. The optimization was performed with a receding horizon approach. The resulting optimized waveform was not sinusoidal, but more pulse-like, with each period composed of two distinct pulses (a primary, as well as a smaller earlier pulse). The most distinct feature of the optimal control is a gradual increase in the forcing  $\phi$  during most of the cycle, followed by a more rapid decrease after its peak. This minimal control effort after the maximum lift, combined with the short pause between the two pulses provides more energy-efficient control than sinusoidal forcing. As a result, the optimal control achieved comparable lift with about half the value of  $C_\mu$  as the sinusoidal waveform.

### 6.1.3 Feedback Control with the Optimized Waveform

Optimal control provides a periodic control waveform. However, if applied in open loop, the flow fails to phase lock onto the optimal waveform, degrading the lift performance. We designed a feedback algorithm to obtain phase-locked limit cycles. Using a Fourier representation of the optimized waveform,  $\phi_{\text{optimal}}$ , the control parameterizes the waveform in terms of its phase  $\theta(t)$ , allowing the feedback to march along  $\phi_{\text{optimal}}(\theta)$  with consistent phase difference between each of its harmonics. The control consists of the following steps : 1. A narrowband filter is used on the lift cycle to obtain a more nearly sinusoidal signal. 2. The filtered lift signal is used as input to a frequency tracking Extended Kalman Filter (EKF) to estimate the phase,  $\hat{\theta}(t)$  of the lift signal. 3. The EKF frequency estimate is used to tune the filter to avoid introducing phase lag. 4. Finally, the phase estimate  $\hat{\theta}(t)$  from EKF is used to march along  $\phi_{\text{optimal}}$ .

Feedback control of the optimized waveform was able to reproduce the high-lift limit cycle from the optimization, but starting from an arbitrary phase of the baseline limit cycle. Also, it allowed us to phase lock an essentially arbitrary waveform, thus enabling us to investigate the sensitivity of the flow to the phase shift and other features of the optimized waveform. By using fewer harmonics in the Fourier expansion of the optimized waveform, we demonstrated that smoothing the dip between the two pulses has little impact on the lift performance; this characteristic is more of an energy-saving feature. We also showed that the phase-locked limit cycle with optimized waveform was sensitive

to changes in the phase shift,  $\theta_{\text{desired}}$  from  $0^\circ$ . The sharp decrease in lift performance with negative phase shift is due to the steep drop in the optimized waveform after its peak. The lift penalty with positive phase shift indicates that the forcing is less effective after the maximum lift has occurred.

Motivated by the pulsatile waveform the optimization provided, we investigated the lift response to sinusoidal pulses of different duty cycles (percentage of the width of a sinusoidal waveform to the actuation period). The feedback was used to enforce the optimal phase shift (approximately in phase) for each control waveform. A sinusoidal pulse with a duty cycle of 25% achieved similar average lift enhancement as a continuous sinusoid when the forcing was in phase with the lift.

## 6.2 Control at $Re = 3000$

We next considered a higher  $Re$  of 3000 and investigated the nature of the optimal waveform we found at  $Re = 300$ , particularly sinusoidal pulses with different widths compared to the actuation period (duty cycle). The geometry of a flat plate with thickness of  $0.04c$  and  $Re = 3000$  were chosen in order to match the experimental studies of Greenblatt *et al.* (2008). A body force was placed at the leading edge directed parallel to the plate towards the trailing edge. The spatial and temporal characteristics of the body force were calibrated in order to mimic the plasma actuator used in the experiments. We considered two representative angles of attack,  $\alpha = 10^\circ$  and  $20^\circ$ , and investigated the response of the flow to different forcing frequencies and different control waveforms.

For both angles of attack, the optimal forcing frequency was observed to be  $F^+ \approx 0.4$  which is consistent with Greenblatt *et al.* (2008). Even though the lift and the streaklines of the baseline flow displayed differences due to the three-dimensional effect of the endplates in the experiments by Greenblatt *et al.* (2008), uniform actuation over the span seemed to generate a more two-dimensional flow in the experiments, leading to better visual agreement of the controlled flow than for the baseline case.

Greenblatt *et al.* (2008) focused on the long-time average lift and explained the effect of control using representative snapshots of smoke visualization. Here, we have used the simulation data to

examine the time-dependent structures in the flow field, particularly the flow structures occurring at the moments of minimum and maximum lift, and the phase of pulses relative to the lift. The main difference observed between the baseline and the controlled flow was that the control maintained several vortices on the plate's surface during most of the shedding cycle, pushing newly forming TEV downstream to the wake. We found that the lift-enhancing mechanism of the control at  $Re = 3000$  is similar as in  $Re = 300$ . First, interference from the TEV near the plate's surface is minimized by forcing the TEV to form, not at the trailing edge, but more downstream in the wake; second, downwash from the TEV in the wake is utilized to keep the vortices from the leading edge close to the plate's surface.

For  $\alpha = 10^\circ$ , we varied the forcing frequencies  $F^+$  and considered two different control waveforms corresponding to different duty cycles ( $DC = 5\%$  and  $DC = 100\%$ ) of actuation. Duty cycle was defined as percentage of the width of a sinusoidal waveform to the period of actuation. Therefore, at  $DC = 5\%$ , the waveform is essentially a train of pulses, while at  $DC = 100\%$ , it is a continuous sinusoid.

For low frequency actuation  $F^+ < 0.5$ , the more pulsatile waveforms had a stabilizing influence, and reducing the duty cycle (making the waveform more pulsatile) resulted in phase-locked flow, while more sinusoidal waveforms resulted in a chaotic response. The opposite was true at high frequencies, where the pulsatile waveforms led to an aperiodic response, while sinusoidal forcing led to a phase-locked flow, albeit one with no lift enhancement (in a time-averaged sense). In fact, at  $F^+ = 1.8$ , the  $DC = 100\%$  waveform resulted in a flow that was nearly steady, with only very small lift fluctuations around a value similar to the minimum lift occurring in the baseline vortex shedding cycle. The flow field in this case consisted of a regular array of 3-4 small vortices uniformly convecting downstream along the plate.

For  $\alpha = 20^\circ$ , we also varied the forcing frequencies  $F^+$  and considered a range of control waveforms corresponding to different duty cycles ( $DC$ ) of actuation.

With  $DC = 5\%$ , the flow was phase locked to the actuation for  $0.4 \leq F^+ \leq 0.7$ . We observed that the increasing duty cycles (from 5% to 100%) decrease the range of forcing frequencies with

phase-locked limit cycles. Also, for high duty cycles ( $DC \geq 50\%$ ) we observed a period doubling in the lift's response to high forcing frequency,  $1.0 \lesssim F^+ \lesssim 1.4$ . For these cases, the response was periodic at half the frequency of the forcing frequency ( $0.5 \leq F^+ \leq 0.7$ ), thus each shedding cycle occurs over two forcing cycles. The resulting flow field displayed formation of vortex pair acting as a lifting body on the plate's surface (however, resulted in similar lift as phase-locked flow forced at its shedding frequency,  $0.5 \leq F^+ \leq 0.7$ ).

Of the various frequencies and duty cycles considered, we found that a phase-locked response occurred when forced at  $F^+ = 0.6$ , or its first harmonic at  $F^+ = 1.2$  for  $DC \geq 50\%$ . In the latter case, the vortex shedding cycle still occurred at  $F^+ = 0.6$ .

Also, we found that the flow is susceptible to pulses with a very short duration (duty cycle of 5% of shedding period), as effective as continuous sinusoidal, which is consistent with the results by Greenblatt *et al.* (2008) This is also consistent with the results at  $Re = 300$  where the optimized waveform of pulsatile control resulted in even higher lift than a continuous sinusoidal forcing.

### 6.3 Recommendations for Future Work

Here, we comment on the possible continuation of the research presented in this thesis.

First, the feedback compensator developed in Chapter 4 can be applied to  $Re = 3000$ . Preliminary study of feedback with a rectangular waveform with a duty cycle of 5% as actuation waveform shows that the feedback was not able to maintain any desired phase shift. However, we found in Chapter 5 that the pulse cannot be too narrow in order to result in a stable limit cycle. Feedback with a higher duty cycle or smoothed waveform such as a sinusoidal pulse can result in more stable performance. Different control waveforms (varying duty cycles) can be investigated with the feedback in an attempt to phase lock the flow at the desired phase shift that is not attainable with open loop forcing. Also, the gradient-based approach developed in Chapter 4 can be extended to this  $Re$  of 3000 to optimize the control waveform and the frequency more directly. Different control objective such as minimizing lift fluctuation or maximizing lift-to-drag ratio can be investigated.

The presented analysis can also be extended to study the control of three-dimensional separated flows around low-aspect-ratio wings. Taira & Colonius (2009*b*) have shown that the aspect ratio and angle of attack are found to have a large influence on the stability of the wake profile and the force experienced by the low aspect-ratio wing. Also, they observed that the tip effects in three-dimensional flows can stabilize the flow and also exhibit nonlinear interaction with the shedding vortices. In this study of two-dimensional flow, we found that the sensitivity of the lift to the actuation was minimal after the maximum lift is achieved (lift decreasing phase) at each shedding cycle, and letting the LEV shed naturally was the most energy efficient. In the presence of the tip effect in three-dimensional flows, the spatial gradient of actuation in z-direction could be beneficial to initiate spanwise transport of vorticity through the tip. The use of the adjoint analysis alone will be useful in identifying effective actuator placement. Full adjoint-based optimization can be used to optimize both the spatial and temporal actuation profile. It would be interesting to see if the spanwise transport of vorticity through the tip vortex can be utilized to stabilize the leading-edge vortex close to the wing's surface, as in the flapping flight of bio-flyers. Of course, similar control studies can be performed on flows around non-rectangular wings, such as semicircular or delta-shaped planforms. Furthermore, demonstrating the robustness of the feedback controller will prove useful for the implementation of the controller on an actual micro air vehicle that operates under constant perturbations.

## Appendix A

# Appendix A

### A.1 Derivation of Linearized and Adjoint Equations

With the pre-computed steady state  $(\gamma_0, q_0)$ , the linearized equations are the same as equations (2.9, 2.10) with the nonlinear term  $n(q)$  replaced by its linearization about the steady state, and is denoted by  $n_L(\gamma_0)\gamma = q_0 \times \gamma + q \times \gamma_0$  where the flux  $q$  is related to  $\gamma$  by (2.8). Thus, the linearized equations are:

$$\frac{d\gamma}{dt} + C^T E^T \tilde{f} = -\beta C^T C \gamma + C^T n_L(\gamma_0) \gamma \quad (\text{A.1})$$

$$ECs = u_{jet}. \quad (\text{A.2})$$

$$(\text{A.3})$$

The boundary conditions for the linearized equations are  $bc_\gamma = 0$  on the outer boundary of the largest computational domain.

Inner product is defined as:

$$\langle c, d \rangle = \int \int \gamma_c \cdot (C^T C)^{-1} \cdot \gamma_d dx dt + \int \int \tilde{f}_c \cdot \tilde{f}_d dx dt \quad (\text{A.4})$$

$$c = \begin{pmatrix} \gamma_c \\ \tilde{f}_c \end{pmatrix} \quad d = \begin{pmatrix} \gamma_d \\ \tilde{f}_d \end{pmatrix} \quad (\text{A.5})$$

in order to result in the adjoint equations which differ from the linearized equations only in the nonlinear term and is thus convenient for numerical implementation. The inner product defined is the standard  $L^2$ -inner product weighted with the inverse-Laplacian operator.

Let  $(\zeta, \psi)$  be the weighting functions corresponding to  $(\gamma, \tilde{f})$ . Then, using the inner product defined in equation (A.4), the weak form of (A.1, A.2) is:

$$\int_0^T \int_{\Omega} \zeta \cdot (C^T C)^{-1} \left( \frac{d\gamma}{dt} + C^T E^T \tilde{f} + \beta C^T C \gamma - C^T n_L(\gamma_0) \gamma \right) dx dt + \int_0^T \int_{\Omega} \psi \cdot ECs dx dt = 0. \quad (\text{A.6})$$

Integrating by parts with respect to  $t$  and rearranging terms,

$$\int_0^T \int_{\Omega} \gamma \cdot \left( - (C^T C)^{-1} \frac{d\zeta}{dt} + (C^T C)^{-1} C^T E^T \psi + \beta \zeta - ((C^T C)^{-1} C^T n_L(\gamma_0))^T \zeta \right) dx dt + \int_0^T \int_{\Omega} \tilde{f} \left( EC(C^T C)^{-1} \zeta \right) dx dt + \langle \gamma, \xi \rangle \Big|_0^T = 0. \quad (\text{A.7})$$

For linearization about stable steady states,  $\gamma \rightarrow 0$ , as  $T \rightarrow \infty$ , and if the adjoint equations are integrated backwards in time,  $\zeta(t=0) \rightarrow 0$ . So, the last term on the left hand side of equation (A.7) vanishes identically. If equation (A.7) is to hold for all values of  $\gamma$  and  $\tilde{f}$ , we get the following adjoint equations hold:

$$- \frac{d\zeta}{dt} + C^T E^T \psi = -\beta C^T C \zeta + (C^T C) n_L(\gamma_0)^T q_a \quad (\text{A.8})$$

$$EC\xi = 0 \quad (\text{A.9})$$

where  $\xi = (C^T C)^{-1} \zeta$  and  $q_a = C\xi$  can be thought of as the weighting functions corresponding to the streamfunction  $s$  and the flux  $q$  respectively. Now, equations (A.10, A.11) have the same form as (2.1, 2.2) except for the nonlinear term. Thus, the same time-integration scheme can be used for both, with the appropriate (linearized) nonlinear terms.

$$\frac{d\zeta}{dt} + C^T E^T \psi = -\beta C^T C \zeta + (C^T C) n_L(\gamma_0)^T q_a \quad (\text{A.10})$$

$$EC\xi = 0 \quad (\text{A.11})$$

where the variables  $\zeta$ ,  $\xi$ , and  $\psi$  are the duals of the discrete circulation  $\gamma$ , stream function  $s$ , and body force  $\tilde{f}$ , respectively, and  $q_a = C\xi$  is the dual of flux  $q$ . The adjoint of the linearized nonlinear term is  $(C^T C) n_L(\gamma_0)^T q_a$ , which can be shown to be a spatial discretization of  $\nabla \times (\gamma_0 \times q_a) - \nabla^2(q_0 \times q_a)$ . Since equation (A.10) differs from (A.1) only in the last term on the right hand side, the numerical integrator for the adjoint equations can be obtained by a small modification to the linearized equations solver.

## Appendix B

# Appendix B

### B.1 Extended Kalman Filter

The extended Kalman filter (EKF) is a tool for estimating the state of a system which is described by a nonlinear state space model. The EKF state estimates are an approximation to the mean of the conditional density of the state  $\{x_k\}$  given the measurements  $\{y_0, \dots, y_k\}$ . The EKF is derived by linearizing the signal model about the current predicted state estimate and then using the Kalman filter on this linearized system to calculate a gain matrix. The gain matrix, along with the nonlinear signal model and new signal measurements, is used to produce the filtered state estimate and then an estimate of the state at the next time instant.

Given a nonlinear system

$$x_{k+1} = f(x_k) + w_k \tag{B.1}$$

$$y_k = h(x_k) + v_k, \tag{B.2}$$

with smooth vector fields  $f$  and  $h$ . The disturbance  $w$  and noise  $v$  are assumed to be mutually independent, zero mean Gaussian processes, with covariance matrices  $Q_k = E(w_k w_k^T)$  and  $R_k = E(v_k v_k^T)$ . The objective is to reconstruct the state  $x$  from the sensor reading  $y$ . Dynamics state and observation estimates are distinguished by a hat:  $\hat{x}_k$  and  $\hat{y}_k$

The state of the EKF is represented by two variables, namely the estimated state  $\hat{x}$  and the error

covariance matrix  $P$ , which is a measure of the estimated accuracy of the state estimate. The EKF has the following two distinct phases.

Measurement update

$$\hat{x}_{k|k} = \hat{x}_{k|k-1} + K_k(y_k - h(\hat{x}_{k|k-1})) \quad (\text{B.3})$$

$$P_{k|k} = (I - K_k H_k) P_{k|k-1} \quad (\text{B.4})$$

Time update

$$\hat{x}_{k+1|k} = f(\hat{x}_{k|k}) \quad (\text{B.5})$$

$$P_{k+1|k} = F_k P_{k|k} F_k^T + Q_k \quad (\text{B.6})$$

where  $K_k$  is the optimal Kalman gain

$$K_k = P_{k|k-1} H_k^T (H_k P_{k|k-1} H_k^T + R_k)^{-1}, \quad (\text{B.7})$$

$H_k$  is the Jacobian of the output equation evaluated with the predicted state

$$H_k = \left. \frac{\partial h}{\partial x} \right|_{x=\hat{x}_{k|k-1}}, \quad (\text{B.8})$$

and  $F_k$  is the Jacobian of the dynamical system evaluated with the current state estimate

$$F_k = \left. \frac{\partial f}{\partial x} \right|_{x=\hat{x}_{k|k}}. \quad (\text{B.9})$$

and  $\hat{x}_{k|k}$  is the estimate of the state at time  $k$  and  $\hat{x}_{k+1|k}$  is the prediction of the state at time  $k+1$  using all the observations up to and including  $y_k$ . The matrices  $P_{k|k}$  and  $P_{k+1|k}$  are approximations of the respective state estimate error covariances.

In our application, filtered lift on the plate (input signal to the EKF) is approximated by a sine function  $y(t) = a_0 + a_1 \sin(\theta(t))$ . We assume a dynamical model with four states; frequency  $\omega$ , phase  $\theta$ , offset  $a_0$ , and amplitude  $a_1$ . Thus, the state of the system becomes

$$x = \begin{pmatrix} \omega \\ \theta \\ a_0 \\ a_1 \end{pmatrix}. \quad (\text{B.10})$$

Filtered lift signal is then described by the output equation

$$y_k = h(x_k) = x_{3,k} + x_{4,k} \sin(x_{2,k}), \quad (\text{B.11})$$

and a state-space model for the temporal evolution is provided by

$$x_{k+1} = \begin{bmatrix} 1 & 0 & 0 & 0 \\ \Delta t & 1 & 0 & 0 \\ 0 & 0 & 0.001 & 0 \\ 0 & 0 & 0 & 1 \end{bmatrix} x_k + w_k. \quad (\text{B.12})$$

In this application, the covariance matrices for the disturbance and the noise are set to be

$$R = 1 \quad \text{and} \quad Q = \begin{bmatrix} 0.25 & 0 & 0 & 0 \\ 0 & 0.00001 & 0 & 0 \\ 0 & 0 & 0.001 & 0 \\ 0 & 0 & 0 & 1 \end{bmatrix} \quad (\text{B.13})$$

and initial filter states are set to  $\hat{x}_0 = [1.5, 0, 0, 0]^T$  and  $P_0 = 0$ .

# Bibliography

- AHUJA, S. & ROWLEY, C. W. 2008 Low-dimensional models for feedback stabilization of unstable steady states. *AIAA Paper 2008-553* .
- AHUJA, S. & ROWLEY, C. W. 2010 Feedback control of unstable steady states of flow past a flat plate using reduced-order estimators. *Journal of Fluid Mechanics* **645**, 447–478.
- ALAM, MD. M., ZHOU, Y. & YANG, H. X. 2010 The ultra-low Reynolds number airfoil wake. *Experiments in Fluids* **48**, 81–103.
- AMITAY, M. & GLEZER, A. 2002 Role of actuation frequency in controlled flow reattachment over a stalled airfoil. *AIAA Journal* **40** (2), 209–216.
- AMITAY, M. & GLEZER, A. 2006 Flow transients induced on a 2D airfoil by pulse-modulated actuation. *Experiments in Fluids* **40** (2), 329–331.
- BEARMAN, P. W. 1967 On vortex street wakes. *Journal of Fluid Mechanics* **28**, 625–641.
- BERGER, E. 1967 Suppression of vortex shedding and turbulence behind oscillating cylinders. *Physics of Fluids* **10** (9P2), S191–193.
- BEWLEY, T. R., MOIN, P. & TEMAM, R. 2001 DNS-based predictive control of turbulence: an optimal benchmark for feedback algorithms. *Journal of Fluid Mechanics* **447**, 179–225.
- BIRCH, J. M., DICKSON, W. B. & H., DICKINSON M. 2004 Force production and flow structure of the leading edge vortex on flapping wings at high and low Reynolds numbers. *Journal of Experimental Biology* **207**, 1063–1072.

- BIRCH, J. M. & H., DICKINSON M. 2001 Spanwise flow and the attachment of the leading-edge vortex on insect wings. *Nature* **412**, 729–733.
- CATTAFESTA, L., GARG, S., CHOUDHARI, M. & LI, F. 1997 Active control of flow-induced cavity resonance. *AIAA Paper* (1804).
- COLONIUS, T., ROWLEY, C. W., TADMOR, G., WILLIAMS, D. R., TAIRA, K., DICKSON, W. B., GHARIB, M. & DICKINSON, M. 2006 Closed-loop control of leading-edge and tip vortices for small UAV. *Conference on Active Flow Control, DFG, Berlin, Sep. 27-29* .
- COLONIUS, T. & TAIRA, K. 2008 A fast immersed boundary method using a nullspace approach and multi-domain far-field boundary conditions. *Computer Methods in Applied Mechanics and Engineering* **197** (25-28), 2131–2146.
- DICKINSON, M. H. & GOTZ, K. G. 1993 Unsteady aerodynamic performance of model wings at low Reynolds-numbers. *Journal of Experimental Biology* **174**, 45–64.
- ELLINGTON, C. P., VANDENBERG, C., WILLMOTT, A. P. & THOMAS, A. L. R. 1996 Leading-edge vortices in insect flight. *Nature* **384** (6610), 626–630.
- GLEZER, A. & AMITAY, M. 2002 Synthetic jets. *Annual Review of Fluid Mechanics* **34**, 503–529.
- GLEZER, A., AMITAY, M. & HONOHAN, A. M. 2005 Aspects of low- and high-frequency actuation for aerodynamic flow control. *AIAA Journal* **43** (7), 1501–1511.
- GREENBLATT, D., GOKSEL, B., RECHENBERG, I., SCHULE, C. Y., ROMANN, D. & PASCHEREIT, C. O. 2008 Dielectric barrier discharge flow control at very low flight Reynolds numbers. *AIAA Journal* **46** (6), 1528–1541.
- GREENBLATT, D. & WYGNANSKI, I. J. 2000 The control of flow separation by periodic excitation. *Progress in Aerospace Sciences* **36** (7), 487–545.
- GRIFFIN, O. M. 1978 Universal Strouhal number for locking-on of vortex shedding to vibrations of bluff cylinders. *Journal of Fluid Mechanics* **85** (Apr), 591–606.

- HUANG, L., HUANG, P. G., LEBEAU, R. R. P. & HAUSER, T. 2004 Numerical study of blowing and suction control mechanism on NACA0012 airfoil. *Journal of Aircraft* **41** (5), 1005–1013.
- HUANG, X. Y. 1996 Feedback control of vortex shedding from a circular cylinder. *Experiments in Fluids* **20** (3), 218–224.
- KEGERISE, M. A., CABELL, R. H. & CATTAFESTA, L. N. 2007a Real-time feedback control of flow-induced cavity tones - part 1: Fixed-gain control. *Journal of Sound and Vibration* **307** (3-5), 906–923.
- KEGERISE, M. A., CABELL, R. H. & CATTAFESTA, L. N. 2007b Real-time feedback control of flow-induced cavity tones - part 2: Adaptive control. *Journal of Sound and Vibration* **307** (3-5), 924–940.
- KIM, J. & BEWLEY, T. R. 2007 A linear systems approach to flow control. *Annual Review of Fluid Mechanics* **39**, 383–417.
- LI, Z., NAVON, I., HUSSAINI, M. & LE DIMET, F. 2003 Optimal control of cylinder wakes via suction and blowing. *Comput. Fluids* **32**, 149–171.
- MADANGOPAL, R., KHAN, Z. A. & AGRAWAL, S. K. 2005 Biologically inspired design of small flapping wing air vehicles using four-bar mechanisms and quasi-steady aerodynamics. *Journal of Mechanical Design* **127** (4), 809–816.
- MAGILL, J., BACHMANN, M., RIXON, G. & MCMANUS, K. 2003 Dynamic stall control using a model-based observer. *Journal of Aircraft* **40** (2), 355–362.
- MIN, C. & CHOI, H. 1999 Suboptimal feedback control of vortex shedding at low Reynolds numbers. *Journal of Fluid Mechanics* **401**, 123–156.
- MIRANDA, S., VLACHOS, P. P., TELIONIS, D. P. & ZEIGER, M. D. 2005 Flow control of a sharp-edged airfoil. *AIAA Journal* **43** (4), 716–726.

- MUELLER, T. J. 1999 Aerodynamic measurements at low Reynolds numbers for fixed wing micro-air vehicles. <http://www.nd.edu/mav/belgium.pdf> [retrieved Oct. 2007] .
- PASTOOR, M., HENNING, L., NOACK, B. R., KING, R. & TADMOR, G. 2008 Feedback shear layer control for bluff body drag reduction. *Journal of Fluid Mechanics* **608**, 161–196.
- PESKIN, C. S. 1972 Flow patterns around heart valves: a numerical method. *Journal of Computational Physics* **10** (1), 252–271.
- PINES, D. J. & BOHORQUEZ, F. 2006 Challenges facing future micro-air-vehicle development. *Journal of Aircraft* **43** (2), 290–305.
- PINIER, J. T., AUSSEUR, J. M., GLAUSER, M. N. & HIGUCHI, H. 2007 Proportional closed-loop feedback control of flow separation. *AIAA Journal* **45** (1).
- RAJU, R., MITTAL, R. & CATTAFESTA, L. 2008 Dynamics of airfoil separation control using zero-net mass-flux forcing. *AIAA Journal* **46** (12), 3103–3115.
- RANEY, D. L. & SLOMINSKI, E. C. 2004 Mechanization and control concepts for biologically inspired micro air vehicles. *Journal of Aircraft* **41** (6), 1257–1265.
- ROMA, A. M., PESKIN, C. S. & BERGER, M. J. 1999 An adaptive version of the immersed boundary method. *Journal of Computational Physics* **153** (1), 509–534.
- ROSHKO, A. 1961 Experiments on the flow past a circular cylinder at very high Reynolds number. *Journal of Fluid Mechanics* **10** (3), 345–356.
- ROWLEY, C. W. & WILLIAMS, D. R. 2006 Dynamics and control of high-reynolds-number flow over open cavities. *Annual Review of Fluid Mechanics* **38**, 251–276.
- RULLAN, J. M., VLACHOS, P. P., TELIONIS, D. P. & ZEIGER, M. D. 2006 Post-stall flow control of sharp-edged wings via unsteady blowing. *Journal of Aircraft* **43** (6), 1738–1746.

- SCHNEIDER, T., SCHULE, C. Y., GREENBLATT, D., NAYERI, C. N. & PASCHEREIT, C. O. 2008 Experimental and computational investigation of active flow control with DBD plasma actuators at low Reynolds numbers. *Int. Conf. on Jets, Wakes and Separated Flows* .
- SCHOLZ, P., CASPER, M., ORTMANN, J., KAHLER, C. J. & RADESPIEL, R. 2008 Leading-edge separation control by means of pulsed vortex generator jets. *AIAA Journal* **46** (4), 837–846.
- SEIFERT, A., BACHAR, T., KOSS, D., SHEPSHELOVICH, M. & WYGNANSKI, I. 1993 Oscillatory blowing: A tool to delay boundary-layer separation. *AIAA Journal* **31** (11), 2052–2060.
- SEIFERT, A., GREENBLATT, D. & WYGNANSKI, I. J. 2004 Active separation control: an overview of Reynolds and mach numbers effects. *Aerospace Science and Technology* **8** (7), 569–582.
- SIEGEL, S., COHEN, K. & MCLAUGHLIN, T. 2006 Numerical simulations of a feedback-controlled circular cylinder wake. *AIAA Journal* **44** (6), 1266–1276.
- SOSA, R., ARTANA, G., MOREAU, E. & TOUCHARD, G. 2007 Stall control at high angle of attack with plasma sheet actuators. *Experiments in Fluids* **42** (1), 143–167.
- TADMOR, G. 2004 Observers and feedback control for a rotating vortex pair. *IEEE Transactions on Control Systems Technology* **12** (1), 36–51.
- TADMOR, G., NOACK, B. R., MORZYNSKI, M. & SIEGEL, S. 2004 Low-dimensional models for feedback flow control. part ii: control design and dynamic estimation. *AIAA Paper* (2409).
- TAIRA, K. & COLONIUS, T. 2007 The immersed boundary method: A projection approach. *Journal of Computational Physics* **225** (2), 2118–2137.
- TAIRA, K. & COLONIUS, T. 2009a Effect of tip vortices in low-reynolds-number poststall flow control. *AIAA Journal* **47** (3), 749–756.
- TAIRA, K. & COLONIUS, T. 2009b Three-dimensional separated flows around low-aspect-ratio flat plates. *Journal of Fluid Mechanics* .

- TAIRA, K., ROWLEY, C. W. & COLONIUS, T. 2010 Feedback control of a high-lift state for a low-aspect-ratio wing. *AIAA Paper 2010-357* .
- TORRES, G. E. & MUELLER, T. J. 2004 Low-aspect-ratio wing aerodynamics at low Reynolds numbers. *AIAA Journal* **42** (5), 865–873.
- VAINBERG, M. M. 1964 Variational methods for the study of nonlinear operators. *San Francisco : Holden-Day* .
- WANG, Z. J. 2000 Two dimensional mechanism for insect hovering. *Physical Review Letters* **85** (10), 2216–2219.
- WEI, M. J. & FREUND, J. B. 2006 A noise-controlled free shear flow. *Journal of Fluid Mechanics* **546**, 123–152.
- WU, J. Z., LU, X. Y., DENNY, A. G., FAN, M. & WU, J. M. 1998 Post-stall flow control on an airfoil by local unsteady forcing. *Journal of Fluid Mechanics* **371**, 21–58.
- ZHANG, M. M., CHENG, L. & ZHOU, Y. 2004 Closed-loop-controlled vortex shedding and vibration of a flexibly supported square cylinder under different schemes. *Physics of Fluids* **16** (5), 1439–1448.
- ZHANG, M. M., ZHOU, Y. & CHENG, L. 2008 Control of poststall airfoil aerodynamics based on surface perturbation. *AIAA Journal* **46** (10), 2510–2519.